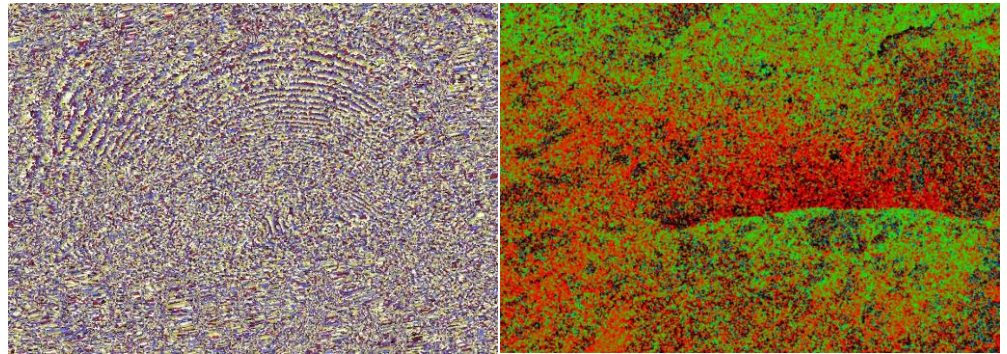# 3-D Surface Deformation Model from Sub-pixel Correlation of Optical Imagery and InSAR

DEWAN MOHAMMAD ENAMUL HAQUE

Enschede, The Netherlands, March, 2016

SUPERVISORS:

Professor Dr. Mark van der Meijde
Dr. Harald van der Werff

3-D Surface Deformation Model from Sub-pixel Correlation of Optical Imagery and InSAR
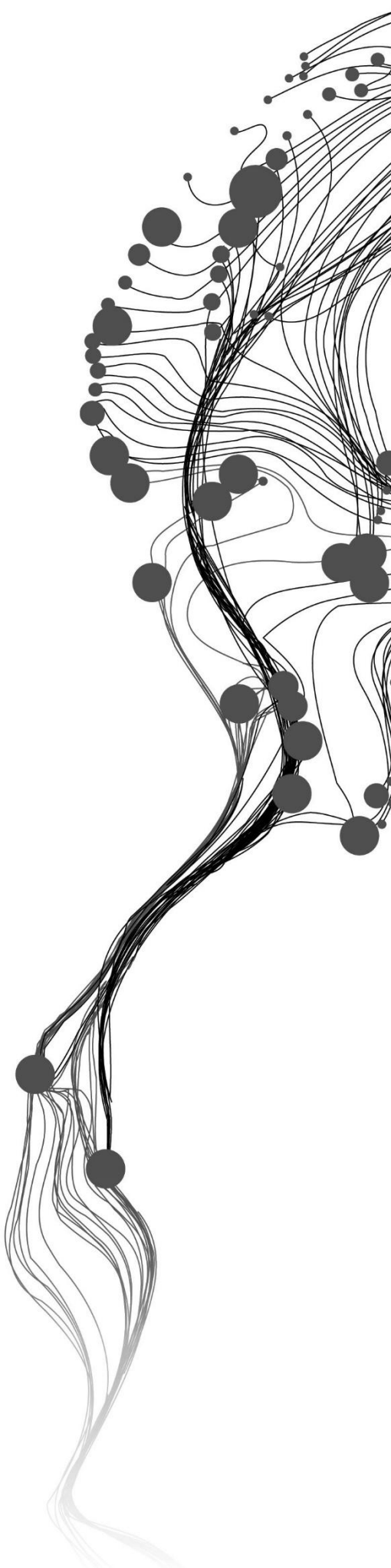
DEWAN MOHAMMAD ENAMUL HAQUE

Enschede, The Netherlands, March, 2016

Thesis submitted to the Faculty of Geo-Information Science and Earth Observation of the University of Twente in partial fulfilment of the requirements for the degree of Master of Science in Geo-information Science and Earth Observation.
Specialization: Applied Earth Sciences

SUPERVISORS:
Prof. Dr. Mark van der Meijde
Dr. Harald van der Werff

THESIS ASSESSMENT BOARD:
Prof. Dr. Freek van der Meer (Chairman)
Dr. Ir. (Seifko) Slob, Witteven+Bos Raadgevende Ingeneieurs B.V., Engineering and Consultancy Firm   (External Examiner)

ABSTRACT

A three-dimensional surface deformation model has been prepared through the current research work integrating the results of sub-pixel correlation of optical imagery and interferometric synthetic aperture radar (InSAR) technique. Earthquake surface deformation in the satellite line of sight (LOS) direction is measured by InSAR analysis and optical image cross-correlation technique has provided the horizontal surface displacement components. The vertical component of surface deformation is derived by utilizing these horizontal and LOS components. Moreover, the sensitivity of the parameters to prepare this surface deformation model is being evaluated. The prepared model has been validated with field and GPS measurement and compared with existing 3-D deformation models. To help reach the goal SPOT 10m resolution panchromatic imagery and ERS-2 SAR images are being utilized to investigate surface deformation caused by 12 November 1999 Düzce earthquake, Turkey. It is found that the Düzce earthquake is characterized by the bilateral surface break, Northside down and Southside up deformation scenario and dominant right lateral displacement in the eastern part.

ACKNOWLEDGEMENTS

TABLE OF CONTENTS

LIST OF FIGURES

LIST OF TABLES

1. INTRODUCTION

1.1 Preamble

Earthquake surface deformation analysis can provide in-depth information about earthquake source and earthquake dynamics-stress accumulation and slip distribution (Avouac et al., 2015; Oglesby & Mai, 2012; Biggs et al., 2007). Similarly, Lu et al (2010) claimed, to measure spatial and temporal patterns of surface deformation in seismically active regions is very useful for understanding rupture dynamics. Seismic risk can be estimated utilizing this information through seismic hazard assessment which basically guides civil defense agencies for proper land use planning, to prepare communities, constructing new infrastructures and retrofitting the vulnerable ones. Thus, life and property can be saved.

Surface deformation analysis can be performed either by in situ measurement or by earth observation techniques. Each technique has respective advantage and limitation. Although accurate measurement of surface break is achievable from the field methods (geophysical survey, trenching, investigating tectonic geomorphic features) but a holistic view of displacement is not obtainable (Gürbüz & Gürer, 2008; Similox-Tohon et al., 2008; Hasancebi et al., 2006; Hitchcock et al., 2003; Rockwell et al., 2001; Okay et al., 2000) despite time and labor intensive investigations. Moreover, it is very difficult to decipher the fault geometry in the field due its complex nature. Nowadays, several earth observation techniques either separately or in a combination are being repeatedly applied for ground deformation analysis such as Global Positioning System (GPS) measurement, Global Navigation Satellite System (GNSS), Interferometric Synthetic Aperture Radar (InSAR) and sub-pixel correlation of optical imagery (Ürüşan, 2014; Konca et al., 2010; Ayoub et al., 2009; Tahayt et al., 2009; Rott, 2009; Zhiyong et al., 2009; Hamiel & Fialko, 2007; Bürgmann et al., 2002; Hearn, 2002; Massonnet et al., 1993). Although both vertical and horizontal ground deformation information is obtainable from GPS measurement, continuous deformation scenario is not achievable as GPS stations have low spatial density.

However, the current research work gears towards the construction of three-dimensional (3-D) surface deformation (due to earthquake) model through the integration of results from the sub-pixel correlation of optical imagery and InSAR.

Sub-pixel analysis of pre and post-earthquake satellite optical images can measure horizontal ground deformation with $1/10$-$1/20^{th}$ -pixel accuracy (Yaseen & Anwar, 2013; Puymbroeck, 2008; Leprince et al., 2008; Avouac et al., 2006). Even this technique has been applied to measure dune migration (Necsoiu et al., 2009). And for seismic surface deformation measurement, it is very efficient technique (Dominguez, 2003; Feigl et al., 2002). Sub-pixel correlation of optically sensed images, however, cannot provide constraints on the vertical component of displacement as only horizontal components of displacement is retrievable from this technique (Avouac et al., 2006).

InSAR is the technique to study the phase difference between two SAR images acquired from different satellite positions or different times (Simons & Rosen, 2007). Vertical surface deformation information with sub centimetric accuracy can be derived from InSAR technique (Rott, 2009; Lasserre et al., 2005; Sandwell et al., 2002; Wright, 2002; Michel & Rignot, 1996). However, the main drawback is that it can provide the displacement value only along satellite line of sight (LOS) i.e. 1-D (Lindsey et al., 2015; Walter et al., 2008; Stramondo et al., 2005; Michel, 2002). For example, the sensitivity of European Satellites ERS is about 0.01, 0.3 and 0.9 in North, East and Vertical direction respectively and hence interferometric measurement is more sensitive to line of sight (near vertical) components, East/West component is poorly represented and the North/South component is hardly reached (Vadon & Massonnet, 2000). Fortunately, horizontal surface displacement can be measured by sub-pixel correlation of SAR amplitude images (Goudarzi et al., 2012; Michel & Taboury, 1999). This technique is also known as pixel tracking/offset tracking/feature tracking (Simons & Rosen, 2007). Compared to InSAR, SAR offset tracking has three advantages (1) it is less sensitive to decorrelation, (2) phase unwrapping is not

required and (3) it rarely fails in terms of large displacement (Peltzer, 1999; Wang et al., 2007).Both range and azimuth offset can be retrieved from the correlation peak of the image amplitude (Michel & Rignot, 1996). In connection, Bechor & Zebker (2006) presents a method to extract two components of the displacement vector: one along the line of sight, the other in the along-track direction by multiple apertures InSAR technique (InSAR-MAI) which is basically based on splitting the aperture to form multiple interferograms instead of formation of single interferogram from conventional InSAR technique. These multiple interferograms are then differenced to get along-track displacement. They have claimed that this technique is more accurate to derive horizontal component of displacement from SAR amplitude images than conventional pixel/offset tracking technique (Peltzer et al., 2001; Fialko et al., 2001; Michel & Taboury, 1999). However, offset measurement often suffers from multiple outliers and patch-like artifacts, because the standard offset method is a regular moving window operation which does not consider the scattering characteristics of the ground (Wang & Jónsson, 2014).

As of late, multi-temporal analysis from SAR imagery are extensively being used in surface deformation measurement (Pagli et al., 2014; Hetland et al., 2012; Sousa et al., 2010; Riddick & Schmidt, 2011). And the techniques are broadly of two categories i.e. persistent scatter (PS) technique and small baseline approach (SBAS). Persistent scatter technique utilizes scattering characteristics that remain stable in time even viewed from a different angle (Sousa et al., 2010; Bürgmann et al., 2006). Small baseline approach is based on distributed scatterers which utilize many interferograms prepared in a conventional way and inverting these to derive incremental displacements; it is efficient when no point targets are identified but natural targets have correlated displacements (Squeesar et al., 2011; Casu et al.., 2011; Berardino et al., 2002). Due to long duration investigation, these techniques are most likely to suffer tropospheric delay which might contribute to the generation of extra phases (Jolivet et al.; 2011). Even, some studies e.g. Hooper (2008) has successfully integrated these two techniques (PS and SBAS). In connection, similar studies regarding the muti-temporal analysis of SAR and optical images can also be mentioned here. (Biggs et al., 2007) measures the interseismic deformation (slip rate) by stacking multiple interferograms for Denali fault Alaska. Milliner et al (2015) show the way of quantifying the near and far fault deformation from the multi-temporal analysis of aerial photos for Landers (Mw 7.3) earthquake. However, the current research is mostly interested in event based surface deformation analysis instead of time-dependent displacement measurement.

Now it's time to move from 2-D to 3-D. Whenever, InSAR measurement is available from different viewing geometries, it is possible to decompose 3-D displacement vector. To get three-dimensional continuous ground deformation, some noteworthy studies have been carried out. For instance, SAR sub-pixel correlation/pixel tracking can be used for 3D deformation measurement by utilizing line of sight (LOS), azimuth and range offset (Tobita et al., 2001). To get vertical, east and north co-seismic displacement components, in this study, a linear system of two equations for each pixel of SAR image have been solved (1) one equation for LOS displacement from ascending and descending orbits (2) another equation for the azimuthal offsets from the descending orbit. Similarly, Fialko et al. (2001) prepare 3D co-seismic surface displacement field for 1999 Mw 7.1 Hector Mine earthquake by combining radar amplitude and phase offset measurement from different satellite tracks.

In summary, to analyze horizontal surface deformation, sub-pixel correlation of optical imagery is comparatively more precise and InSAR technique provides most accurate vertical deformation information. So the current research work aims to integrate these two techniques. Some previous studies have also tried to combine these two techniques. For example, Wegner et al (2008)fused optical and SAR images and subsequently classified (by means of support vector machine or Markov random field classifier) for change detection. Despite the fast development, multi-source data fusion techniques still remain challenging due to varying spatial and temporal resolutions (Zhang, 2010). However, the goal of the current research is to measure surface deformation due earthquake, not image classification for land cover mapping.

So the fact is transparent that, to date surface deformation measurement integrating the results of sub-pixel correlation of optical imagery and InSAR remains as a good topic for research. Therefore, the optimal way of integrating these two techniques to model earthquake surface deformation is tried to be figure out through the current research work.

1.2   Research Problem and Scope

From the previous studies, it is evident that still now the construction of three-dimensional surface deformation model remains challenging task and needs further improvement. Particularly, 3-D surface deformation model combining two datasets from active and passive sensors is hotly interesting topic to study. The respective advantages and limitations of each technique have been elaborated in preamble section. Briefly, InSAR is highly sensitive to vertical deformation and horizontal deformation can be obtained from the sub-pixel correlation of optical imagery. Yet, there exist some obstacles to deal those techniques. Both techniques have to compromise with noises from multiple sources due to different sensor positions and different investigation duration. Furthermore, the spatial resolution and measurement accuracy of two datasets are different. Therefore, an attempt will be taken to prepare a 3-D coseismic deformation model by combining LOS deformation information from InSAR and horizontal surface deformation information from the sub-pixel correlation of optical imagery through the current research work. To fulfill the objective Düzce fault segment of North Anatolian fault in general and 12 November 1999 Düzce earthquake event, in particular, have been selected. There is a reason behind that, though. Some pertinent studies have already been carried out in the context of InSAR (Bürgmann et al., 2002), sub-pixel correlation of optical imagery (Konca et al., 2010) and field investigation (Pucci et al., 2006) on Düzce event. Instead of duplicate the previous works, current research wishes to complement towards further understanding.

1.3   Research Objectives

The main objective of the current research work is to prepare 3-D surface deformation model integrating horizontal surface deformation information from optical imagery and line of sight ground deformation information from InSAR for 12 November 1999 Düzce earthquake, Turkey.

The specific objectives are:

➢ To derive horizontal surface deformation information from the sub-pixel correlation of optical imagery

➢ To derive line of sight surface deformation information from InSAR technique

➢ Integration of this horizontal and vertical information to prepare a 3-D deformation model

➢ Validation of the model to be prepared

1.4   Research Questions

From the formulation of research objective, two specific research questions are emerged that fine tunes further research in a certain direction.

▪ How to integrate horizontal and vertical (LOS) surface deformation information derived from sub-pixel correlation and InSAR respectively? Which parameters are more sensitive to this integration?

▪ Does the 3-D deformation model represent the continuous deformation scenario of the study area? What is the performance of this model compared to GPS measurement and/or field observations?

1.5   Methodological Framework

Sometimes figures can tell the story better than description. The following flow diagram is a typical example of this situation. Briefly, the sub-pixel correlation technique has two broad steps: orthorectification of pre (master) and post (slave) earthquake images and subsequent cross-correlation. Similarly, InSAR also deals with two pre and post event SAR images. Whenever there is displacement, the corresponding phase shift can be detected through InSAR technique and presented in an SAR Interferogram. Then this Interferogram is being unwrapped to get continuous satellite line of sight deformation. The more detail is furnished as follows (Figure 1-1) and the description of each method is broadly outlined in chapter 3.
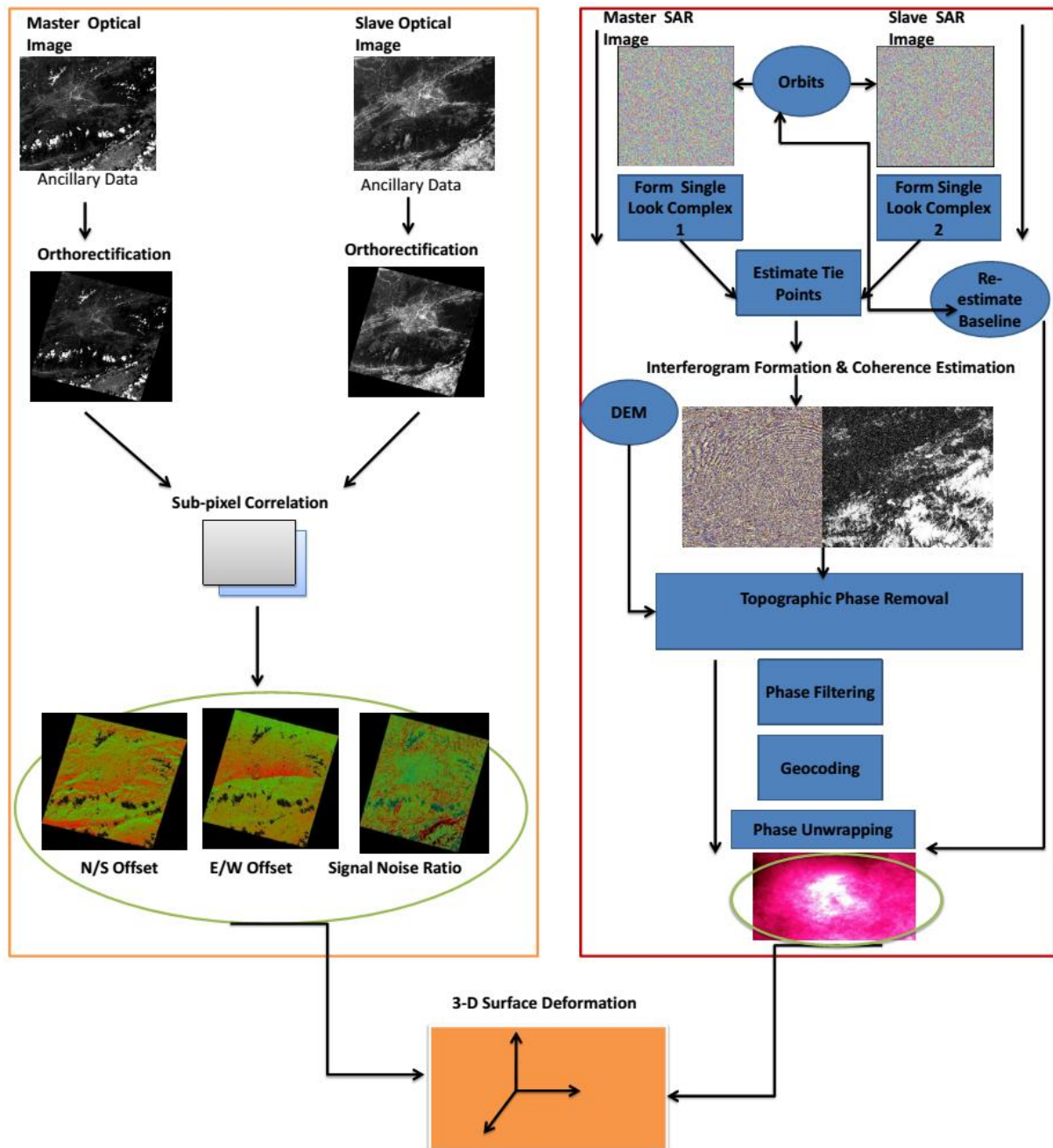
Figure 1-1 The methodological framework for the current research work; modified from (Sébastien et al., 2007; Simons & Rosen, 2007).

1.6 Thesis Structure

The MSc dissertation starts with scrutinizing existing relevant studies to find out the knowledge gap/lack of understanding and a possible way to improve the understanding of earthquake surface deformation analysis. Thus, the research objectives and research questions are being formulated. As the sun shows the day, the objectives have guided to define the methods to be followed. It is mentioned earlier that, to test the selected methods, the North Anatolian Fault has been chosen as a test site in general and Düzce earthquake (12 November 1999) in particular has been selected as a test event. The prepared 3-D surface deformation model is also being validated by field observations & GPS measurements and compared with some existing models. Thus, the summary of the research findings is outlined at the end along with mentioning the drawbacks of conducting this research and highlighting the limitations of the prepared model.

Briefly, the current research is designed into five main chapters:

Chapter 2 explains the tectonic settings of North Anatolian Fault. As per Düzce event is concerned, some remarkable findings from previous studies about Düzce rupture and slip distribution are outlined here so that possible outcome from this research can be anticipated.

Chapter 3 narrates the parts and parcel of each method that has applied in this study. The results from each method are also mentioned here simultaneously with methodological description.

Chapter 4 starts with the illustration of some best-cited research work dealing with 3-D surface deformation model. The approaches adopted to prepare 3-D surface deformation model is also explained in this chapter. A comparative picture of existing and adopted approach for surface deformation model will be reflected here.

Since the inception of chapter 5, a description of the validation processes of the constructed model is outlined. Not only verification, this chapter also interprets the results. Moreover, limitations of the present study are mentioned here too.

The last chapter, chapter 6 ends with concluding remarks along with pointing out some recommended ways to improve the obtained results and mentions the scope for future study.

2. GEOLOGIC SETTINGS OF THE STUDY AREA

2.1 Tectonic Settings in and around Düzce

Anatolian fault is well known active fault system which is formed by the complex tectonic interaction of Anatolian plate with Eurasian plate in the North, African plate in the South-West and Arabian Plate in the South-East (Reilinger, 2000; Reilinger et al., 2006; Lorenzo-Martín et al.,2006; Flerit et al., 2003; Kiratzi, 1993; McKenzie, 1972). As a consequence of this interaction, Anatolia is bounded by the right lateral North Anatolian Fault (runs along transform boundary between Anatolian plate and Eurasian plate) and left-lateral East Anatolian Fault (transform type boundary between Anatolian plate and Arabian plate). Actually, the North Anatolian Fault (NAF) is currently the most active fault system in Turkey and is characterized by several spectacular westward (towards Istanbul and Marmara sea) progressive earthquake sequences (Hamiel & Fialko, 2007; Ferrari et al., 2000; Barka, 1992; McKenzie, 1972). Their study shows that the NAF is characterized by six westward migrating strike-slip earthquakes (M>7) that have occurred from 1939-1999 (Figure 2-1). Stein et al (1997) and Pondard et al (2007) showed the role of stress transfer along NAF that figures out the relationship of the occurrence of an earthquake due to tectonic stress loading triggered by the previous earthquakes.
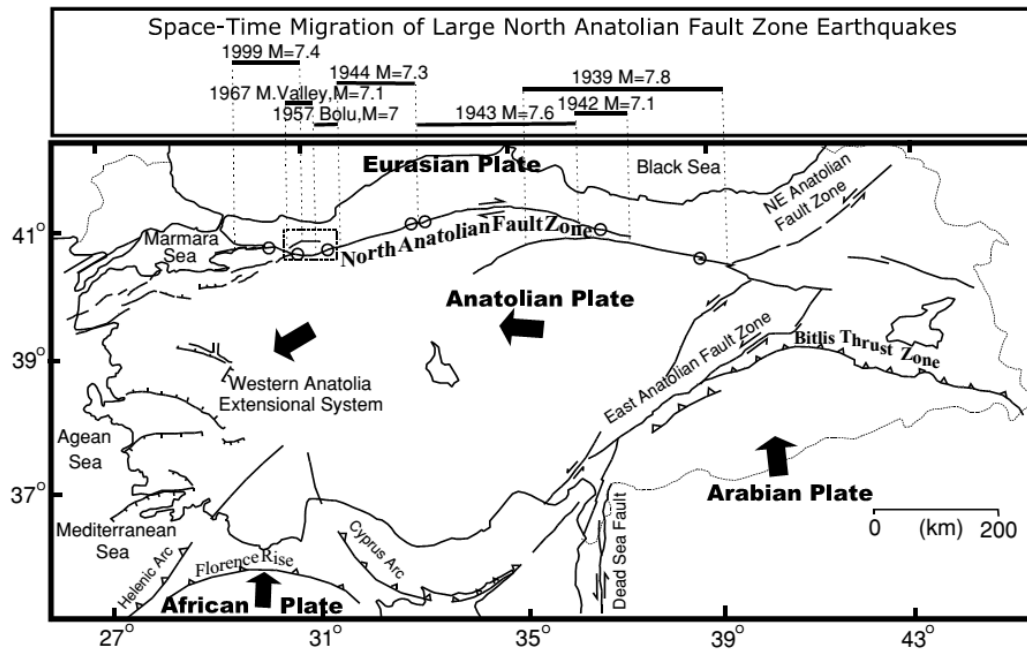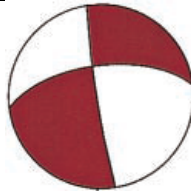
Figure 2-1 is showing major tectonic elements in and around Turkey. The space-time migration of previous 7 major earthquakes is also shown here. The dotted small black box shows the rupture zone from Düzce earthquake. Source: (Utkucu et al., 2003)

Stein et al (1997) have also predicted about Düzce fault segment as a stress shadow (this segment was undisturbed by earthquakes) and hence, it might be the possible zone of next rupture. And the prediction becomes true. The rupture from Düzce earthquake was initiated from the south of city Düzce where 87 days older Izmit earthquake terminated and progressed dominantly eastward. Düzce (7.2 M; USGS) event is characterized by 40 km long surface rupture and average 300 cm right lateral displacement with a maximum horizontal displacement of 500±5 cm and maximum vertical displacement was about 300 cm (Bouin et al., 2004; Akyüz et al., 2002). The focal mechanism (geometry of faulting during an earthquake) of Düzce earthquake shows that the fault dips to the North at an angle ranging from 53° to 73° with a rake between 167° and 184°(Çakir et al., 2003b). The earthquake source parameters for both Düzce and Izmit are outlined in the table (table 2-1) below:

Table 2-1 Source parameters of Düzce and Izmit earthquakes

Event	Strike (˚)	Dip(˚)	Rake (˚)	Mo (Nm)	Rupture Velocity (kms⁻¹)	Focal Mechanism
Izmit	270	83	181	$1.47×10^{20}$	4.5?	
Duzce	263	62	184	$0.47×10^{20}$	2	

<div align="right">

Source: (Tibi et al., 2001)

</div>

2.2 Surface Rupture due to Düzce Event in Retrospect

17 August Izmit and 12 November Düzce earthquakes together killed about 25,000 peoples and about 20 million people (one-third of the whole population of Turkey) are being affected (Sahin & Tari, 2000).

Actually, Duzce is an eastward extension of Izmit earthquake (Utkucu et al., 2003). After reaching Bolu, NAF splits into two parts: Northern (NNAF) and Southern (SNAF) (Oglesby & Mai, 2012). The Düzce fault (splaying from the southern branch of NAF), has created about 20km wide right step over between Düzce and SNAF fault (Locally known as Modurnu fault) (Hitchcock et al., 2003). From Cinarcik basin (within Marmara sea), the rupture of Izmit earthquake was initiated and terminated at Eften Lake (North of Golyaka fault segment) (Çakir et al., 2003a). Compared to the magnitude of Duzce earthquake (M=7.2) the surface rupture was only around 35km which is initiated in Golyaka fault segment (just south of Izmit rupture termination place) and continues eastward (Çakir et al., 2003b).

The above explanation can be easily visualized from the following pictorial representation (figure 2-2)
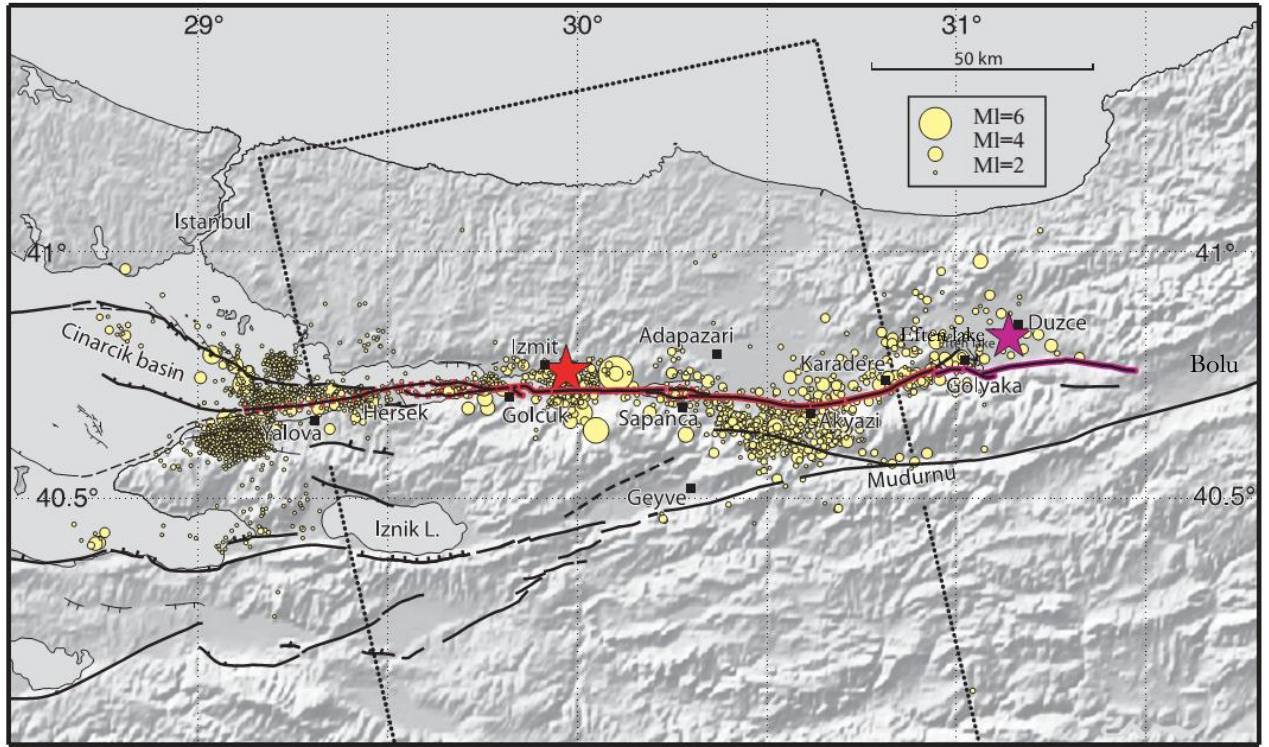
Figure 2-2 Before reaching Bolu the NAF is split into two major parts: Northern and Southern. Southern part consists of Mudurnu-Geyve fault segments. And Duzce-Karader-Goluck segments are in Northern Part. The red segment of Northern North Anatolian Fault (NNAF) was ruptured during Izmit earthquake and the violet segment is during Düzce event. Epicenters of the main shocks are indicated by stars. Yellow circles are showing the aftershocks (M_L>2) that occurred between 1999 August 20 and October 20. This information is shown in a background of GTOP30 DEM. The dotted rectangular area is the footprint of SAR image used in their study. The figure and information are taken from (Çakir et al., 2003a).

The rupture geometry of Izmit event is very complex which is characterized by numerous segmented surface ruptures and consecutive rupture breaks (Utkucu et al., 2003; Hitchcock et al., 2003). On the other side, Düzce is a typical example of bilateral surface deformation (Pucci et al., 2007). Although it moves dominantly eastward it has also ruptured western segment of Düzce fault. The rupture from Izmit event steps over (figure 2-3) the Düzce fault segment after crossing Eften lake, where maximum vertical displacement (~2.5m) (Pucci et al., 2007) was recorded.
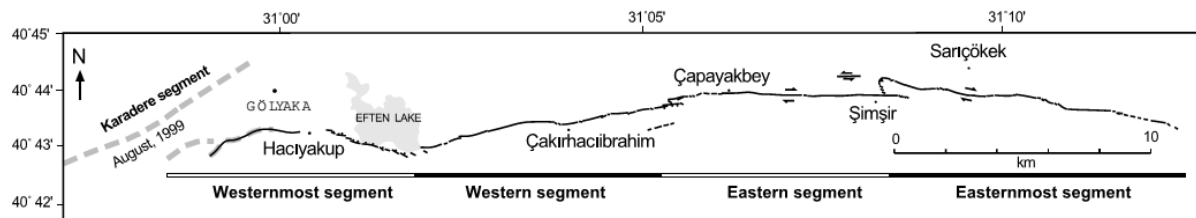
Figure 2-3 Surface Rupture Segments Associated with Düzce Event (from Çakir et al., 2003b)

Çakir et al., (2003b) has divided the Düzce rupture into four segments (figure 2-3) considering rupture geometry and slip distribution. Three segments except westernmost one are mainly characterized by right lateral movement (maximum right lateral movement was up to 5 meters in Eastern segment) and a

normal slip movement (maximum 3.0 meters) was recorded in the westernmost segment. This segment can be considered as an oblique transfer fault segment between NE-SW trending Karadere fault and the E-W trending Düzce fault. Moreover, important information can be obtained from the study conducted by (Bouchon & Karabulut, 2008). Most of the aftershocks associated with the Düzce event are located (figure 2-4) on the northern side of Düzce fault which suggests North Dipping fault plane. To the West of Düzce epicenter, aftershocks occurred at depth (cross section in the figure 2-4) which supports the reactivation of some Plio-Quarternary faults. This study also shows that Düzce is characterized by the combination of multiple ruptures.
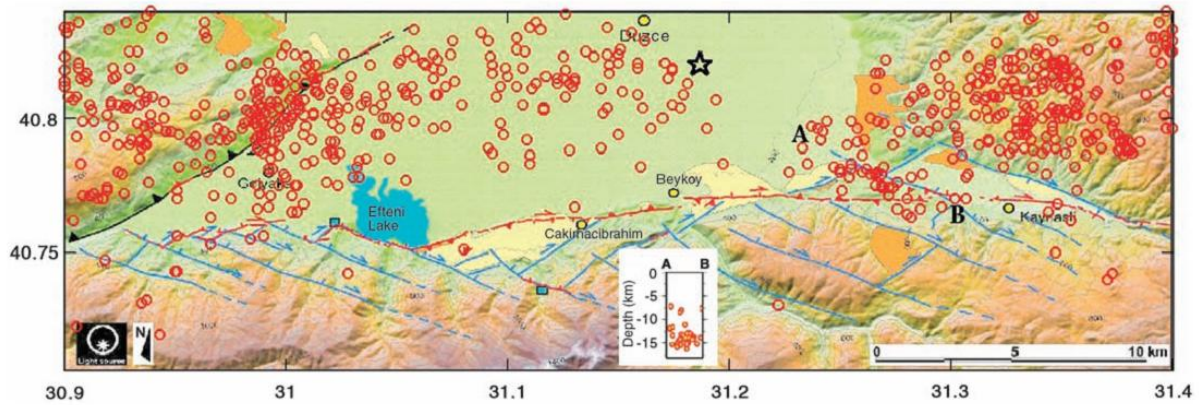
Figure 2-4: Map showing the location of the epicenter (black star) and aftershocks (red circles) of Düzce event. Düzce rupture is shown as red and Plio-Quarternary faults are in blue. The insert cross section is along A-B. Source: (Bouchon & Karabulut, 2008)

The figure (figure 2-5) below shows the rupture Length and average displacement for historic earthquakes occurred along North Anatolian Fault. Interestingly, Düzce event is characterized by the highest rupture to slip ratio than any other historical earthquake generated from North Anatolian fault (Ayhan et al., 2001). Star and diamond indicate the Düzce and Izmit event respectively. And circles are historical earthquakes since 1939.

Average Displacement (AD) (m)

$$\log (AD) = 1.43 + 0.88 * \log (SRL)$$

Surface Rupture Length (SRL)(km)
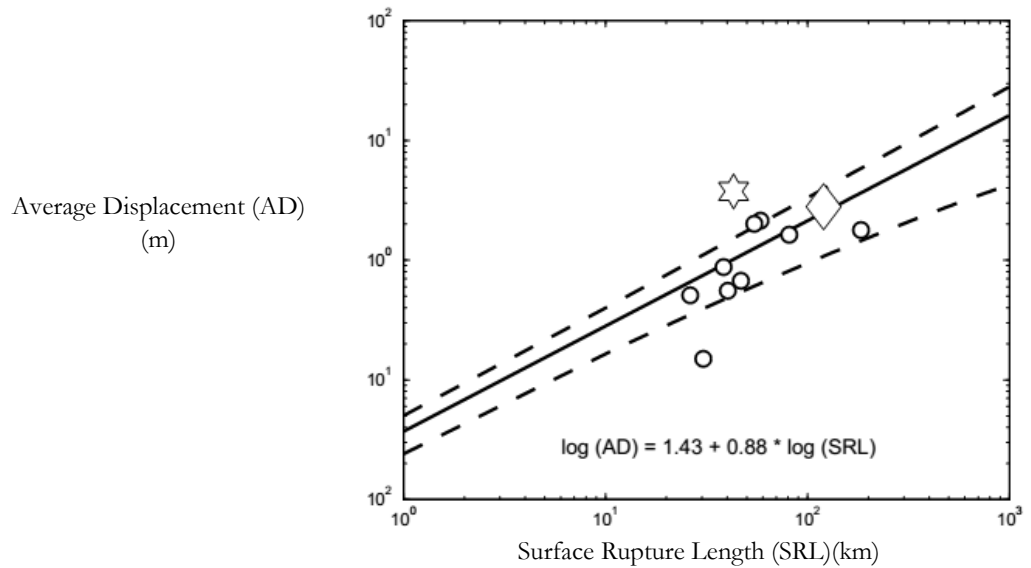
Figure 2-5 Average displacements and surface rupture length of some historic earthquake occurred along NAF (Ayhan et al., 2001). Düzce event (star) exhibits the highest slip to rupture ratio ever documented.

3. METHODS AND RESULTS

3.1 Introduction

The current research work is conducted for methodological improvement with an underlying motivation for the surface deformation measurement due to earthquake through the integration of two methods i.e. sub-pixel correlation of optical satellite imagery and InSAR. To help reach the goal, each method is being applied and results are derived; and subsequently integrated to construct a 3-D surface deformation model. In this particular chapter, results of each method are outlined simultaneously with the theoretical explanation of methodology. The intention of keeping methods and results together as one part is supporting another which might provide convenience to the readers.

3.2 Interferometric Synthetic Aperture Radar (InSAR)

3.2.1 InSAR Basics

SAR imagery exhibits two types of information: one is amplitude which is the strength or intensity of radar backscattered signal and another one is the phase (fraction of one complete sine cycle) which possesses the geometric information (Simons & Rosen, 2007). Typically, exposed rock or urban areas show strong amplitude (bright pixel) and water bodies show low amplitude (dark pixel). On the other hand, due to sinusoidal nature of radar signal, the delay between transmission and reception signals is proportional to the phase change.

Surface deformation can be measured from SAR image pair by two major techniques: a) formation of SAR interferogram (Massonnet & Feigl, 1998) by InSAR technique & b)sub-pixel correlation of SAR imagery (Michel & Taboury, 1999). The second method is also known as SAR offset tracking/pixel tracking which is capable of providing two components of displacement: one parallel to the satellite track (azimuth offset) and the other along the line of sight (range offset).

InSAR is a technique of exploiting phase difference from two SAR images acquired in a different time or from different vantage points (Bamler & Hartl, 1998). Surface shifts due to the earthquake can be detected as a phase difference in InSAR technique. Interferometric phase difference contains information about surface deformation together with atmospheric phase delay, topography, and noises from a number of sources (Hooper et al ., 2012).

$$\varphi = W\{ \varphi\,def + \varphi\,atm + \varphi\,orb + \varphi\,\theta + \varphi\,N\}$$

$\varphi\,def$ is the phase change due to movement of the pixel in the satellite line of sight (LOS) direction

$\varphi\,atm$ is the difference in the atmospheric phase delay between acquisitions

φorb is the residual phase due to orbit errors

$\varphi\,\theta$ residual phase due to looking angle error (commonly referred to as DEM error)

$\varphi\,N$ is the phase noise due to both variabilities in scattering and thermal noise

$W\{.\}$ is the wrapping operator that drops the whole phase cycle, because phase can only measure in terms of the fractional part of a cycle.

When the phase difference due to the difference in viewing geometry (i.e. topographic phase) is removed from the interferogram, the resulting output will show only surface change due to displacement assuming no other influences are present. For the sake of simplicity, let consider that surface has displaced from earthquake only. The equation for radar pulse (wave):

$E_y = \cos(\omega t + \beta x)$

Where, $\omega = \frac{2\pi}{T}$

And, $\beta = \frac{2\pi}{\lambda}$

This equation can be expressed in an exponential form:

$E_y = Eo.e^{j(\omega t \pm \beta x)}$ --(Equation 3-1)

In standard strip map mode the range (line of sight) and azimuth (along track) resolution can be calculated from:

$\Delta r = \frac{c}{2B}$ and $\Delta a = \frac{L}{2}$

Where, c, B, and L are speed of light, frequency bandwidth of radar pulse and antenna length along azimuth axis

Figure 3.1 shows the basic geometry for an Interferometric SAR model
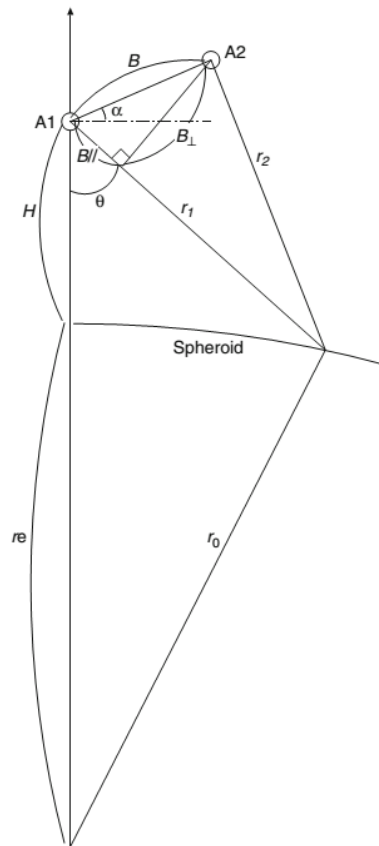
Figure 3-1 Basic SAR geometry. Source: (Masato Furuya, 2011)

A_1= antenna 1

A_2= antenna 2

$B_\parallel$ =baseline component parallel to the radar line of sight

$B_\perp$ =perpendicular baseline; similarly, the spatial separation between two antennas of different sensors, or between two vantage points of the same antenna of a sensor, is termed as the baseline (B).

So two co-registered focused complex SAR Data-SLC (Single Look Complex) images, E_1, and E_2, acquired from two different ranges r_1 and r_2 can be expressed according to equation 3-1:

$$E_1 = e^{j\Phi Scatter}\, e^{-\frac{4\pi r_1}{\lambda}}$$

$$E_2 = e^{j\Phi Scatter}\, e^{-\frac{4\pi r_2}{\lambda}}$$

Then the interferometric phase can be derived from

$$E_1{}^*E_2 = e^{-\frac{4\pi(r_1-r_2)}{\lambda}}$$

Or, $\Phi = \frac{4\pi}{\lambda}(r_1-r_2)$

This is the fundamental equation of InSAR which describes "wrapped" phase in the initial interferogram. The actual phase of the initial interferogram is "wrapped" into an interval $(0, 2\pi)$, thus an ambiguity of $2\pi N$ do exist, N is an integer and the factor 4 is taken for round-trip distances.

This equation can be simplified (as the baseline B is usually much shorter than the ground range distance R)

$$\Phi = \frac{4\pi}{\lambda}(r_1-r_2) \approx \frac{4\pi}{\lambda}B_{\parallel}\ \text{---(Equation 3-2)}$$

3.2.2 Decorrelation

Most of the cases, the fringes do not remain clear and/or continuous throughout the interferogram. Depending on data and places, fringes may vary from clear to obscured even completely missing. This phenomenon results from decorrelation.

Correlation and coherence are often synonymously used. The phase noise can be estimated from coherence. Correlation of two signals: S_1 and S_2 observed in interferometer aperture 1 and 2 can be defined as

$$\gamma = \frac{|\langle S_1 S_2^* \rangle|}{\sqrt{|\langle S_1 S_1^* \rangle||\langle S_2 S_2^* \rangle|}}\ \text{(Bamler \& Hartl, 1998)}$$

Where, * indicates complex conjugate.

Deterministic signals or signals with perfect combination exhibit correlation value 1 and signals with random component have an imperfect correlation less than one. Interferometric phase is a function of coherence; the better the correlation ($\gamma \sim 1$) the more conspicuous the interferogram will be (Simons & Rosen, 2007; Rosen et al., 2000)

Decorrelation originates broadly from spatial (geometric) error and temporally due to scattering characteristics. The other source of decorrelation is atmospheric and thermal delay of radar signal that might be the reason for the creation of extra fringes in SAR interferogram (Hanssen, 2001). The fringe density can be derived from the gradient of phase along the range axis. If the fringe density becomes too high within range resolution it will be very difficult to accurately count.

$$\frac{\partial \emptyset}{\partial R} = -\frac{4\pi B_\perp}{\lambda R tan\theta} + \frac{4\pi B_\perp}{\lambda(r_e + H)sin\theta} \approx \frac{4\pi B_\perp}{\lambda R tan\theta}\ \text{(Masato Furuya, 2011)}$$

Hence, the fringe density is proportional to the perpendicular baseline $B_\perp$ and inversely proportional to wavelength λ

And the critical baseline is determined by

$$B_\perp^c = \frac{\lambda R \tan\theta}{2\Delta r}$$

In connection, it can be noted that there is an upper bound for critical baseline over which interferogram decorrelates and hence no fringe is generated (Ferretti et al., 2007) and such an optimum baseline for ERS is about 300-400 meter. One relevant term can be explained here and that is the altitude of ambiguity. Altitude of ambiguity (that generates an interferometric phase change of 2π after interferogram flattening) depends on perpendicular baseline and it can be defined as:

$$ha = \frac{\lambda R \sin\theta}{2B_\perp} \quad \text{where, } R = \text{satellite altitude}$$

And phase flattening is achieved by subtracting the phase contribution of flat earth from the interferogram.

The 2nd type of decorrelation originates from scattering due to surface condition. However, the effect of decorrelation can be reduced a bit by two ways, each at the cost of resolution. One is filtering each image before interferogram formation (changing look direction) and another one is filtering after interferogram formation (Hooper et al., 2012). Goldstein filtering (Goldstein & Werner, 1998) permits retrieval of surface deformation or topography over large areas by preserving a high density of residues in noisy regions through effectively improving the performance of branch-cut phase unwrapping methods. In addition, Zebker & Villasenor (1992) pointed out some other sources of decorrelation (spatial baseline decorrelation, decorrelation due to rotation of the target between observations and decorrelation from surface motion of individual scattering centers within each resolution element) and explains how to quantify the contribution of each decorrelation sources so that this contribution can be removed from SAR interferogram.

3.2.3 Phase Noise Reduction, Phase flattening, and Unwrapping:

Generating noise free interferogram benefits unwrapping. In a noise free interferogram, the distance between two consecutive fringes is 2π. But the real interferogram exhibits a noisy pattern like in the figure 3-2 below. So before unwrapping it necessitates to filter out the noise as much as possible and then unwrapping it (Qing et al., 2000).
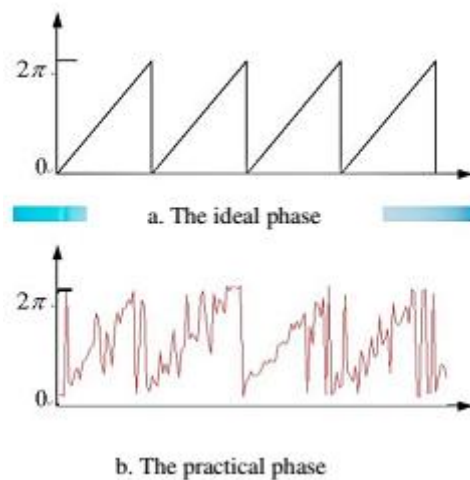
Figure 3-2 Comparison between ideal phase and real phase (Qing et al., 2000)

InSAR technique measures relative phase change between 0 to 2π (one complete wavelength) and hence, two targets will come out at the same phase if their ranges differ by an integer number of wavelengths. It is, therefore, necessary to find the multiples of 2π. Through phase unwrapping unambiguous phase values from SAR interferogram are being recovered (Hooper & Zebker, 2007). It is done by the subtraction of all full 2π intervals from the total pixel phase difference at two points (Rosen et al., 2000). When the phase of the continuous function reaches 2π, wrapped function returns to 0. Hence, phase unwrapping is the process of reconstructing continuous function from wrapped phase. Although improper unwrapping can cause significant measurement error, thorough explanation of phase unwrapping is beyond the scope of the current study. Many instructive studies (Agram & Zebker, 2009; Chen & Zebker, 2002; Chen & Zebker, 2001; Chen & Zebker,2000; Zebker & Villasenor, 1992), however, can be mentioned which has explained phase unwrapping in a great detail. Yet, a simple way of explaining phase unwrapping is outlined here.
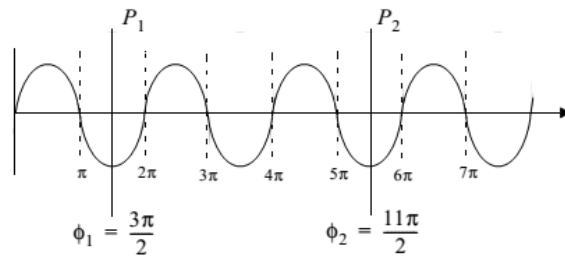
The phase difference between two points P_1 and P_2 in a radar pulse is

$$\Phi_1 - \Phi_2 = \frac{11\pi}{2} - \frac{3\pi}{2} = \frac{4\pi}{2}$$

But in case of interferogram formation $\Phi_1 - \Phi_2 = (module\, 2\pi)\frac{11\pi}{2} - (module\, 2\pi)\frac{3\pi}{2} = \frac{3\pi}{2} - \frac{3\pi}{2} = 0$

So the task of phase unwrapping is to convert the wrapped function (interferogram) into a continuous function like figure 3-3.
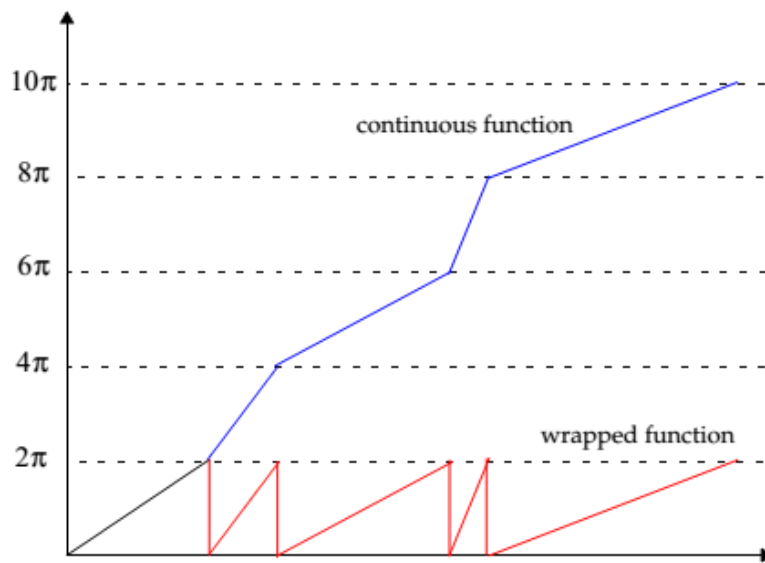
Figure 3-3: One-dimensional continuous vs wrapped phase (Erdas Field Guide, 1997)

The final unwrapped phase is converted to the line of sight (LOS) displacement by repositioning these wrapped functions into a continuous function which will indicate the real ground displacement. In general, the higher the wrapping frequency, the more difficult the area is to unwrap. Once the wrapping frequency exceeds the spatial sampling of the phase image, information is lost (Simons & Rosen, 2007; Bamler & Hartl, 1998).

As it mentioned earlier, before phase unwrapping and phase flattening, it is better to reduce the noise. Interferometric phase can be corrupted due to noise emerged from the temporal decorrelation, geometric decorrelation, volume scattering and processing error (Lu et al., 2010). Another topic needs some explanation in this context of noise and that is specles. Specles are pepper and salt like noise (occurred due to constructive and destructive interference) may present in SAR images that can be removed by speckle filtering. After radar image acquisition, specles are being reduced by applying adaptive and nonadaptive filters (Mansourpour et al., 2000) with an aim of preservation of radiometric information and not changing the spatial resolution. Spatial filters are categorized into two general groups i.e. non-adaptive (fast Fourier transform based) and adaptive filters (e.g. mean, median filters): the local properties of the terrain is neglected by the first category instead it considers the parameters of the whole image and the second group considers the local properties of the terrain backscatter or nature of sensor (Mansourpour et al., 2000). To preserve edge information along with speckle noise reduction adaptive filters (e.g. Lee, Refined Lee, Frost & GAMMA MAP filter) are usually being used.

3.3 Conducted InSAR Analysis

3.3.1 Raw SAR Data

To measure earthquake surface deformation, at least, two SAR images (pre- and post-event) are required. The perpendicular baseline (distance separating the two orbit of a pair of images) and the time interval between these two images should be as small as possible (Wauthier et al., 2009; Ferretti et al., 2007).

One pair ERS-2 SAR images from ascending track and another pair from the descending track are being analyzed for interferogram formation. But, the SAR interferogram from descending pair (dated 08/09/99 and 23/11/99) does not cover the rupture area. Bürgmann et al (2002) have also mentioned that there was no suitable image pair available from descending track to investigate Düzce rupture. So, the detail of SAR image pair from ascending east track which has been used for InSAR analysis is shown in Table 3-1

Table 3-1 Details of SAR Image Pair

Track	Frame	Orbit 1	Date-1	Orbit 2	Date 2	Perpendicular Baseline (m)	Altitude of Ambiguity (m)
114	812	23014	14/09/1999	24016	23/11/1999	259	37

The Shuttle Radar Topography Mission (SRTM) 1 ARC Second (~30m) DEM in UTM projection System is used both for InSAR and sub-pixel correlation of optical imagery analysis. This DEM has an absolute height accuracy of 10m, the absolute horizontal accuracy of 20m and relative horizontal accuracy of 15 m. These accuracies are quoted at 90% certainty level (Farr et al., 2001). The absolute vertical accuracy means the elevation error in the DEM with respect to the ground truth and similarly, the positional accuracy with respect to the ground truth is termed as absolute horizontal accuracy.

3.3.2 InSAR Analysis & Results

Interferograms are processed and analyzed with ROI_PAC (Repeat Orbit Interferometry Package) software (Rosen et al., 2004), as well as package SNAPHU (statistical cost network flow algorithm for phase unwrapping) (Chen & Zebker, 2002) was utilized to unwrap the interferogram. The topographic effects from the phase are removed by using 30m resolution SRTM DEM. Moreover, orbit files are used to estimate and to remove the orbital error. Goldstein (Goldstein & Werner, 1998) adaptive filtering was applied to reduce the noises emerged from high local fringe rate due to a large displacement. The incidence angle of ERS satellite is approximately 23° from vertical, so the measurement is mostly sensitive to vertical surface displacement.

The interferogram (figure 3-4) is a pictorial representation of a number of fringes. Actually, this is a relative measure of surface deformation. Fringe shows the difference in phase corresponding to difference in the distance during two observations. The deformation magnitude can be measured by counting the fringe numbers and multiplying it by half of radar wavelength.

Approximately 40 fringes are visible in the Northern part of the Düzce rupture from interferogram (figure 3-4) which suggests ~1.2m line of sight deformation (half of the wavelength ×number of fringes). From the line of sight (LOS) measurement it can be postulated (rough estimate) that the maximum vertical deformation will be around ~1.3m (LOS/cosine of incidence angle) and about 3.1m (LOS/sine of incidence angle) will be the maximum horizontal offset. If the fringes are distinguishable enough, similar fringes can be digitized (Wright et al., 1999) for accurate counting. The fringes become obscured close to the fault as well as southern part of the fault. This might be due to undersampling caused by high deformation rate and higher (259m in the present case) perpendicular baseline. Therefore, extra information is necessary to know about the true vertical deformation. From the previous literature, it is found that vertical displacement was around ~3meter. The discrepancy of vertical deformation between observed and field investigation arises from the opacity in the interferogram that inhibits counting all fringes. (Bürgmann et al., 2002) and (Çakir et al., 2003b) have also investigated Düzce rupture through InSAR analysis and the noise from large vertical displacement is acknowledged. Even none of these two studies, SAR Interferogram was unwrapped. And the reason for doing so is the presence of a noisy signal in Interferogram. They have also claimed that intensive agricultural practice close to the rupture zone was another source of noise. In addition, the densely vegetated area of northern part of surface rupture and rugged Almacik block to the South limit for adequate correlation. The transparency of fringes also depends on this coherence. Fringes having better coherence will be more conspicuous (Hanssen, 2005). As far as coherence is concerned, it should be mentioned that southeastern part (whitish part in figure 3-6) has the better correlation than close (both northern and southern proximity) to the rupture area. Although the southern part is more rugged terrain but it is sparsely vegetated (confirmed from google earth) and suffers less from Düzce event surface deformation; hence exhibiting better coherence.
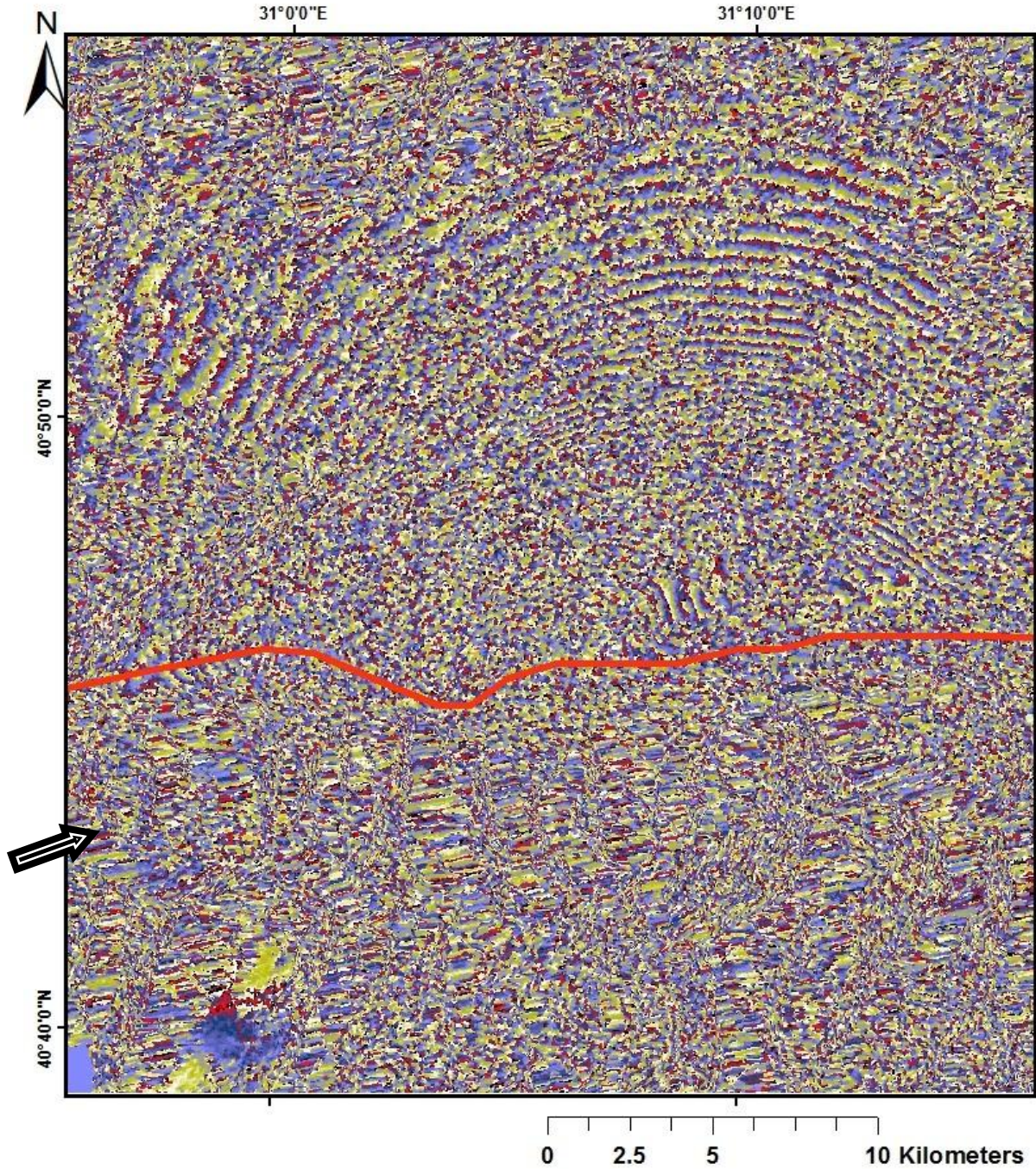
Figure 3-4 SAR Interferogram is obtained from ERS-2 SAR images acquired on 14 September & 23 November 1999. Arrow is showing the line of sight look direction. The raw images have a footprint of 100*100km. One fringe cycle indicates a range component of displacement (line of sight) of 2.83cm between the two images. The number of fringes increases from the North to the center (close to the Düzce rupture which is drawn as a red line) of the images which imply the maximum LOS displacement was in the central part. The Düzce rupture (red line) lies in the central eastern part (between 40˚40˝ to 40˚50˝ latitude) of the map. The asymmetry between two sides of the fault was due to fault geometry and rupture behavior of Düzce event. The Spatial baseline between two images is 259 meter.

The initially formed interferogram is unwrapped with SNAPHU and the relative line of sight displacement is shown in figure 6-5. The figure 3-5 is a subset of the complete unwrapped interferogram figure 6-5. The line of sight deformation is in radians. LOS component becomes positive when surface move along the line of sight direction and when surface moves towards the satellite, the LOS component exhibits negative value. In the present context, the bright part of figure 3-5 exhibits positive line of sight values and hence subsided. However, in some literatures (e.g. Hooper & Zebker, 2007), this sign convention is explained in a opposite way and the fact of inconsistency regarding this sign convention is clearly mentioned in (Bähr, 2013).

However, noise could not be removed even after unwrapping the interferogram. Arbitrary profiles aa´ and bb´ are drawn to see the pattern of unwrapping result and degree of noise present in the unwrapped interferogram. In both profiles, noise has been increased close to the fault.
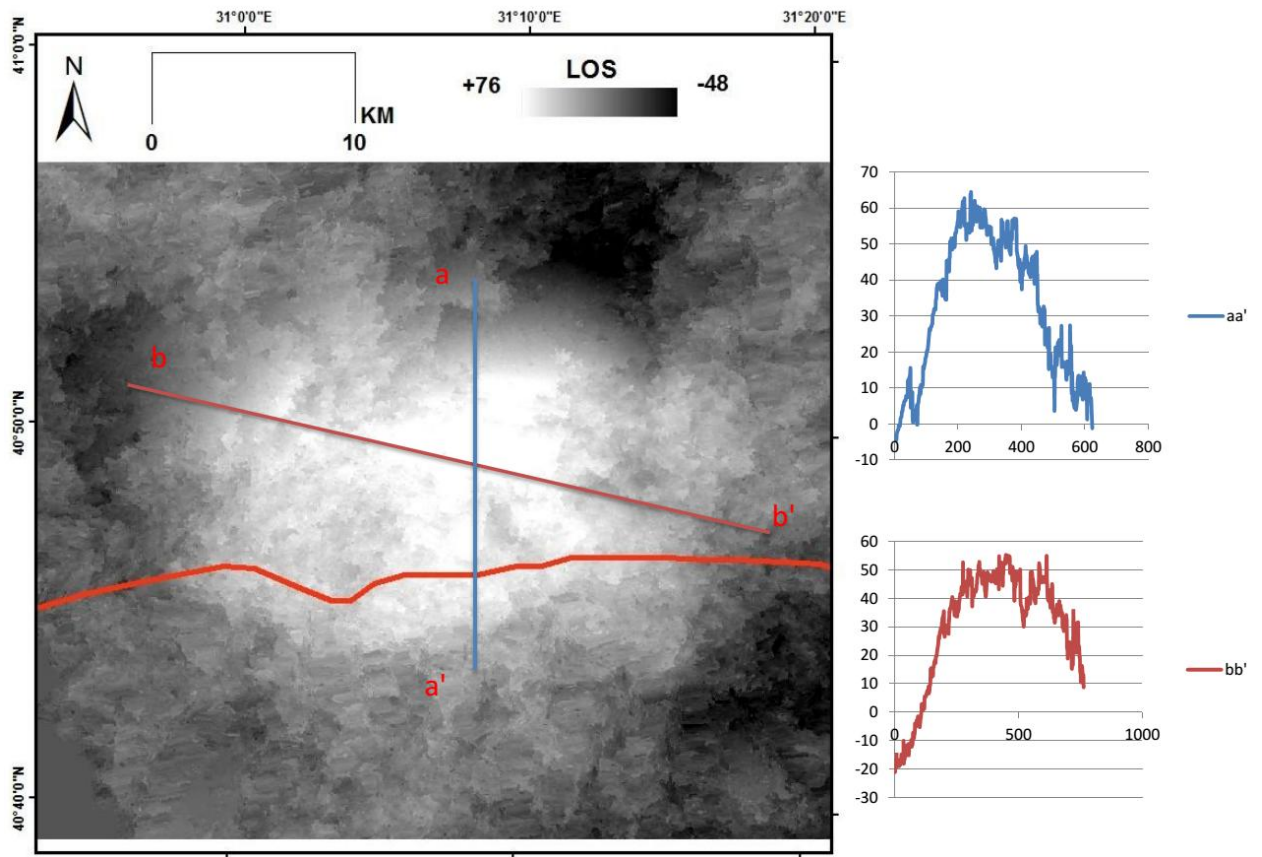
Figure 3-5 is the subset of gecoded unwrapped interferogram (figure 6-5). Despite unwrapping with SNAPHU the continuous phase is still noisy profile aa´ and bb´
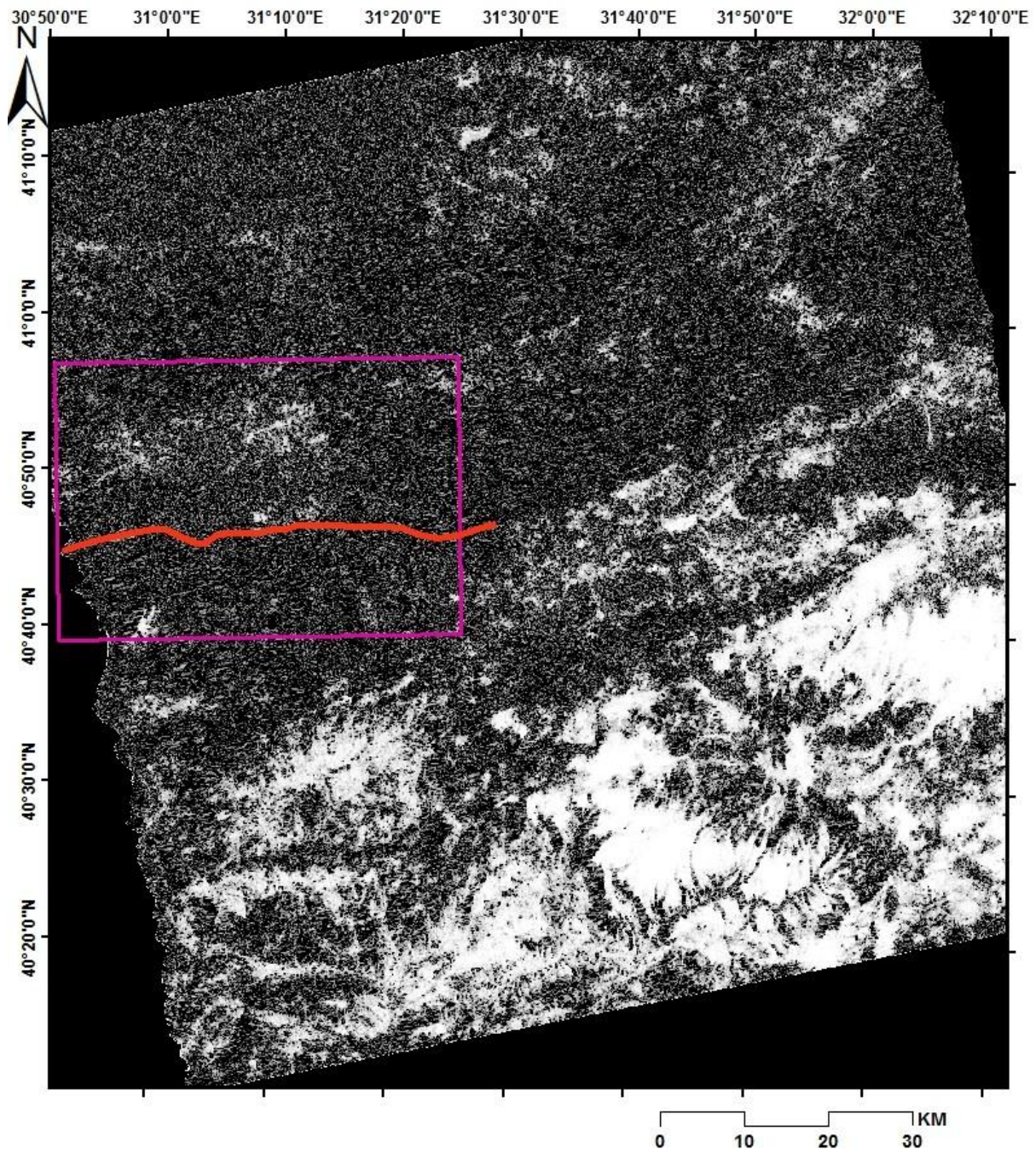
Figure 3-6 Corresponding coherence map of SAR interferogram (figure 6-1 in the appendix). Bright areas refer to better coherence and darker part is vice verse. Düzce and Izmit rupture which is shown as the red line is drawn from figure 6-3 (attached in the appendix). The area within the pink box is covering the area of figure 3-4 and 3-5

3.4 Sub-pixel Correlation of Optically Sensed Imagery

3.4.1 Method Overview

The sub-pixel correlation of optical imagery can provide interesting solutions including earthquake ground deformation analysis (Elliott et al., 2016; van der Meer et al., 2012). Recently developed COSI-Corr software (available at http://www.tectonics.caltech.edu/slip_history/spot_coseis/download_software.html) offers the opportunity to measure surface deformation at sub-pixel level with greater ease and accuracy

(~1/20th pixel accuracy) as the tool does not require external measurement like GPS measurement and is based on topographic knowledge and ancillary data provided by the observing sensors (Leprince et al., 2007). Although some other relevant free open source software like Medicis developed by CNES (Centre National d'Etudes Spati-ales, France), MicMac implemented at IGN (Institut National de l'Information Géographique et Forestière, France) are available, COSI-Corr (co-registration of optical imagery and correlation) is more familiar with scientific community (Rosu et al., 2014).

The main processing chain of COSI-Corr consists of two basic steps i.e. co-registration and sub-pixel correlation. The brief procedure to achieve precise co-registration and retrieve deformation information utilizing COSI-Corr which is being followed during current research work is mentioned here.

1. Ancillary data (orbits, platform attitudes, camera model, and digital elevation model) of both master and slave images is defined. The pre-earthquake image is taken as master image and slave image is the post-earthquake image.

2. Then orthorectification of both master and slave image is carried out to superimpose the two images accurately.

3. Following coregistration, correlation is performed selecting appropriate correlator, window size (number of pixels in both images) and step size (shift between two sliding windows).

4. Then the correlation of the two co-registered and orthorectified images results in a three band file containing the EW displacement map (positive toward the East), the NS displacement map (positive towards North), and Signal Noise Ratio (SNR) assessing the quality of the measurement. The resultant of two horizontal components will be a vector that shows the direction of surface movement.

The sub-pixel correlation method which has been followed here is a phase correlation method. Phase correlation method is more robust and accurate than classical cross-correlation method (Foroosh et al., 2002). All phase correlation methods rely on Fourier shift theorem. Fourier transform calculates the coefficients of sine and cosine curves to adequately represent the image and this phase correlation image alignment technique is very useful when images are taken from different sensors and having a different condition of illumination (Kuglin & Hines, 1975). From the phase difference of the Fourier transform, the relative displacement between two (pre- and post-event) overlapping images is derived (Foroosh et al., 2002; Stone et al., 2001).

Let, i_1 and i_2 are two images that differ only by displacement (Δ_x, Δ_y)

$i_2(x,y) = i_1(x - \Delta_x, y - \Delta_y)$

I_1 and I_2 are the corresponding Fourier transform of two images

$I_2(\omega_x, \omega_y) = I_1(\omega_x, \omega_y)e^{-j(\omega_x\Delta_x + \omega_y\Delta_y)}$

Where, ω_x and ω_y are the frequency variables in column and row i.e. amplitude of respective frequencies in x and y-direction.

Normalized cross power spectrum of image i_1 and i_2 can be expressed

$$C_{1,2}(\omega_x, \omega_y) = \frac{I_1(\omega_x,\omega_y)I_2^*(\omega_x,\omega_y)}{|I_1(\omega_x,\omega_y)I_2^*(\omega_x,\omega_y)|} = e^{j(\omega_x\Delta_x + \omega_y\Delta_y)}$$

The relative displacement based on Fourier shift theorem can be obtained by

$$F^{-1} \{e^{j(\omega_x \Delta_x + \omega_y \Delta_y)}\} = \delta (x + \Delta_x, y + \Delta_y)$$

The following sections start with a description of utilized optical satellite imagery, followed by more detail of each processing and analysis steps that has been followed in the present study in the context of sub-pixel correlation technique.

3.4.2 Conducted Sub-pixel Correlation Analysis

Raw Optical Data

SPOT Level 1A images are compatible with the COSI-Corr software. Three SPOT images are being utilized to investigate the effect of both Izmit and Düzce earthquake. So one Image was selected before Izmit event and another image was selected in between Izmit and Duzce event. Both of these images are correlated with 12 July 2000 SPOT image. The brief specification of available data is tabulated as follows:

Table 3-2: Specification of utilized SPOT Imagery

Parameters	SPOT-1	SPOT-1	Spot-4
Scene ID	1 105-268 99-06-21 09:03:10 2 P	1 105-268 99-10-03 09:02:33 2 P	4 105-268 00-07-12 09:02:45 2 M
Instrument	HRV 2	HRV 2	HRVIR 2
Preprocessing level	1A	1A	1A
Spectral band indicator	PAN	PAN	PAN
Orientation angle (degree)	12.8	12.7	12.6
Incidence angle (degree)	11.0	10.4	10.3
Sun Azimuth (degree)	143.0	165.2	142.3
Sun Elevation (degree)	69.4	44.4	67.7

The smaller off-nadir angle and similar incident angle image pairs are better for surface deformation measurement by COSI-Corr. Interestingly; the available images for this research purpose have identical incident angles.

Ancillary Data

SPOT level 1A images are provided along with its ancillary data. The ancillary file contains information on a number of useful parameters like position, attitude and look direction of the satellite during image acquisition. Moreover, the number of lines and columns in image, nominal ground resolution, solar azimuth and elevation can also found from ancillary data.

Selection of Tie Points and Ground Control Point Optimization

Initially, during co-registration of pre-earthquake image tie points were tried to be selected from shaded relief and raw image. Despite carefully selecting four ties points, the RMS becomes more than 9.00. Values of 0.5 to 1.0 pixels are normally regarded as being satisfactory (Townshend et al., 1992). According to the COSI-Corr user manual, this is the recommended way to select tie points. However, this operation is sensitive and does not always work well if the DEM is not well resolved. As a rule of thumb, if the resolution of the level 1A image is 1/3-1/4 times the DEM; this step does not work unless sharp

topographic features are well spread in the image. So the pre- earthquake image has been orthorectified from the absolute accuracy of the satellite metadata from the ancillary file and with the aid of DEM. DEM should cover more than the area of the raw image itself. Then tie points are being selected from the pre-earthquake orthorectified image and post-earthquake raw image. These points are subsequently optimized as Ground Control Points (GCP) to ensure well co-registration of the post-event raw image.

Prior to going into the following description, some important terminologies need to be clearer. Transformation is the mapping of locations of points in one image to the new location of points in another. This should be chosen carefully (because many types do exist) with an aim to remove spatial distortion between images due to the difference in acquisition and scene characteristics. The window size gives the number pixels of both images that are averaged to derive the deformation field and the step size is the distance in pixels between each sampling points. The step size should be related to window size; usually 1/4-1/8 times window size. In the case of large step size details will be lost and in the case of very small step size, the displacement field will be oversampled without adding any further details. Two types of correlation techniques are available in COSI-Corr software. The correlator works on the image frequencies, not on the absolute pixel values (Avouac et al., 2006). So the frequential correlator which is Fourier based and is suggested (by COSI-Corr user manual) to use during orthorectification of a raw image based on the orthorectified image. The statistical correlator, however, should be selected during orthorectification when the master image is shaded relief and slave is a pre-earthquake raw image (Ayoub et al., 2009). Further details about statistical correlation can be found in (Pratt, 1974).

GCPs are optimized by keeping sinc (sinus cardinal) resampling kernel size 25 and frequential correlator engine (window size 128/256, iteration 5 and mask threshold 0.9). Then the inverse mapping matrices are computed from GCPs to associate ground coordinates with raw pixel coordinates. However, it is found that kernel size 25 and window size 256 gives better convergence. Convergence shows the quality of coregistration i.e. the deviation of rows and columns of orthorectified images from standard X, Y coordinates. And the threshold performs like filtering and is always kept 0.9 as recommended by some previous studies (Yaseen & Anwar, 2013; Leprince et al., 2007).

Orthorectification and Resampling

Images are being resampled during coregistration with digital elevation model by sinc resampling method. In correlation, image offsets can emerge from two images if acquired from different orbits (as they have a different distance between orbits), the different geometry of detector and displacement of the ground due to the earthquake (Puymbroeck et al., 2000). For that reasons, images are being resampled with same DEM so that only offsets due to earthquake remain. There are some other resampling methods (bilinear and bicubic) do exist but they are suitable only to get fast visual results from both real and synthetic images (Leprince et al., 2007). In contrasts, sinc resampling provides less biased (residual biased ~0.2 pixels) estimate of offsets and more precise results from real images compared to other interpolators (Puymbroeck et al., 2000). Sinc resampler is defined by

$$\text{binterp(x,y)} \sum_{cl} b\,(c,l) = \frac{\sin \prod (c-x) \sin \prod (l-y)}{\prod (c-x) \prod (l-y)}$$

Where, binterp and b are the interpolated and raw images, respectively, and (x,y) are the coordinates of the interpolated images.

Orthorectification accounts for the acquisition distortion, scaling difference and topography by projecting both images on a common projection (Ayoub et al., 2009). The maximum distortion in ortho-rectification mapping i.e. image frequency content is determined by the variables known as transformation matrices, containing the x and y coordinates of the pixels in the image to project. These matrices have no standard value. But it's better if the values are close to 2 pixels; otherwise, orthorectification might fail. After

orthorectification (meaning that images are reprojected on the ground) each pixel of ortho-images seems like as it was seen exactly from the above.

Correlation

Cross correlation is not a registration method itself instead it is a similarity measure or match metric between an image and template; if the template matches exactly with the image, the cross-correlation reaches at its maxima (Brown, 1992; Foroosh et al., 2002). Correlation is processed using sliding window which scans both of the orthorectified images with an aim to similarity match and displacement is estimated from the coordinate of correlation peak. The consistency of measurement (correlation) can be estimated from phase change variability on a scale of the sliding window (Ayoub et al., 2009). This variability indicates the quality of measurement (Dominguez, 2003) i.e. coherence (ranging from 0 to 1).

Correlation images have been derived from SPOT-1 (pre-earthquake) and SPOT-4 (post-earthquake) image with different window-step size combinations (32-4, 32-8, 32-16, 64-8, 64-16 & 64-32). Correlation image results in a three band files i.e. EW, NS and SNR band. The EW and NS band correspond to displacement field measured along NS and EW direction; values are in meter and positive in North and East direction. And the quality of correlation can be assessed from SNR band. The output pixel size of correlation image is the input pixel size of the raw images multiplied by the step size between windows.

Post Processing

Some post processing steps are applied to obtain optimal results and to filter out outliers (exceptionally large displacement values). The displacement value that is beyond field measurement is usually being discarded. Prior to discarding, destriping is necessary. Through destriping correlation quality is preserved which back projects the correlation data in the satellite focal plane (Leprince et al., 2008). From the previous studies, it is found that maximum surface displacement (horizontal) did not exceed 10m during Duzce event. So displacement value beyond -10/10 has been discarded as the study is not concerned with extremely large unphysical measurement.

3.4.3 Results of COSI-Corr Analysis

As it mentioned earlier that, three SPOT images are available spanning both Izmit and Düzce event to conduct the study. The current research, however, mainly focused on investigating the Düzce event analyzing 03/08/99 and 12/07/2000 SPOT Images. In addition, two other combinations of analysis are also performed i.e. 21/06/99 and 12/07/2000 SPOT image correlation and 21/06/99 & 03/08/99 SPOT image correlation. The results from the last two combinations will help in result interpretation section. So these results are furnished in the appendix. And the following discussion will continue with the sub-pixel analysis for Düzce event only.

From the discussion of the previous sections, it is transparent that, a number of parameters need to be selected with care for better correlation result. And it is also mentioned that the quality of the result can be assessed from SNR band. So the histogram of SNR bands derived from different combinations of utilized parameters is the way of evaluating correlation quality.

It is found that sinc resampling method, frequential correlator with window size 32×32 and step size 4 provides a better result (based on Figure 3-7). Window size, step size; more precisely the step size is found as the most sensitive parameter during correlation. The quality of the result is assessed from SNR band and the histogram of SNR band. Figure 3-7 shows the histogram of coherence (SNR value 0 refers to no correlation and 1 indicates that the result is highly correlated) image (figure 3-11). The histogram shows the SNR values against the number of samples. The 32-4 window size-step size is found as the best combination on the basis of its SNR band. Although SNR bands from 32-4, 32-8, 32-16 (window-step size) have similar value and trend (figure 3-7), SNR from 32-4 combination has more affinity to

correlation value 1 (this has been verified by carefully looking into all SNR values against sample numbers).
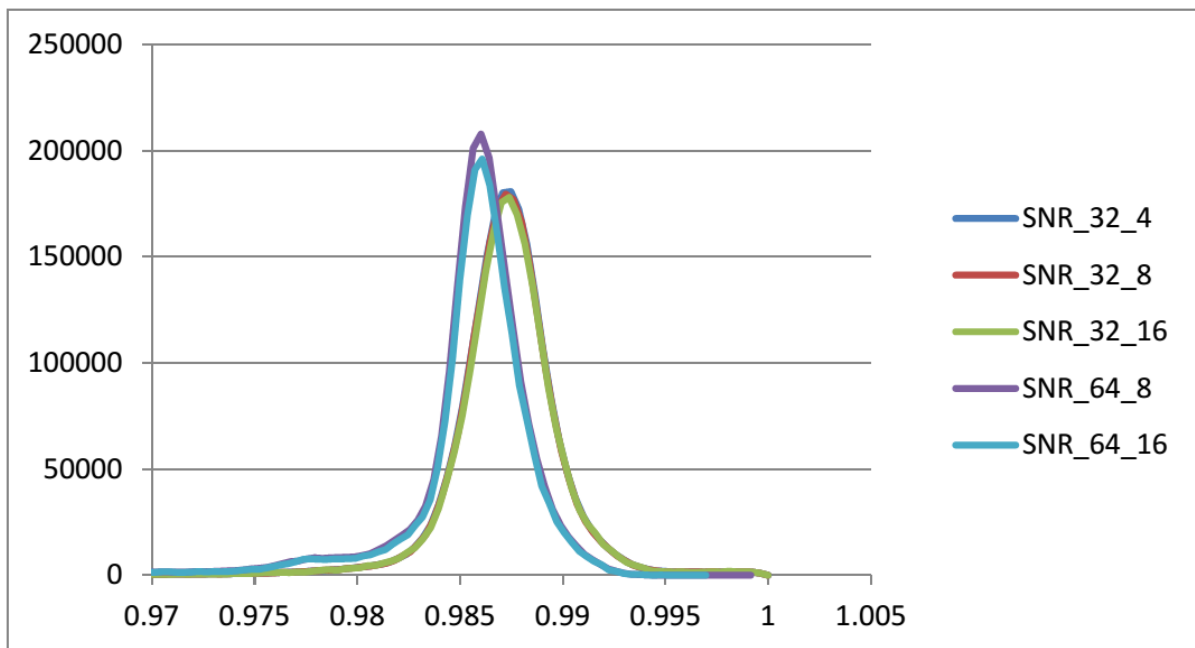
Figure 3-7 is showing Signal Noise Ratio (SNR) Value against Number of Samples

From the histogram (figure 3-8) of East West displacement map (figure 3-9), it is evident that most of the image samples (one example is figure 6-4, attached in the appendix) are exhibiting about +5 to -5 EW displacement value (within one standard deviation). This result has a good agreement with the previously conducted study (Konca et al., 2010). It should be noted here the current study is utilizing the same SPOT images what (Konca et al., 2010) have used.
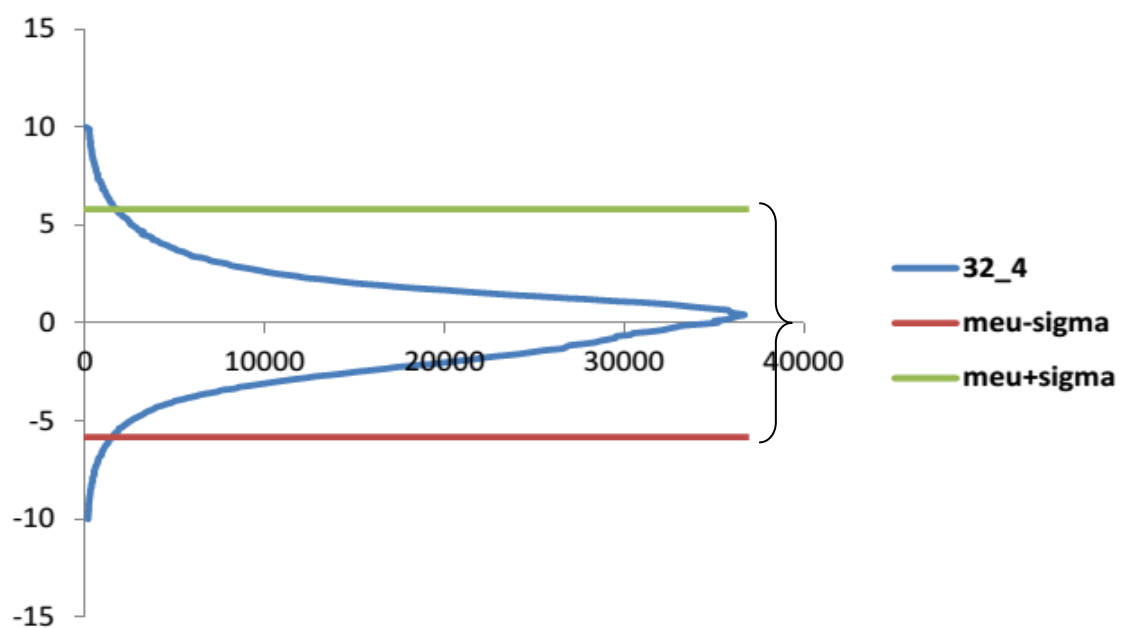
Figure 3-8: EW (Y-axis) displacement value against a number of samples. The second bracket is showing the displacement value within one standard deviation.

The EW and NS displacement can be visualized from figures 3-9 and figure 3-10 respectively. The surface rupture from Düzce event can be demarcated from the central right part of figure 3-9 where there exists a sharp discontinuity between red and blue color. The positive values of figure 3-9 indicate surface movement towards East and negative values refer to westward displacement. Some parts of the map are showing missing values and those places have suffered from decorrelation due to the presence of cloud in the images, the presence of lakes and landslides.
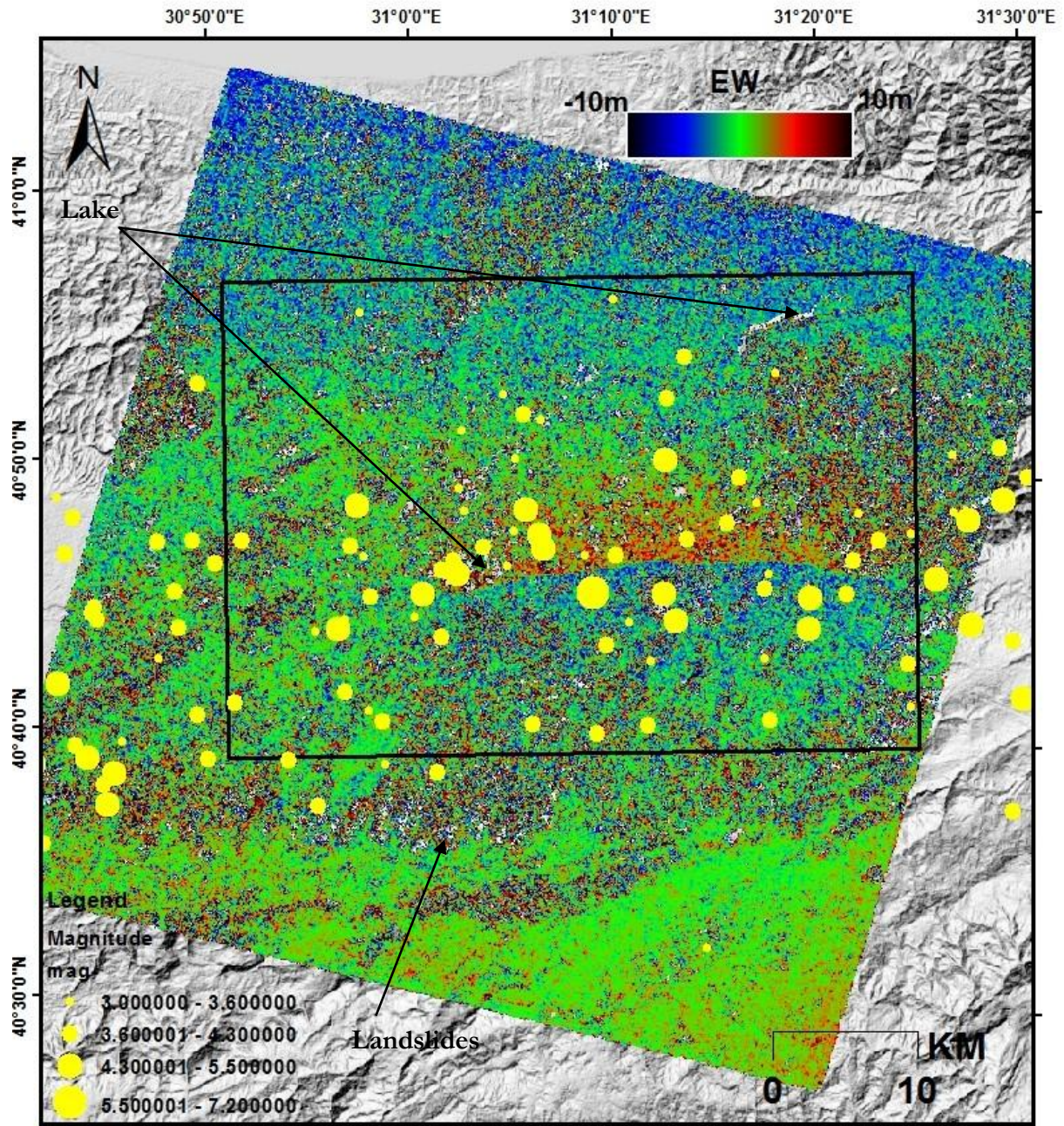
Figure 3-9 East-West Displacement map (positive towards East and Negative towards West) derived from sub-pixel correlation (window size 32×32 and step size 4) of SPOT Pan (10m) Image Pair (dated 03/08/99 & 12/07/2000) bracketing Düzce earthquake rupture area. Very few areas are decorrelated due to the presence of the lake, cloud, landslides and might be from building collapse. Yellow circled aftershocks (M>3) followed by both Izmit and Duzce are plotted from the information of USGS earthquake catalogue (17 August 1999 to 05 April 2000). The background hill shade image is 10m (resampled) resolution image

derived from SRTM 1 Arc Sec DEM. The blackbox is the region of interest for the 3-D surface model in the present study.

Similarly, the North-South surface movement is represented in the following figure. Positive values refer to the northward surface movement and negative value refers to southward movement. No vividly exposed discontinuity is observed between red and blue color like what was observed in EW displacement map. The black box (figure 3-10) is the region of interest for the 3-D model.
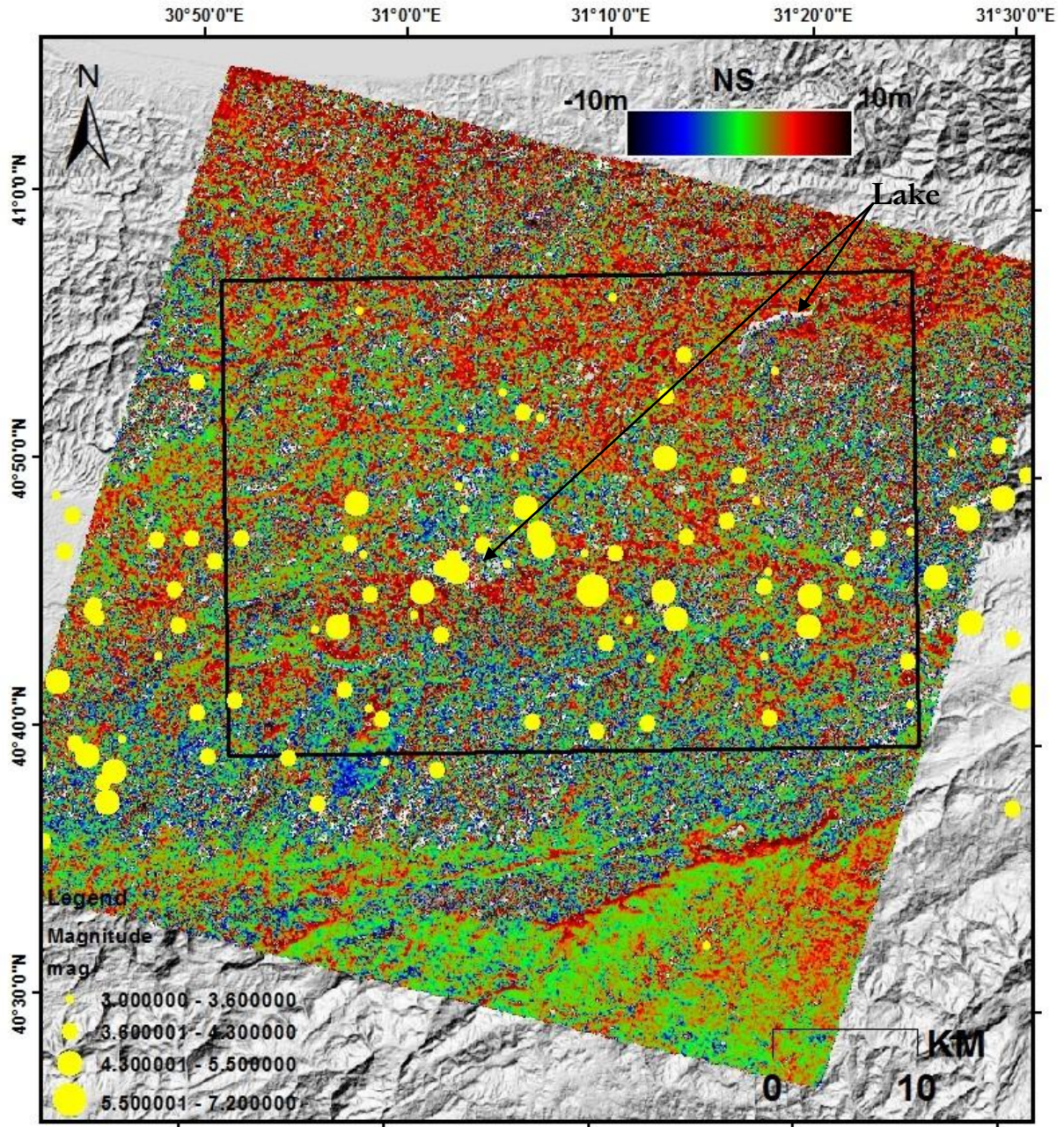
Figure 3-10 North-South Displacement map (positive towards North and Negative towards South) derived from sub-pixel correlation (window size 32×32 and step size 4) of SPOT Pan (10m) Image Pair (dated 03/08/99 & 12/07/2000) enveloping Düzce earthquake rupture area. No conspicuous displacement is observed. Very few areas are decorrelated due to the presence of the lake, cloud and might be for building collapses. Yellow circled aftershocks (M>3) followed by both Izmit and Duzce are plotted from the

information of USGS earthquake catalogue. The background hill shade image is 10m (resampled) resolution image derived from SRTM 1 Arc Sec DEM.

The band which determines the quality of sub-pixel correlation results is shown in figure 3.11. Overall coherence is found to be good except some areas which are covered by water bodies, landslides, and clouds.
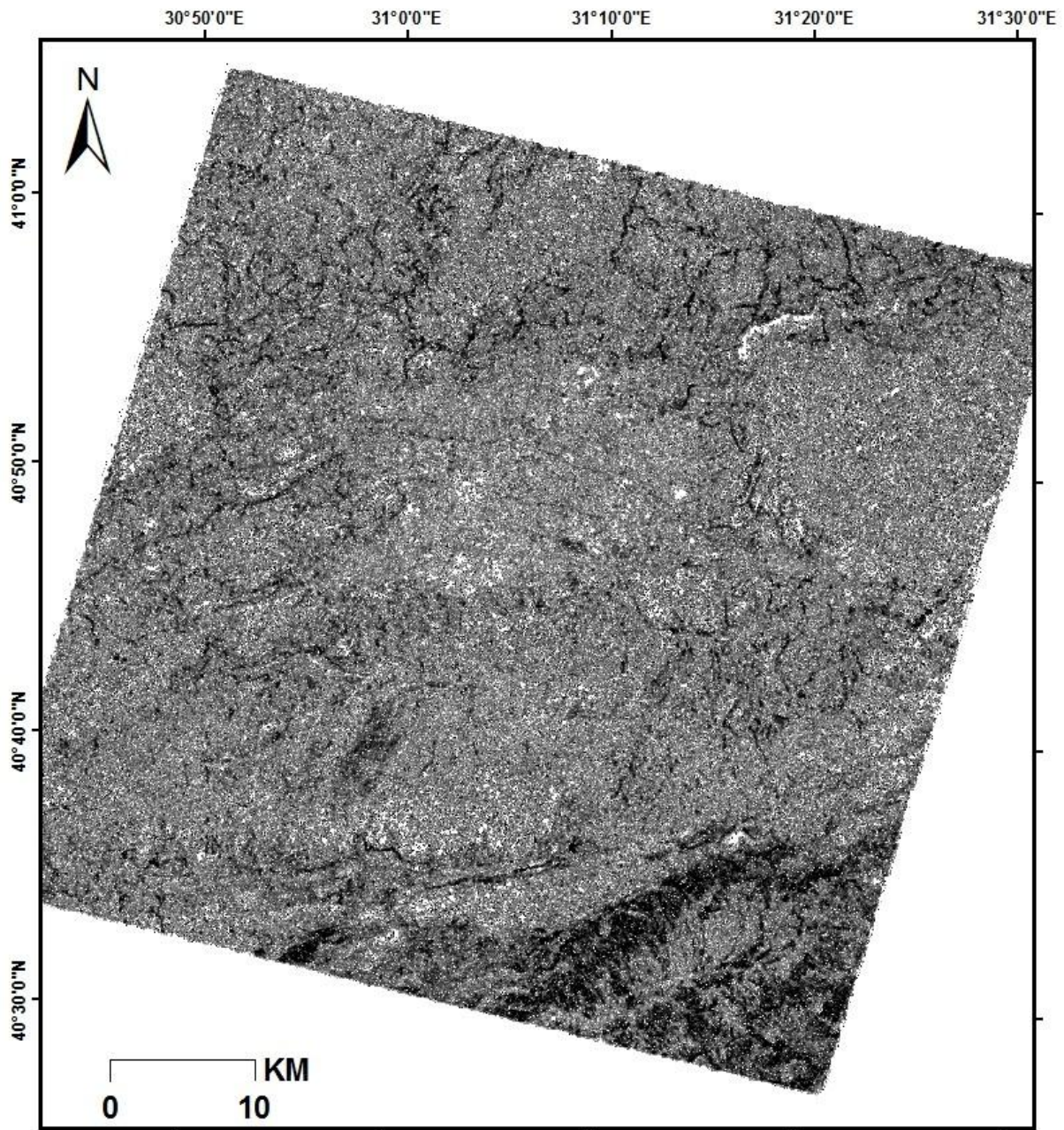
Figure 3-11 is showing SNR band of SPOT-1(03/10/99) and SPOT-4(12/07/2000) image correlation. Although SNR ranges from 0 to 1.0, here it is shown from 0.9 to 1.0 i.e. only better coherence.

4.   3-D SURFACE DEFORMATION MODEL

4.1 Existing 3-D Model

The satellites are called ascending and descending when it moves towards the North and South respectively. Four scalar components can be derived from SAR images if acquired from ascending and Descending track (Michele et al. 2010). For example, the same scene can be observed from the East during descending pass and from the West during ascending passes of ERS and Envisat. Therefore, with a single satellite, it is possible to obtain a 3-D geodetic measurement as observations from multiple look direction are available.
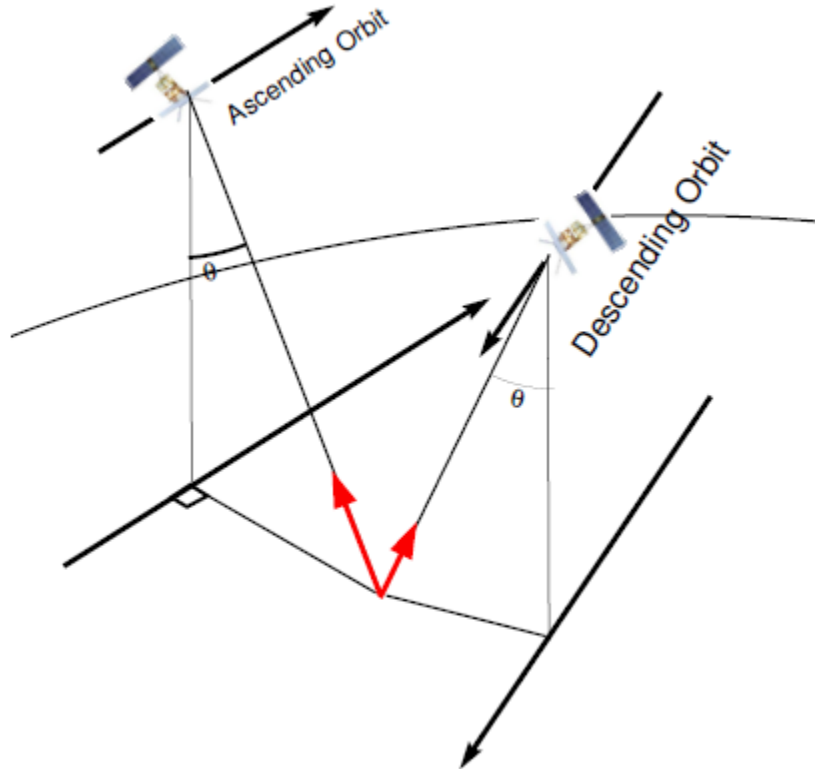
Figure 4-1 Simplified example of ascending and descending track SAR image acquisition (Bechor, 2006)

Wright et al (2004) narrate the procedure of mapping surface deformation in three dimensions from the interferograms having different (ascending and descending track) imaging geometries. The algorithm behind that was the calculation of pixel by pixel deformation by applying the least square solution. Say, $\hat{E}$ be the unit row vector (Ex, Ey, Ez) pointing from the ground to the satellite in local East, West, and Up direction. Then the line of sight displacement will be defined by r=-$\hat{E}$u, where u is the column vector $(u_x, u_y, u_z)^T$; containing the vector components in the same reference frame. If satellites from ascending and descending tracks observe any point on the ground, then the line of sight displacement from different look directions, R=$(r_1, r_2, r_3, r_4)^T$ can be defined as R=Eu, where E is the 4×3 matrix.

$$E = \begin{pmatrix} \hat{E}1 \\ \hat{E}2 \\ \hat{E}3 \\ \hat{E}4 \end{pmatrix}$$

If the observed range changes' covariance matrix for errors is $\sum_R$, then the least squares (maximum likelihood) solution for u can be expressed

Û=-[E^T$\sum_R^{-1}$ E]$^{-1}$E^T $\sum_R^{-1}$R

Where, [E^T$\sum_R^{-1}$ E]$^{-1}$ is the covariance matrix for the estimated vector components.

Briefly, least square provides a better solution for 3D decomposition in the situation of more known equation than unknown variables. In the above case, the line of sight is well known but Up, East, and North components are estimated and/or unknown. This is the typical situation of InSAR measurement. In this case, the least square solution reduces the distance among different equation and brings them closer to intersects onto a single point i.e. search for the desired solution.

Another relevant study can be mentioned here for further clarification. Wang et al (2007) explain the way of the derivation of complete 3-D displacement field by the inverted least square method. They have explained like this: the vector u=$[u_e u_n u_u]^T$ is represented by three orthogonal components of displacements (e.g. east, north and up) in the local coordinate system and displacements in the range and azimuth direction are represented by d=$[d_r d_{az}]^T$. If they are all in same reference frame, the transformation from u to d can be expressed as

d=s.u

where, s is the unit vector $s=\begin{bmatrix} cos\alpha sin\theta & -sin\alpha sin\theta & -cos\theta \\ sin\alpha & cos\alpha & 0 \end{bmatrix}$ ----------(4-1)

and α is the azimuth of the satellite heading vector (positive clockwise from the north) and θ is the radar incident angle at the reflection point.

A complete 3-D displacement field can be inverted by the least-square method:

U=(s^{T}Ps)$^{-1}$s^{T}Pd, where P is the weight matrix for the observations. Another issue can be made clearer here. In equation 4-1, the vertical sensitivity of LOS component i.e. cos (incidence angle) is negative, that is contrasting with (Fialko et al., 2001) where positive sign is being used. Feigl et al (2002) pointed out that the sign convention for s should be adjusted according to increase or decrease of range change (i.e. upward and downward movement).

Pathier et al. (2006) constructed 3-D surface displacement field (figure 4-2) from SAR pixel/offset tracking by adapting the strategy that (Wright et al., 2004) has proposed for 3D decomposition. Displacements are measured from azimuth and range offset data which were obtained from both ascending and descending passes of satellites. So the measurement was taken only those points which have vector components owing to different viewing geometries.

Earlier, this approach of the least square solution was usually being selected during 3-D surface displacement model preparation. Some other well-cited 3D surface deformation studies (Wang & Jónsson, 2014; Wright et al., 2006; Sandwell et al., 2002) can also be brought up here. However, in the present study, a different approach is adapted to prepare the 3-D surface deformation model which is going to be explained in the following section.
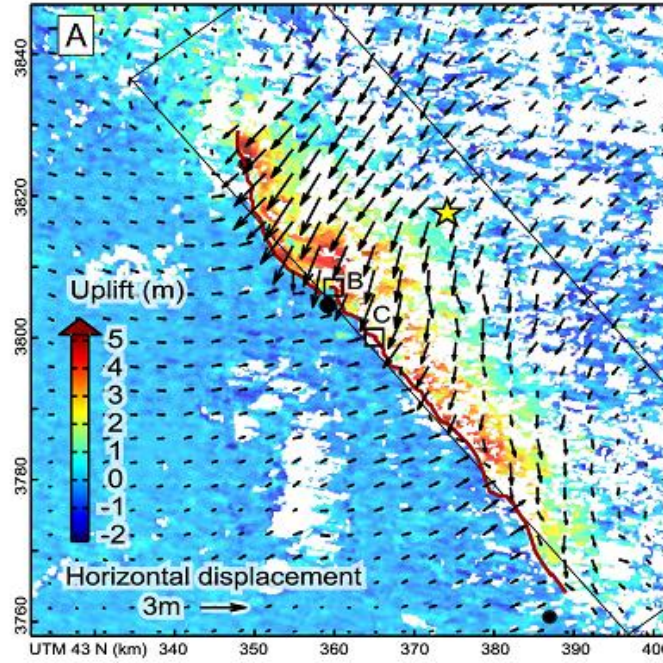
Figure 4-2: 3-D Displacement field for Kashmir (2005) earthquake derived from offset tracking of SAR imagery. Arrow is representing horizontal shift and color quantifies vertical shift. Star is the epicenter of the main shock and the red line is the rupture from Kashmir earthquake. Source: (Pathier et al.,2006).

4.2 3-D Model Prepared from the Current Research Work

Hanssen (2001) schematically (figure 4-3) shows the decomposition to derive vertical component from LOS, East, and North components. For instance, a displacement vector with three components (*dn, de and du)* in North, East and Up direction respectively is projected to the line of sight. For a satellite orbit with a heading azimuth (α_h), the line of sight can be found as:

*dr= du cos (θ_{inc}) – sin (θ_{inc}) [dn cos(α_h – 3π/2) + de sin (α_h – 3π/2)]-----------(*Equation 4-2*)*
This equation can be simplified as,
*dr = du cos (θ_{inc}) – sin (θ_{inc}) [de cos(α_h) – dn sin(α_h)]-----------------------------(*Equation 4-3)
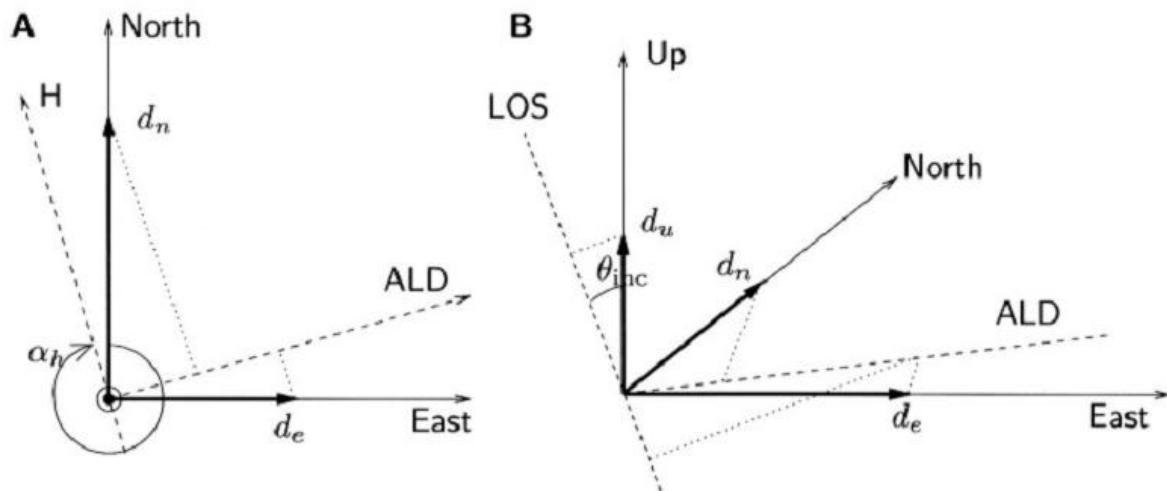
Figure 4-3 is showing the projection of three components from the satellite line of sight. (A) North and East components projection on the azimuth look direction (ALD) is seen from the top view (B) projection

of vertical component *(du)* to the line of sight via incident angle (θ_{inc}). Where, d_{ALD}= *de cos(α_h) - dn sin* (α_h). **The concept along with the sketch is taken from** (Hanssen, 2001).

Despite the fact that InSAR observation is mostly sensitive to the vertical component, converting a line of sight component to vertical while ignoring horizontal components will be resulted in an error (Samieie-esfahany et al., 2010). And this error will be Δ**u =** *tan (θ_{inc}) [de cos(α_h) - dn sin (α_h)]*

$$= tan\ (\theta_{inc}) \times d_{ALD} \quad \text{-------------------------}\text{(Equation 4-4)}$$

So, the minimum error will be zero when the horizontal components are perpendicular to ALD and maximum error be counted when the horizontal motion is parallel to the ALD.

However, in the current research work, the vertical component of displacement is obtainable as the contribution of horizontal components can be integrated with LOS component. And this can be explained in the following manner:

From the sub-pixel correlation of SPOT imagery, two true horizontal components are derived (EW and NS). Assuming these two horizontal components can substitute the *de* and *dn* in the equation 4-3; then it is possible to get the true vertical component as all other parameters of the equation (4-3) are known from the present study. Therefore, instead of following least square solution approach, three different but complementary datasets (LOS from InSAR; EW & NS from optical sub-pixel correlation) are being utilized in a simple linear equation (4-3) to derive the true vertical displacement field in the present study. It is to note that all the LOS unit vector coefficients are spatially dependent, and during calculation, each pixel is taken into consideration separately.

At this particular stage of the current research, it is noteworthy to mention that Barisin et al (2009) also construct 3-D surface displacement model for the 2005 rifting event on the Dabbahu segment in the Afar valley integrating sub-pixel analysis of SPOT-4 images result with InSAR measurement. They utilize the horizontal components of displacement derived from SPOT-4 images to account for the contribution of horizontal components to line-of-sight displacements from SAR Interferogram. The same LOS measurement what has been obtained by (Wright et al., 2006) was being utilized in the study of (Barisin et al., 2009). However, the LOS map from descending (due to its greater coverage) track was utilized for 3D decomposition and the gaps (formed due to decorrelation) within the line of sight map were filled up from range offset output. Although the 3-D model significantly improves compared to (Wright et al., 2006), Barisin et al (2009) acknowledged that the findings in that study need field validation. And figure 4-4 and 4-5 illustrate the findings from both studies.

Figure 4-4 shows the 3-D displacement field derived from the results of InSAR and SAR offset tracking. The vertical component of displacement is shown in the color ramp and horizontal displacement is shown in arrows. Here, to derive the vertical displacement field, Wright et al (2006) have followed the least square solution approach.
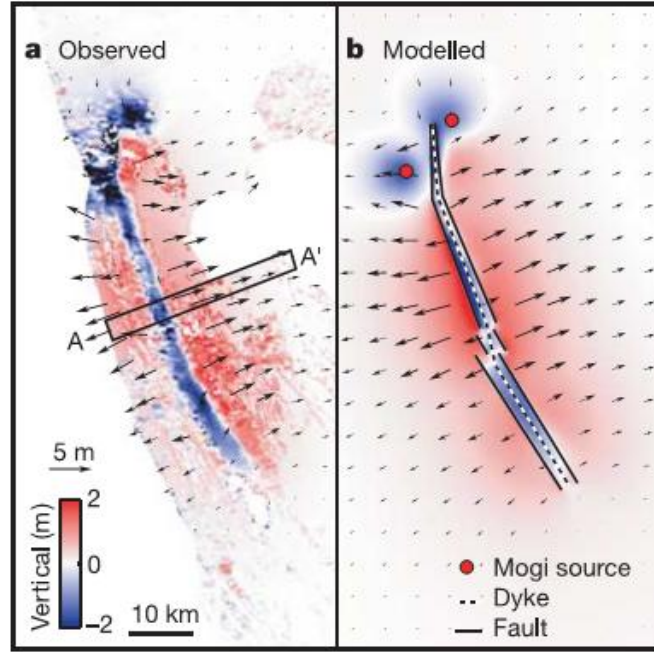
Figure 4-4(a) Observed and (b) modeled 3-D Displacement field for 2005 Dabbahu rifting episode. (a) 3-D Displacement field is derived from InSAR and offset tracking (range and azimuth offset) measurement. Arrows show the horizontal displacement and color ramp quantifies the vertical deformation (Wright et al., 2006)**.** AA´ cross section is not shown in the present study.

To improve the 3-D model of (Wright et al., 2006) by adapting a different approach, (Barisin et al., 2009) presented 3-D deformation model for the same rifting event. The contribution of horizontal components in the LOS component is accounted with the aid of NS and EW components derived from the sub-pixel correlation of SPOT-4 image pairs; thus, true vertical component is obtained (figure 4-5-e).
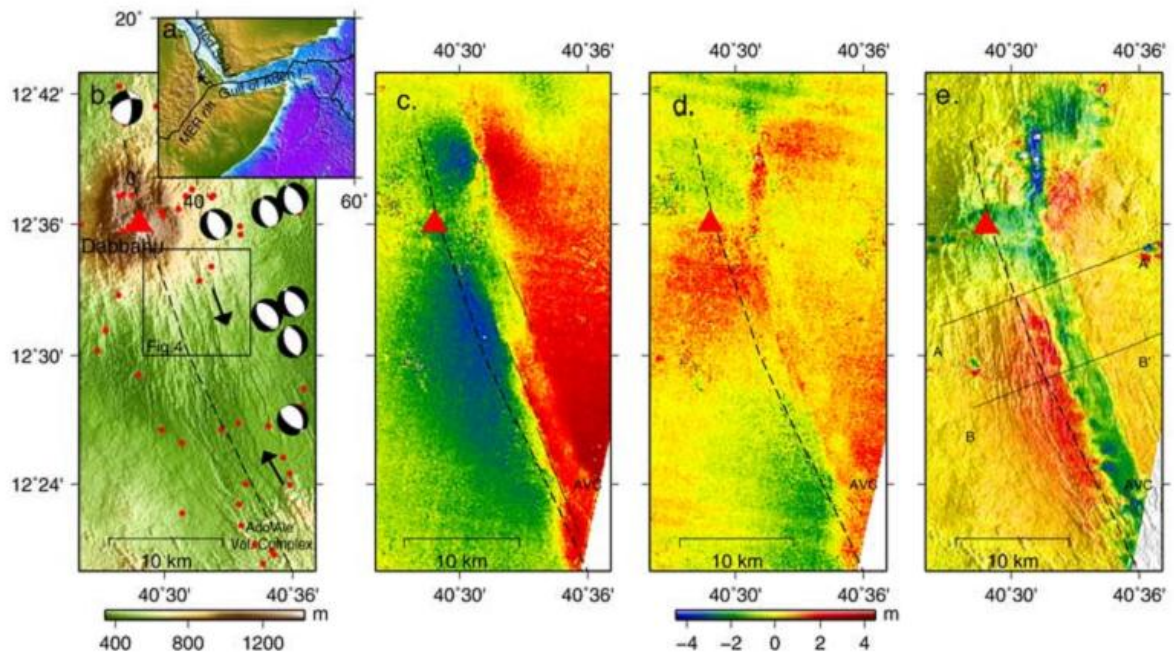
Figure 4-5: a. Location of Dabbahu rifting event (2005) along with fault plane solutions. Sub-pixel correlation results from SPOT-4 images are shown in c (EW displacement) and d (NS displacement).

Vertical displacement (e) is derived from EW and NS displacement and InSAR LOS displacement map. Source: (Barisin et al., 2009). AA´ and BB´ profiles are not shown in the present study.

The current research has the similar input what (Barisin et al., 2009) had. Hence, a true vertical component of deformation is derived by putting EW and NS horizontal components (obtained from the SPOT images cross-correlation) in the place of de and dn in equation 4-3 to account for the contribution of horizontal components from LOS (line of sight). Before decomposing the vertical component, three input maps (EW, NS and LOS) are being layer stacked to make exactly the same pixel resolution and the unit of LOS map is also converted from radian to meter. And the result is shown in figure 4-7. In connection, it is important to mention that before integration of COSI-Corr EW and NS (region of interest) components with the line of sight map (figure 3-5), non-local means filter (Ayoub et al., 2009) is applied to denoise the two horizontal components. During denoising, the default parameters (non-local means parameter: noise parameter 2, a search area 41, average weighting method, median filter 5×5) are chosen according to COSI-Corr user manual. The noise is significantly suppressed (as the snapshots figure 4-6 look smoother and homogeneous than its non-filtered counterpart but due to the averaging effect of filtering, the displacement values are reduced a bit (histograms of figure 4-6).
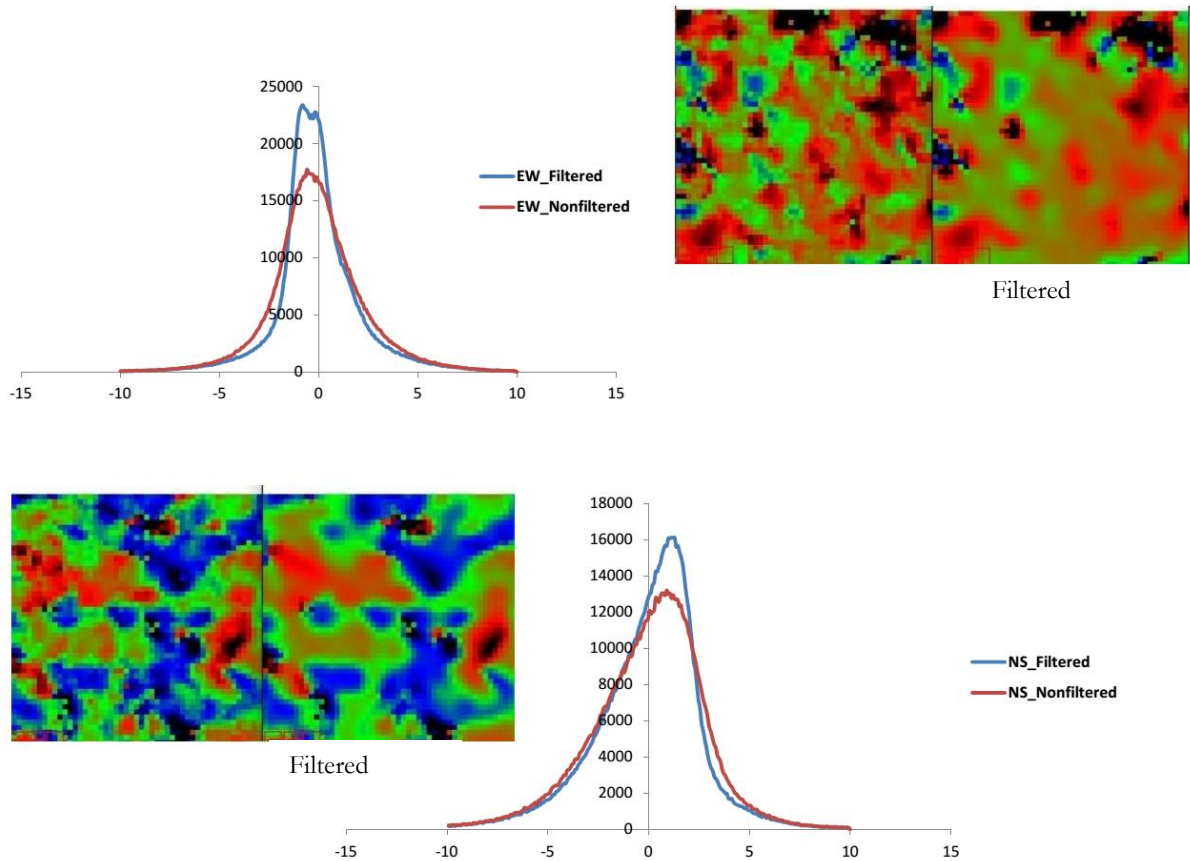
Filtered

Filtered

Figure 4-6 the effect of applying non-local means filter on EW and NS displacement map. The left snapshots for both cases are the non-filtered ones. The histogram is showing the displacement values against the number of samples.

Figure 4-7 (a) is the filtered subset of EW displacement map (figure 3-9). The same region of interest (figure 4-7 b) is selected for NS displacement field from the figure 3-10. These two horizontal inputs are used to account for the contribution of horizontal components to the satellite line of site component (figure 3-5 whose unit is converted into meter before 3-D decomposition).

Figure 4-7 (c) shows the vertical deformation field. The discontinuity from Düzce rupture is clearly visible. A negative value means surface moves downward i.e. subsidence and positive values indicate upliftment of the surface. Overall, the northern part of Düzce rupture moves downward compared to the southern part.
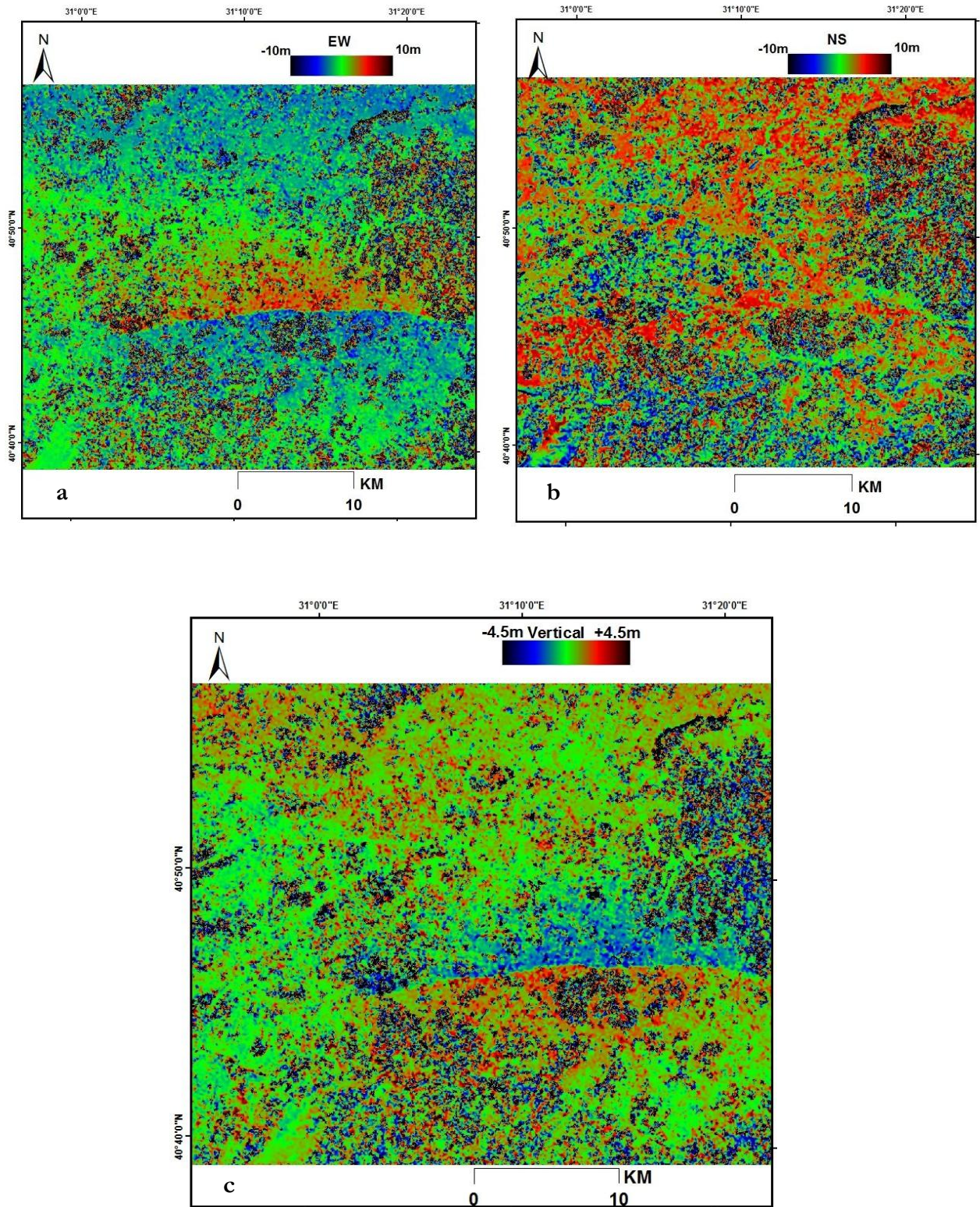
Figure 4-7 shows the (a) EW and (b) NS displacement field. (c) the vertical displacement field is obtained from the LOS from InSAR; EW and NS components from SPOT image cross-correlation

Another approach, however, do exist to derive true vertical component directly from the line of sight component. If the deformation occurs only in vertical direction (assumed), according to the figure (figure 4-8) below, the vertical deformation (Δh) can be obtained by $\Delta h = \frac{\Delta Rd}{\cos(\theta i)}$ (Zhiyong et al., 2009) ; where ΔR_d = line of sight deformation; θi is the incidence angle
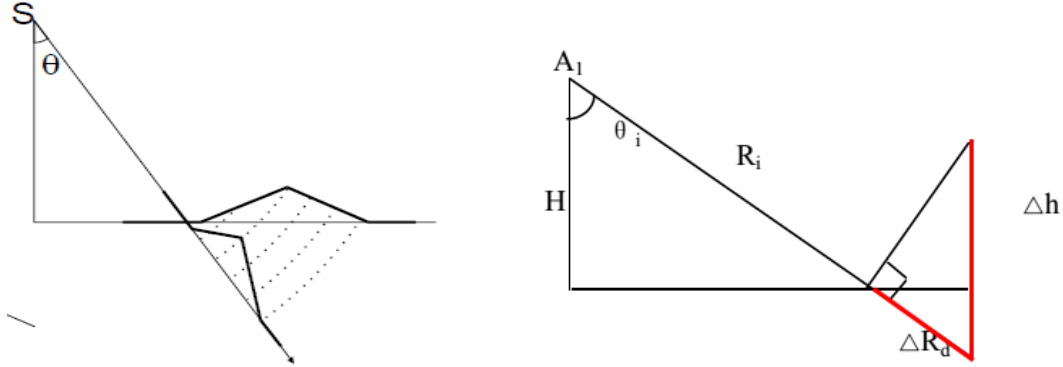
Figure 4-8 vertical component derivation from LOS; modified from (Zhiyong et al., 2009)

However, Zhiyong et al (2009) suggest that this assumption needs further study. Yet, adapting the same approach, the true vertical field for Düzce event (figure 4-9) is derived. The following figure (figure 4-9) shows the 3-D displacement field: vectors are showing the horizontal deformation field obtained from the sub-pixel correlation of SPOT Imagery and underlying vertical displacement field is derived by normalizing the line of sight displacement (which is is in radians) by cosine incident angle. Prior to deriving displacement map in meter, an offset of no deformation is taken from the southeastern edge (considering nearly zero deformation) of figure 6-5 and is added during conversion from radian to meter. It is already mentioned during explaining the figure 3-5 that, for the present context, the positive vertical values mean surface moves away from satellite along the line of sight direction and hence subsided. Figure 4-9 shows that the northern side is subsided compared to the southern part. The vector field which is the resultant of EW and NS displacement map from the COSI-Corr results (figure 4-7 a and figure 4-7 b) is overlaying the vertical displacement map constructed adapting (Zhiyong et al., 2009) approach.
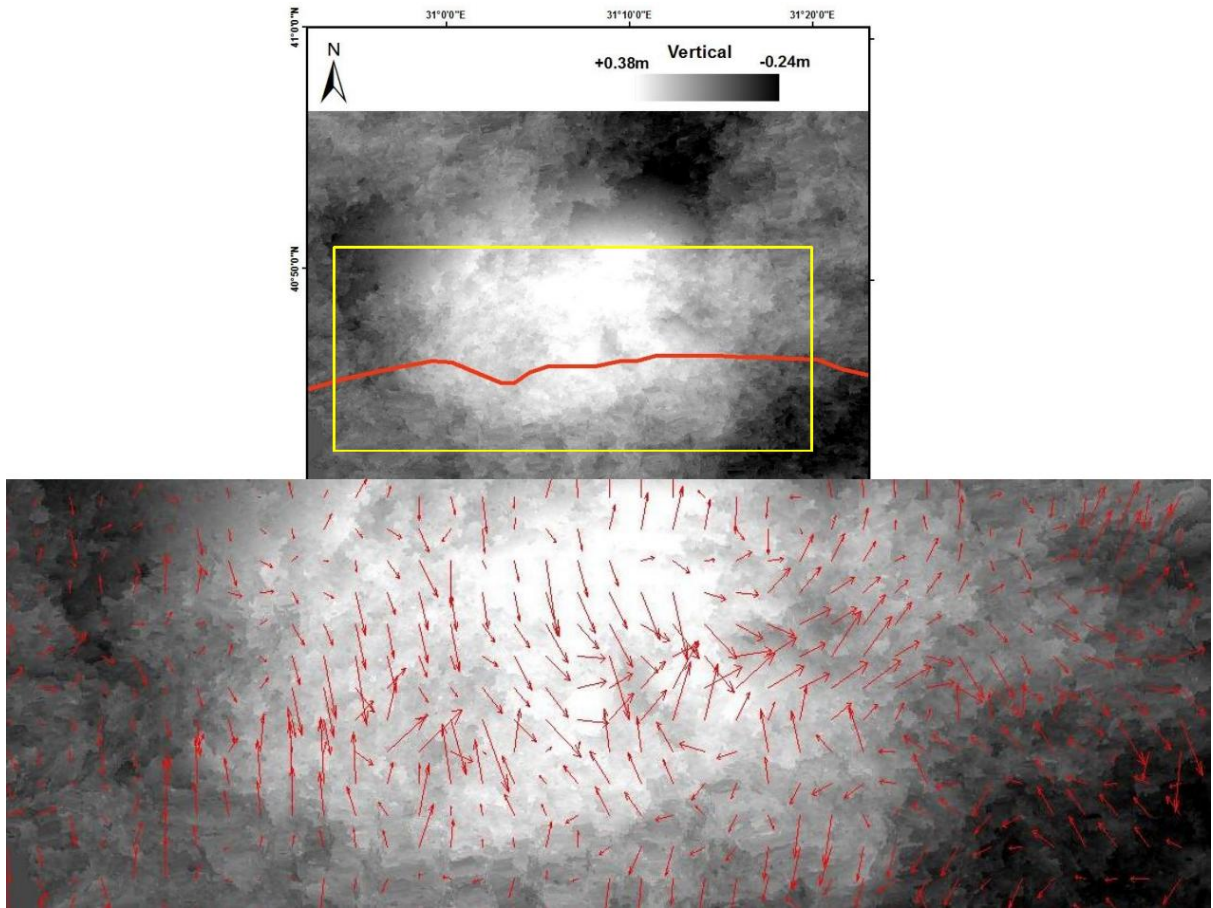
Figure 4-9 Vertical displacement map derived by normalizing LOS component. Maximum and minimum displacement are +0.38m and -0.24m. The bottom part is showing the resultant vectors of NS and EW optical bands (derived from sub-pixel correlation) overlaying the vertical deformation field (within the yellow box). The red line is the rupture caused by both Izmit and Düzce event.

5. DISCUSSIONS

5.1 Validation

During Düzce event, mainly Almacik and the North-Eastern tip (a small area) of Karadere fault is uplifted and Akyazi and Golayaka basin is subsided (Pucci et al., 2007). Some other studies have also specifically mentioned the slip distribution from Düzce rupture. The 40km long surface rupture by Düzce event is accompanied with ~500cm right-lateral offset (averaging 300cm) and maximum 350cm vertical displacement (normal faulting) (Akyüz et al., 2002). Overall, the Efteni Lake section is characterized by dominant vertical offsets and easternmost part of Düzce rupture is possessing mainly right-lateral offsets (Pucci et al., 2006).
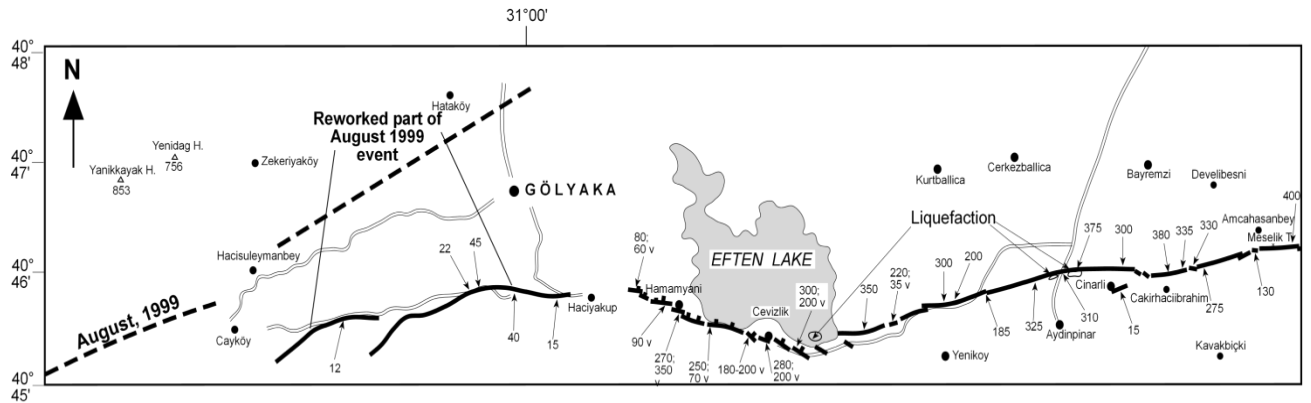
Figure 5-1 shows the field measurement along the fault. Vertical offset is designated with v along with numerical displacement value and the horizontal offsets are designated in numbers only. All the measurements are in centimeter. It is evident that the vertical deformation is prominent in the southern proximity of Eften Lake and the eastern side of Düzce rupture is mainly characterized by dominant right-lateral offset. Figure courtesy: Dr. H. Serdar Akyuz

The prepared vertical and EW horizontal displacement maps have good agreement with the above-mentioned studies. From figure 5-2 (blue color corresponds to subsidence and red is upliftment), it is evident that the northern part of Izmit-Düzce rupture is subsided and Almacik block is uplifted. Golyaka wedge basin which accommodates Eften lake is also subsided. Although some previous studies (e.g. Pucci et al., 2007) have claimed that the North-Eastern tip of Karadere fault is uplifted but this is not very clear from the prepared model. Higher resolution optical images might need to observe this. In terms of right lateral movement, the eastern part (from figure 4-7a) of Düzce fault seems to have (visually) more displacement.
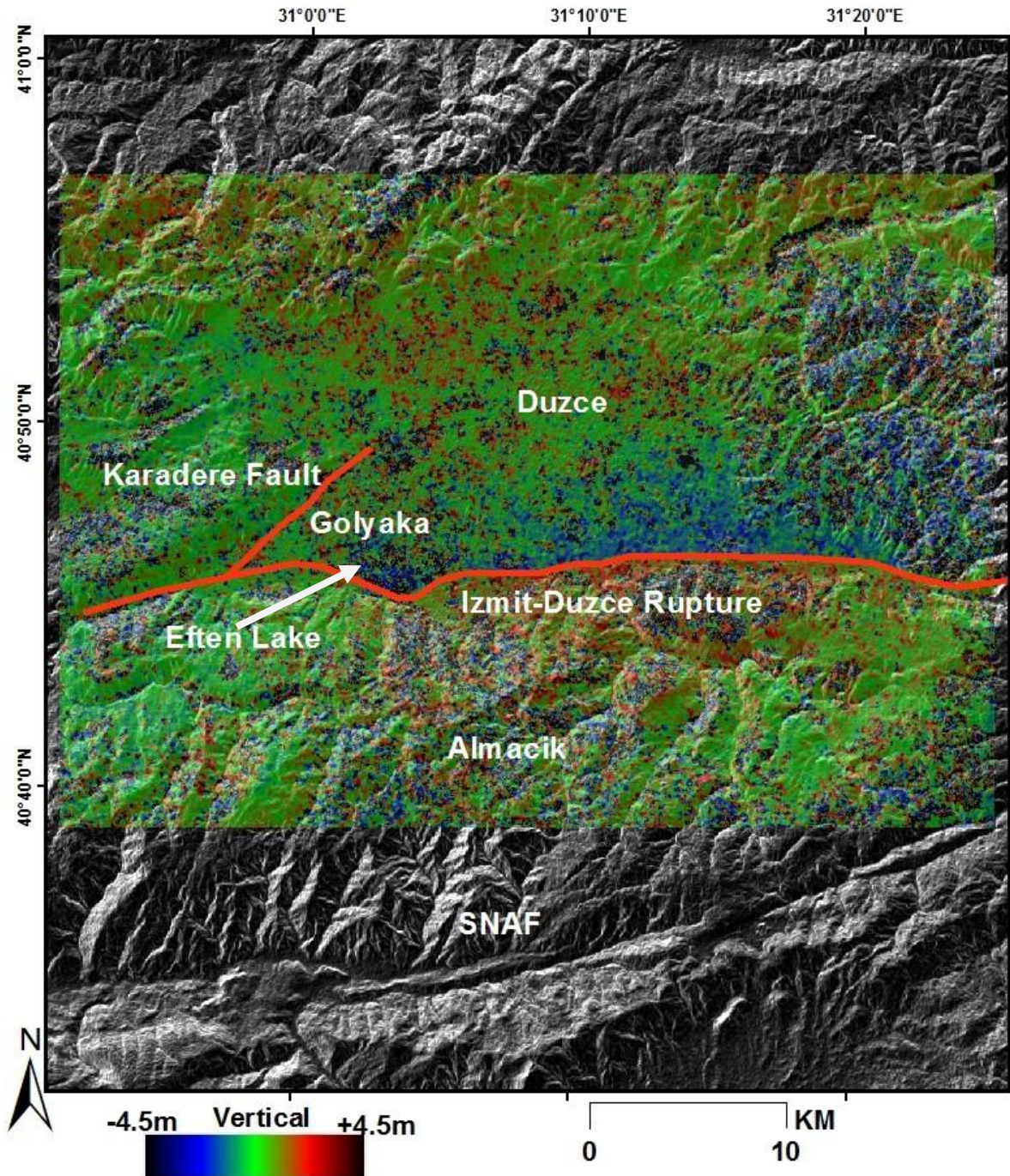
Figure 5-2 The vertical displacement map (figure 4-7-c) overlaying the shaded relief (constructed from SRTM 1 Arc Sec DEM). The positive values mean surface is uplifted and negatively value is for subsidence. Some important structural and geomorphic features are named in white. SNAF is the southern segment of North Anatolian Fault

Now it's time to move from qualitative to quantitative validation. The right lateral and vertical field displacement measurements (151 and 122 locations respectively) have been collected through the personal communication with Dr. Stefano Pucci. This field measurement is being compared with the prepared horizontal and vertical displacement map. At this point of the current study, it is reiterating that, the vertical displacement maps are obtained adapting two different approaches: one integrating COSI-Corr horizontal components with the line of sight measurement and another one is directly normalizing

the line of sight component by cosine incident angle. Here the reason for selecting the first approach is outlined. The second approach has come up with a displacement range far from the reality as the maximum and minimum value is +0.38m and -0.24m. Moreover, the motive for choosing the first approach can be explained in the following manner:

X=regression between field data and vertical component (derived integrating COSI-Corr results)

Y=regression between field data and vertical component derived by normalizing LOS unwrapped interferogram by cosine incidence angle

Z= regression between two derived vertical components
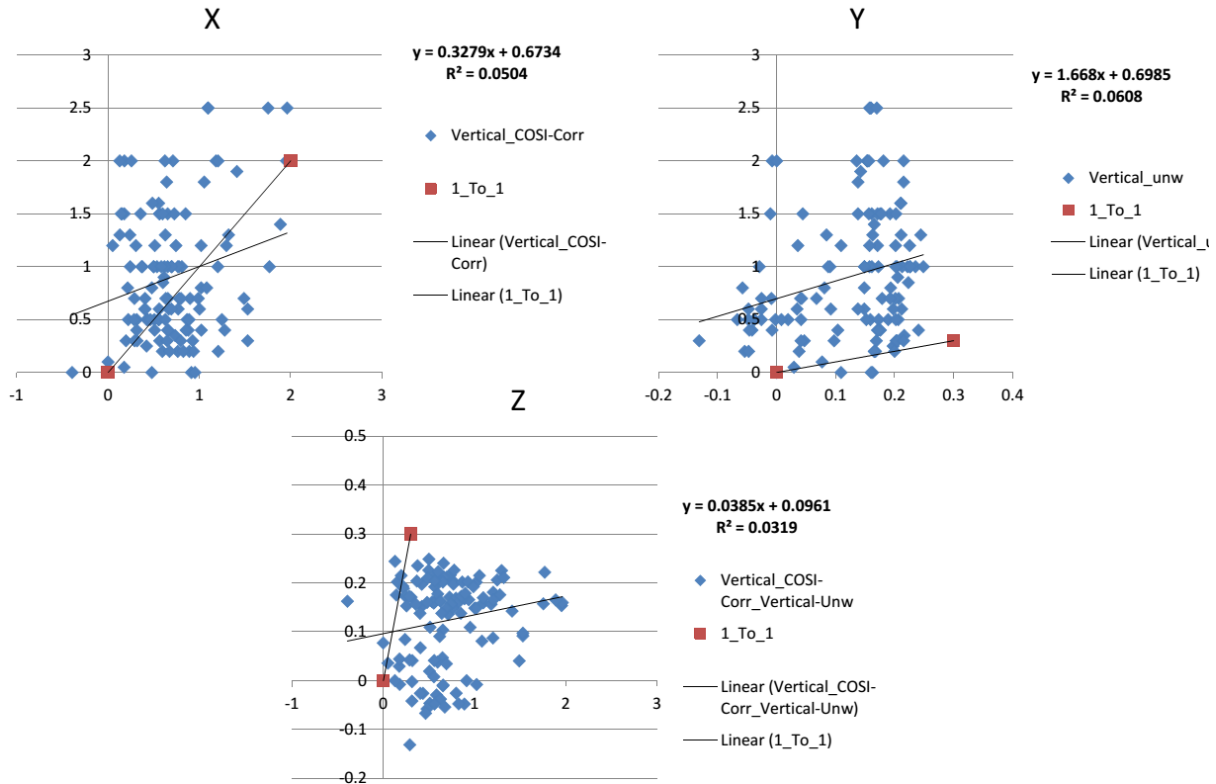
Figure 5-3 is showing the regression between X, Y and Z. For each case, a line is drawn between zero deformation and maximum extracted deformation and is designated as "1_To_1"

Regression is a statistical measure to show the relation between two or more variables (Stein et al., 2002); the higher (closer to 1) the R² value the better the regression model will be able to explain the variation. For the above regression analysis (figure 5-3) none of the X, Y and Z is showing a better regression; however, the tendency of the points to spread on the both side of ("1_To_1") line in case of X is comparatively better than Y and Z. This "1_To_1" line is drawn between zero and maximum extracted (from the prepared models) displacement value.

It is to mention that the above vertical displacement values are extracted along the Düzce rupture. And LOS component has a strong influence to obtain this vertical displacement field. In the context of present study, phase unwrapping was less than sufficient level of accuracy. The aim of phase unwrapping is to reduce the areas where the gradient of wrapped and unwrapped phase differs. The assumption between most of the phase unwrapping is that the neighboring phases of true unwrapped interferogram vary by one-half cycle (π) radian (Chen & Zebker, 2000). But this is not always the case. Hence, unwrapped interferogram sometimes quantifies ground deformation with astounding accuracy and sometimes far less than adequate. The unwrapping practice carried out in the present study is bearing the

accuracy less than adequate. And the reason is expectable as Düzce event is exhibiting highest slip to rupture ratio compared to any other major historical earthquake occurred from the North Anatolian fault (Akyüz et al., 2002). In addition, Düzce is characterized by multiple ruptures and the vertical displacement was pretty high and the biggest source of noise might emerge from this large displacement. It has already mentioned that (Bürgmann et al., 2002) and (Çakir et al., 2003b) have also investigated Düzce rupture through InSAR analysis and in none of these two studies, SAR Interferogram was unwrapped. So comparatively low vertical displacement derived from unwrapped interferogram is not an unexpected case.

However, the comparison of vertical components with GPS measurements has an excellent story to deliver. The GPS data for Düzce coseismic vertical displacement is available at (http://seismo.berkeley.edu/~burgmann/RESEARCH/TURKEY/turkey.html). Ten GPS points fall within the prepared vertical displacement fields. As GPS points are mostly located (eight out of ten) far from Düzce rupture, they should have less unwrapping influence. The figure below supports this statement as the R^2 value for the case X (figure 5-4) is now significantly improved. Despite Y has better R^2 value (figure 5-4) than X; but X is exhibiting the displacement value close to the GPS data and the algorithm for the derivation of this vertical components utilizing LOS, EW and NS components has a mathematically proved background (Hanssen, 2001) and does not need any assumption to take into account. Hence, the current research recommends this approach and the remaining discussion will continue dealing with this vertical component.
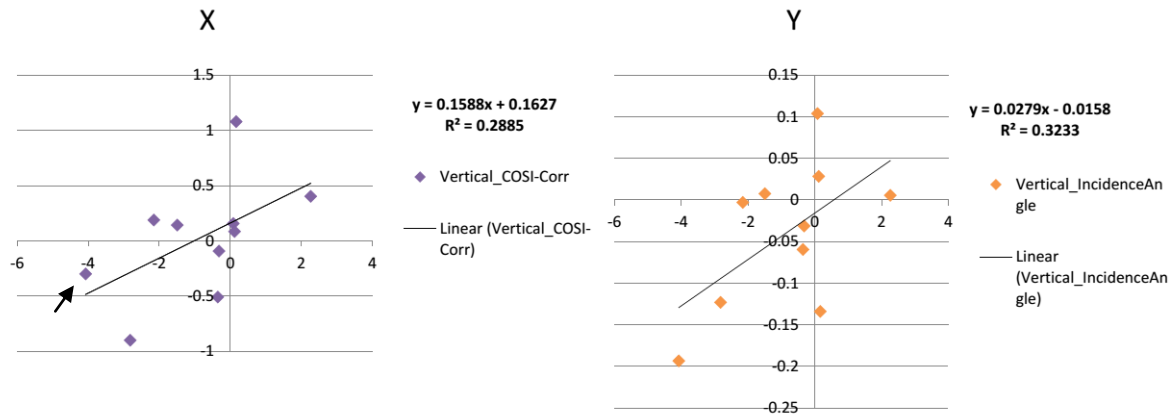
Figure 5-4 is showing the regression of X and Y. In this case, the extracted vertical values are compared with GPS data instead of field measurement

In the figure 5-4, the left most vertical displacement value (pointed with black arrow) from GPS measurement (for case X) is relatively higher (close to -4m). Because this particular point is located near to the epicenter of Düzce earthquake. Moreover, eight out of ten extracted vertical displacement values have the same trend. The remaining two are wrong looking; here the term "wrong looking" is used, for example, if the GPS shows positive value and corresponding extracted value is negative. With an inherent aim to reduce these wrong looking pixels, non-local means filtering is being applied on EW and NS optical displacement results.

The current research has also compared (figure 5-5) the EW displacement map with the field data collected by Dr. Stefano Pucci. The summary of the comparison is tabulated in table 5-1 (all units are in meter):

Table 5-1: Comparison of EW displacement with field data

Title	Maximum	Minimum	Average
Pucci et al (2006)	4.5	0	2.35
Extracted EW Displacement	6.67	-1.68	1.61

The average value between field and extracted right lateral displacement has dissimilarity. Two reasons might be responsible for that. Here the comparison is only with right lateral field measurement; hence all EW displacement values should be positive which means surface moves eastward. But about 6 % data (out of 151extracted data points) is exhibiting westward displacement i.e. negative. To remove this inconsistency, non-local means filter is applied on NS and EW map. Results are significantly improved after applying the filter that has been mentioned while explaining the figure 4-6, but due to the averaging effect of filtering, the displacement value is reduced a bit. Therefore, for the most of the points, due to the presence of negative value and averaging effect of filtering, the extracted values become a little bit less than the field measurement. From the figure 5-5 this explanation is also visible.
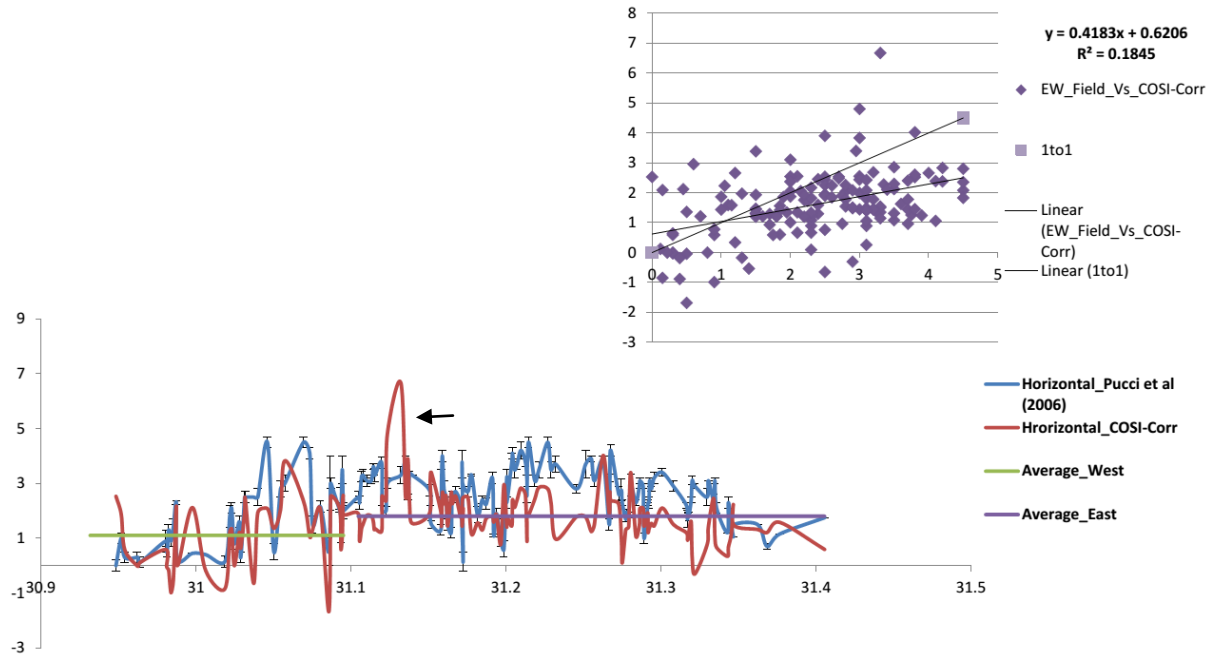
Figure 5-5 right lateral offset comparison between field data collected by Dr. Stefano Pucci and EW displacement results from COSI-Corr. The offsets are plotted against longitude (WGS84).

The Düzce rupture can be broadly divided into two parts: East and West based on the trend of the strike. Before 31.1° Düzce strikes mainly NE (North-East) direction and after that, the trend is mainly EW (figure 5-2). Compared to some previous studies like (Konca et al., 2010) and (Pucci et al., 2007); it is found that eastern part of Düzce rupture has suffered from more right lateral displacement than the western part. One extracted point in figure 5-5 has significantly high value (6.67m); channel and tree line is located on that particular point (indicated by arrow) which might have an influence on the COSI-Corr analysis. The second highest extracted EW displacement value is 4.2m which is identical with the field measured maximum value (4.5m). The R^2 and the tendency to spread from "1_To_1" line (figure 5-5) in this context are also reasonably good, considering the complex surface deformation scenario due to the earthquake. In this case, the comparison of right lateral displacement with GPS measurements has not

been shown as the optical image cross-correlation result is comparatively better close to the rupture area than the far fault and does not have 2π ambiguity like InSAR LOS measurement.

5.2 Interpretation

The analysis and validation part are now going to act as recipes during interpreting all results. The following discussion is organized in two parts: interpretation in terms of tectonic point of view and interpreting the results from a technical point of view.

The bilateral surface break (Bouin et al., 2004; Fatih et al., 2007) phenomenon due to the Düzce rupture is observed during the sub-pixel correlation of SPOT satellite images. The sub-pixel analysis results of figure 6-2 and 6-3 (attached in the appendix) bears the testimony of this bilateral surface rupture. At this point of discussion, it can be mentioned again that the Izmit and Düzce event occurred on 17 August and 12 November 1999. The EW displacement field (figure 6-2) from the image pair (dated 21/06/99 and 03/10/99) shows the EW rupture caused by Izmit event only. Although the termination part of Izmit rupture was reached within the footprint of that image pair, the surface break evidence is not so conspicuous (figure 6-2). But the EW displacement field (figure 6-3) from image pair (dated 21/06/99 and 12/07/2000) enveloping both Izmit and Düzce event clearly shows the effect of bilateral rupture phenomenon caused by Düzce event. Now the terminated rupture part (figure 6-2) of Izmit event becomes more pronounced after Düzce event. There is, however, a 10-15km overlap between Izmit and Düzce rupture (figure 6-3 and figure 2-2). Ergintav et al (2002) have interpreted the 298 days post-seismic behavior following Izmit earthquake as a rapid afterslip following the main shock and more steady long-term deformation due to the processes primarily act below seismogenic layer (10-15km). And the super-shear rupture from Düzce event reactivated surrounding secondary structures (Bouchon & Karabulut, 2008). These facts were the reason for spreading aftershocks in and around Düzce instead of concentrating along the fault. In terms of Düzce earthquake slip distribution, the model has an agreement with previous studies. Overall, the eastern part of Düzce fault exhibits more right lateral offset than the western parts. The derived EW displacement is also much more in the eastern part of the Düzce fault (figure 5-5) as the strike-slip motion was dominant in this particular part during Düzce rupture which has mentioned in chapter 2. In terms of vertical deformation, the northern side of Düzce rupture is subsided compared to the southern part. Due to dip-slip movement of Düzce fault around Eften Lake section, the maximum vertical displacement is observed (from field measurement) in this particular section. However, extracted vertical displacement from the present study (figure 5-6) does not have identical result in this Eften lake part and the reason behind that is transparent. Due to the presence of lake both optical and SAR measurements have suffered from decorrelation.

Average Field: 0.904   Maximum Field: 2.5m
Average Model: 0.703   Maximum Model: 1.96m
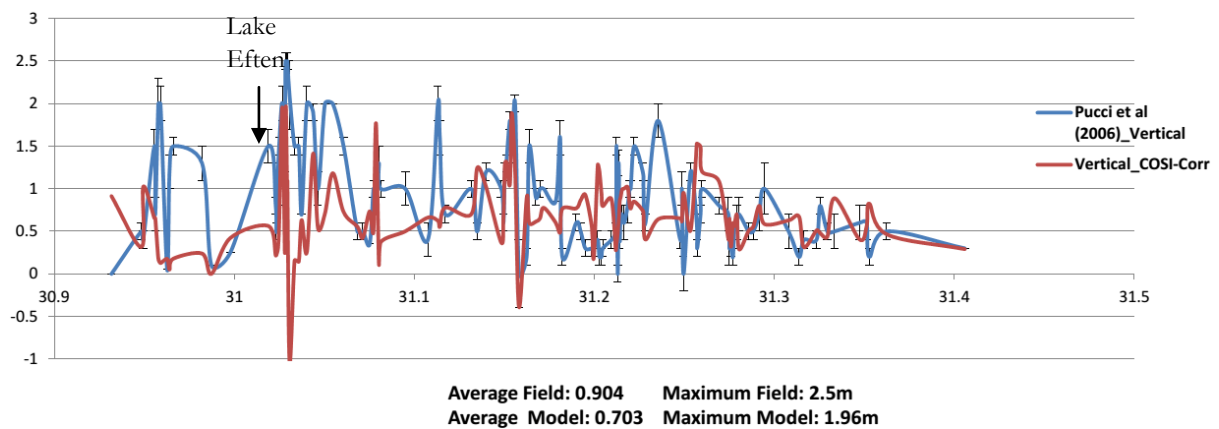
Figure 5-6 Comparison of field measurement (vertical) and extracted vertical displacement from figure 4-7 (c). The offsets are plotted against longitude (WGS84)

Technically speaking, the obtained vertical displacement field has better agreement with far field GPS measurement than along fault measurement. Still the maximum and average value is quite similar (figure 5-6). The extracted maximum and average value, however, are less than the field measurement. This might happen due to the averaging effect of filtering (figure 6-6) and presence of wrong looking pixels. Perhaps the noise suppression through filtering has improved all the results in one sense; by decreasing wrong looking pixels; otherwise, displacement measurement might have more variability.

The crucial part of the current research work was to figure out the means of integrating horizontal and LOS components to derive true vertical component. Although unwrapping of interferogram was not at that adequate level of accuracy, fortunately, the horizontal components from COSI-Corr have filled this drawback very nicely and have brought the result close to the reality. It can be reiterated that successful unwrapping might bring more expected vertical offset results. In many studies, this unwrapping problem has faced and it is always tricky to handle particularly when the large displacement occurs from earthquakes. In this kind of situation the conducted approach (integration of optical image cross-correlation and InSAR results for surface deformation analysis) to derive vertical displacement component might be a better solution to constrain vertical displacement measurement.

Undoubtedly, the 3-D surface deformation model prepared from the current research work is a new concept in the field of earth observation. However, the applicability of the prepared model still needs further study due to the presence of many limitations which is going to be narrating in the following section.

5.3 Limitation

The limits and potentiality of the prepared 3-D model have been evaluated in the validation part. It has no denying that the current research work needs further study and this creates new scope to research for an improved integration of two different techniques (sub-pixel correlation of optical imagery and InSAR). But it has limited applicability in many cases. It is very difficult for any region to find two images of the same scene except for SPOT (HRV1 & HRV2) as other sensors like Quickbird, Ikonos, IRS-Ic etc do not possess the duplicate of their instrument (Sébastien Leprince, 2008). In the present study, SRTM DEM (30m resolution) was utilized during the sub-pixel correlation of 10m resolution SPOT imagery. Availability of similar resolution DEM might enhance the accuracy of the result. In addition, temporal (cloud cover, landslides, building collapse) decorrelation was also responsible for degrading the correlation results in few parts. Although InSAR is a useful & relatively accurate geodetic technique but it suffers significantly from atmospheric influences (Jolivet et al., 2011; Ding et al., 2008). This is also true that limitation from atmospheric influence is difficult to solve with single Interferogram (Hanssen, 2001). Perhaps, atmospheric errors have not been taken into account during current research work. Since the study had to deal with large displacement exhibiting obscured interferometric fringes close to the fault, unwrapping was challenging to make the result to a sufficient level of accuracy. However, some other unwrapping methods might give a better solution. But the present study has tried to solve this problem only with SNAPHU. Moreover, the study has integrated two different techniques that have a different level of accuracy: LOS measurement from InSAR has centimeter-level precision (Peltzer et al., 2001), on the other hand, sub-pixel correlation technique provides meter level (Leprince et al., 2008). This topic of accuracy difference might become a stormily debated issue among scientists. The current study suppressed the noise both from SAR interferogram and correlated optical maps by inbuilt filtering present in ROI_PAC and COSI-Corr respectively. But within the research period, the optimal parameter for filtering was not perfectly figure out. Last but not least, the images (both optical and SAR) utilized in the present study span different time interval and hence had to face different surface and atmospheric interaction which might have effects on the results. This varying investigation period of InSAR and the sub-pixel correlation was unable to take into account the post Düzce aseismic deformation scenario. In connection, the obtained result is compared with field and GPS data, but the date of acquiring these data was also unknown.

One sentence might be enough to summarize the limitation of the study and that is the presented 3-D surface deformation model does complement but could not replace the field measurement if the limitations could not be overcome.

6. CONCLUSION AND RECOMMENDATION

6.1 Conclusion

Rupture length and slip distribution of moderate and large earthquakes depend on the geometric complexity of fault surface, local geology, tectonic loading preceding the event and rupture dynamics during the event (Elliott et al., 2016; Avouac, 2015). This rupture length and slip distribution can be measured from the current 3-D surface deformation model. From this study, it is found that Düzce event has created bilateral surface rupture propagates dominantly eastward. In terms of slip distribution, the eastern part of Düzce fault has more horizontal offset than the western part. Although there exhibits some discrepancy regarding the vertical slip distribution, the fact is clear that the hanging wall (northern) part of Düzce fault is subsided compared to the southern part.

The current research was conducted to figure out the way to integrate two different techniques (sub-pixel correlation of optical imagery and InSAR) and to assess the performance of the prepared 3-D surface deformation model with field data. The objectives are fulfilled and the research questions have found the answers at least to a certain extent; the optimistic author hopes so. However, the brief answers to the research questions are outlined as follows:

Question 1. How to integrate horizontal and vertical (LOS) surface deformation information derived from the sub-pixel correlation and InSAR respectively? Which parameters are more sensitive to this integration?

InSAR analysis has provided the line of sight displacement component for Düzce event. And NS and EW horizontal displacement components are derived from the sub-pixel correlation of SPOT imagery. A displacement vector with three components for every pixel in North (N), East (E) and Up direction is projected to the line of sight. To derive true vertical component, the contribution of horizontal components in the line of sight is accounted for. Assuming the EW and NS horizontal displacement components obtained from sub-pixel correlation technique will complement to that E and N component while integrating with the line of sight component from InSAR. Finally, the assumption becomes true and the vertical deformation field is derived.

LOS component is one of the most important parameters for this integration; however, it was far less than sufficient level of accuracy. It is also true that the denoising attempt has reduced the vertical displacement value a bit due to the averaging effect of filtering (figure 6-6). So these phenomena were the most sensitive issues during the integration of two different datasets. Technically, in the equation 4-2, two important parameters do exist i.e. satellite heading azimuth and incident angle. These two parameters have significant influence to derive vertical component from three other vector components (LOS, E, and N). Moreover, as two different data sets (optical and SAR) are being used during the decomposition of true vertical components; these are prepared as spatially dependent (with same pixel size) and each pixel is considered separately during calculation.

Question 2. Does the 3-D deformation model represent the continuous deformation scenario of the study area? What is the performance of this model compared to GPS measurement and/or field observations?

Although the prepared 3-D model has covered a small area close to the Düzce fault, the surface rupture and slip distribution is well represented. The rupture length is clearly visible and measurable. Overall, the northern part of Düzce fault is subsided compared to the southern part. In terms of horizontal surface deformation, the eastern part of Düzce rupture has experienced more right lateral displacement compared to the western part.The prepared model is validated with the field investigation of (Pucci et al., 2006) and GPS study conducted by (Bürgmann et al., 2002). The model has more agreement with far fault

GPS measurement than along fault field investigation.

Each study has two broad purposes i.e. scientific and economic. And these two purposes achieve value whenever people start to secure benefits. From a scientific point of view, the accessibility to noise free raw optical and SAR imagery & successful unwrapping will bring an added value to the prepared 3-D surface deformation model. This particular research topic might motivate other scientists who are solely concerned about either InSAR or optical image correlation technique to research further on this combining two dataset approach.

The world is now experiencing disasters with increasing numbers; particularly earthquakes are, nowadays, responsible for significant damage and noticeable life loss (Coppola, 2006). Sumatra, Kashmir, Bam, Sichuan, Tohoku and Nepal earthquakes are bearing the testimony of massive destruction. So the necessity for better understanding the surface deformation due to earthquakes is a demand of time. Current research has tried to contribute in earthquake slip distribution measurement and mapping surface rupture. This information can be utilized in various ways to save life and property.

6.2 Recommendation

Future always brings a better solution. The grand field of earth observation is also not different in this context. For instance, to provide routine earth observation data continuity of active sensors ERS, ENVISAT and as well as multispectral missions such as SPOT, Landsat, ATER etc, the sentinel missions are launched (F. Van der Meer et al., 2014). In 2002, Envisat was launched which carries sophisticated optical and radar instruments (Ferretti et al., 2007). In future, the availability of optical and SAR imagery acquired from optical and RADR sensor installed in the same satellite might reduce the uncertainty and limitations of the preparation of 3-D surface deformation model integrating the two techniques that current research has focused on.

In general, the optical image correlation results have larger noise than unwrapped interferogram. So combining these two will result in a model that has some wrong looking values. If more than three datasets were available in the current study, for example, unwrapped interferogram from the descending track, the current research might give it a try for a 3-D computation following least square approach which might provide a better result. It is also recommended to reduce the noisy displacement value from the input data sets by applying proper filtering (although in this study it has been tried but more efforts are required) before 3-D decomposition.

The interferogram unwrapping is always challenging and it was even more arduous during the current study. Interestingly, Chen & Zebker (2002) has presented a technique for applying SNAPHU to large interferograms (interferograms approaching or exceeding the limits of typical computer resources available for unwrapping them). In this study the wrapped interferogram is partitioned into arbitrarily shaped region relatively free from local unwrapping errors and then unwrapping them individually. Regions are then assembled through the use of topographically irregular network model. In connection, after unwrapping some parts might exhibit missing data values due to masking low coherence. Recently, Yaseen et al (2013) demonstrate the mean of filling up the missing value in the constructed interferogram by local level interpolation (kriging).

Interestingly, scattered horizontal surface deformation from GPS measurement can be integrated with InSAR line of sight component to derive vertical component of deformation (Biggs et al., 2009). In the case of insufficient unwrapping due to poor coherence, the reliable scattered areas from the prepared 3-D model can be obtained by masking out the low coherence. If GPS horizontal measurement is available in these masked out scattered areas too; it will offer to research further by comparing vertical components accounting GPS and COSI-Corr horizontal components.

The slip distribution due to earthquake varies with different geomorphic units. It might be an interesting topic to continue the current research to observe the slip distribution on different geomorphic units (geomorphic map is prepared by Dr. Stefano Pucci during his PhD research) in and around Düzce rupture. The same approach is also recommendable to other geologic settings. Moreover, a model secures acceptation when its performance in different geological settings achieves greater accuracy. The prepared 3-D surface deformation model is an output from strike-slip settings. It will be interesting to apply this in thrust fault settings and assess the performance of this model.

REFERENCES

Agram, P. S., & Zebker, H. A. (2009). Sparse Two-Dimensional Phase Unwrapping Using Regular-Grid Methods. *Geoscience and Remote Sensing Letters, IEEE*, *6*(2), 327–331. http://doi.org/10.1109/LGRS.2009.2012445

Akyüz, H. S., Hartleb, R., Barka, a., Altunel, E., Sunal, G., Meyer, B., & Armijo, R. (2002). Surface rupture and slip distribution of the 12 November 1999 Düzce earthquake (M 7.1), North Anatolian fault, Bolu, Turkey. *Bulletin of the Seismological Society of America*, *92*(1), 61–66. http://doi.org/10.1785/0120000840

Avouac, J. P., Ayoub, F., Leprince, S., Konca, O., & Helmberger, D. V. (2006). The 2005, Mw 7.6 Kashmir earthquake: Sub-pixel correlation of ASTER images and seismic waveforms analysis. *Earth and Planetary Science Letters*, *249*(3-4), 514–528. http://doi.org/10.1016/j.epsl.2006.06.025

Avouac, J.-P. (2015). *Mountain Building: From Earthquakes to Geologic Deformation. Treatise on Geophysics* (Vol. 6). Elsevier B.V. http://doi.org/10.1016/B978-0-444-53802-4.00120-2

Avouac, J.-P., Ayoub, F., Leprince, S., Konca, O., & Helmberger, D. V. (2006). The 2005, Mw 7.6 Kashmir earthquake: Sub-pixel correlation of ASTER images and seismic waveforms analysis. *Earth and Planetary Science Letters*, *249*(3-4), 514–528. http://doi.org/10.1016/j.epsl.2006.06.025

Ayhan, M. E., Bürgmann, R., McClusky, S., Lenk, O., Aktug, B., Herece, E., & Reilinger, R. E. (2001). Kinematics of the Mw=7.2, 12 November 1999, Düzce, Turkey Earthquake. *Geophysical Research Letters*, *28*(2), 367. http://doi.org/10.1029/2000GL011851

Ayoub, F., Leprince, S., & Avouac, J. P. (2009). Co-registration and correlation of aerial photographs for ground deformation measurements. *ISPRS Journal of Photogrammetry and Remote Sensing*, *64*(6), 551–560. http://doi.org/10.1016/j.isprsjprs.2009.03.005

Ayoub, F., Leprince, S., & Keene, L. (2009). User's Guide to COSI-CORR Co-registration of Optically Sensed Images and Correlation. *User Manual*, 1–38. Retrived from http://www.tectonics.caltech.edu/slip_history/spot_coseis/pdf_files/CosiCorr-Guide2015a.pdf

Bähr, H. (2013). *Orbital Effects in Spaceborne Synthetic Aperture Radar Interferometry*. P7; Retrieved from: https://www.google.nl/webhp?sourceid=chrome-instant&ion=1&espv=2&ie=UTF-8#q=B%C3%A4hr%2C+H.+(2013).+Orbital+Effects+in+Spaceborne+Synthetic+Aperture+Radar+Interfe rometry.+P7

Bamler, R., & Hartl, P. (1998). Synthetic aperture radar interferometry Synthetic aperture radar interferometry, *1*.

Barisin, I., Leprince, S., Parsons, B., & Wright, T. (2009). Surface displacements in the September 2005 Afar rifting event from satellite image matching: Asymmetric uplift and faulting. *Geophysical Research Letters*, *36*(7), 1–6. http://doi.org/10.1029/2008GL036431

Barka, A. (1992). The North Anatolian fault zone. *Annales Tectonicae*, *6*.

Bechor, N. (2006). *EXTENDING INTERFEROMETRIC SYNTHETIC APERTURE RADAR MEASUREMENTS FROM ONE TO TWO DIMENSIONS*. STANFORD UNIVERSITY.PhD Thesis.p14. Retrieved from: http://web.stanford.edu/group/radar/people/noa_thesis.pdf

Bechor, N. B. D., & Zebker, H. a. (2006). Measuring two-dimensional movements using a single InSAR pair. *Geophysical Research Letters*, *33*(16), 1–5. http://doi.org/10.1029/2006GL026883

Biggs, J., Burgmann, R., Freymueller, J. T., Lu, Z., Parsons, B., Ryder, I., … Wright, T. (2009). The postseismic response to the 2002 M 7.9 Denali Fault earthquake: Constraints from InSAR 2003-2005. *Geophysical Journal International*, *176*(2), 353–367. http://doi.org/10.1111/j.1365-246X.2008.03932.x

Biggs, J., Wright, T., Lu, Z., & Parsons, B. (2007). Multi-interferogram method for measuring interseismic deformation: Denali Fault, Alaska. *Geophysical Journal International*, *170*(3), 1165–1179. http://doi.org/10.1111/j.1365-246X.2007.03415.x

Bouchon, M., & Karabulut, H. (2008). The Aftershock Signature of Supershear Earthquakes. *Science*, *320*(June), 1323–1325. http://doi.org/10.1126/science.1155030

Bouin, M. P., Bouchon, M., Karabulut, H., & Aktar, M. (2004). Rupture process of the 1999 November 12 D??zce (Turkey) earthquake deduced from strong motion and Global Positioning System measurements. *Geophysical Journal International*, *159*(1), 207–211. http://doi.org/10.1111/j.1365-246X.2004.02367.x

Brown, L. G. (1992). A survey of image registration techniques. *ACM Computing Surveys*, *24*(4), 325–376. http://doi.org/10.1145/146370.146374

Bürgmann, R., Ayhan, M. E., Fielding, E. J., Wright, T. J., McClusky, S., Aktug, B., … Türkezer, A. (2002). Deformation during the 12 November 1999 Düzce, Turkey, earthquake, from GPS and InSAR data. *Bulletin of the Seismological Society of America*, *92*(1), 161–171. http://doi.org/10.1785/0120000834

Bürgmann, R., Hilley, G., Ferretti, A., & Novali, F. (2006). Resolving vertical tectonics in the San Francisco Bay Area from permanent scatterer InSAR and GPS analysis. *Geology*, *34*(3), 221–224. http://doi.org/10.1130/G22064.1

Çakir, Z., de Chabalier, J. B., Armijo, R., Meyer, B., Barka, A., & Peltzer, G. (2003a). Coseismic and early post-seismic slip associated with the 1999 Izmit earthquake (Turkey), from SAR interferometry and tectonic field observations. *Geophysical Journal International*, *155*(1), 93–110. http://doi.org/10.1046/j.1365-246X.2003.02001.x

Çakir, Z. Y. A. D. N., Barka, A. A., Chabalier, J. D. E., Armijo, R., & Meyer, B. (2003b). Kinematic of November 12, 1999 (M=7.2) Düzce Earthquake Deduced from SAR Interferometry. *Turkish Journal of Earth Sciences*, *12*(1999), 105–118.

Casu, F., Manconi, A., Pepe, A., & Lanari, R. (2011). Deformation time-series generation in areas characterized by large displacement dynamics: The SAR amplitude pixel-offset SBAS technique. *IEEE Transactions on Geoscience and Remote Sensing*, *49*(7), 2752–2763. http://doi.org/10.1109/TGRS.2010.2104325

Chen, C. W., & Zebker, H. a. (2000). Network approaches to two-dimensional phase unwrapping: intractability and two new algorithms. *Journal of the Optical Society of America. A, Optics, Image Science, and Vision*, *17*(3), 401–414. http://doi.org/10.1364/JOSAA.18.001192

Chen, C. W., & Zebker, H. a. (2001). Two-dimensional phase unwrapping with use of statistical models for cost functions in nonlinear optimization. *Journal of the Optical Society of America A*, *18*(2), 338. http://doi.org/10.1364/JOSAA.18.000338

Chen, C. W., & Zebker, H. A. (2002). Phase unwrapping for large SAR interferograms: Statistical segmentation and generalized network models. *IEEE Transactions on Geoscience and Remote Sensing*, *40*(8), 1709–1719. http://doi.org/10.1109/TGRS.2002.802453

Coppola, D. (2006). *Introduction to international disaster management*. *Vasa*. Elsevier Inc.pp14-23 Retrieved from http://medcontent.metapress.com/index/A65RM03P4874243N.pdf\nhttp://books.google.com/books?hl=en&lr=&id=s6oxEraqWWwC&oi=fnd&pg=PP2&dq=Introduction+to+International+Disaster+Management&ots=tQkh9B273s&sig=HOqjpkOH1Plt_SsuTc0K4m-lmI4

De Michele, M., Raucoules, D., De Sigoyer, J., Pubellier, M., & Chamot-Rooke, N. (2010). Three-dimensional surface displacement of the 2008 May 12 Sichuan earthquake (China) derived from Synthetic Aperture Radar: Evidence for rupture on a blind thrust. *Geophysical Journal International*, *183*(3), 1097–1103. http://doi.org/10.1111/j.1365-246X.2010.04807.x

Ding, X. L., Li, Z. W., Zhu, J. J., Feng, G. C., & Long, J. P. (2008). Atmospheric effects on InSAR measurements and their mitigation. *Sensors*, *8*(9), 5426–5448. http://doi.org/10.3390/s8095426

Dominguez, S. (2003). Horizontal coseismic deformation of the 1999 Chi-Chi earthquake measured from SPOT satellite images: Implications for the seismic cycle along the western foothills of central Taiwan. *Journal of Geophysical Research*, *108*(B2), 2083. http://doi.org/10.1029/2001JB000951

Elliott, J. R., Jolivet, R., González, P. J., Avouac, J.-P., Hollingsworth, J., Searle, M. P., & Stevens, V. L. (2016). Himalayan megathrust geometry and relation to topography revealed by the Gorkha earthquake. *Nature Geoscience*. http://doi.org/10.1038/ngeo2623

Erdas, I. (1997). *ERDAS Field Guide. Imagine*.pp645 Retrieved from http://www.gis.usu.edu/manuals/labbook/erdas/manuals/FieldGuide.pdf

Farr, T., & Al, E. (2001). The shuttle radar topography mission. *Eos Trans. AGU*, *82*(2005), 47. http://doi.org/10.1029/2005RG000183.1.INTRODUCTION

Fatih Bulut, Marco Bohnhoff, M. A. and G. D. (2007). Characterization of aftershock-fault plane orientations of 1999 Izmit (Turkey) earthquake using high-resolution aftershock locations, 1–4. http://doi.org/10.1029/2007GL031154.Formatiert

Feigl, K. L., Sarti, F., Mcclusky, S., Ergintav, S., Durand, P., Bu, R., … Reilinger, R. (2002). Estimating Slip Distribution for the Izmit Mainshock from Coseismic GPS, ERS-1, RADARSAT, and SPOT Measurements. *Bulletin of the Seismological Society of America*, *92*(February), 138–160. http://doi.org/10.1785/0120000830

Ferretti, A., Monti-Guarnieri, A., & Prati, C. (2007). *InSAR Principles-Guidelines for SAR Interferometry Processing and Interpretation.* Retrieved from http://www.esa.int/esapub/tm/tm19/TM-19_ptA.pdf\nhttp://adsabs.harvard.edu/abs/2007ESATM..19.....F

Ferretti, A., Monti-guarnieri, A., Prati, C., & Rocca, F. (2007). Part B InSAR p rocessing: a practical approach, part B.

Fialko, Y., Simons, M., & Agnew, D. (2001). The complete (3-D) surface displacement field in the epicentral area of the 1999 Mw 7.1 Hector Mine earthquake, California, from space geodetic observations. *Geophysical Research Letters*, *28*(16), 3063–3066. http://doi.org/10.1029/2001GL013174

Flerit, F., Armijo, R., King, G. C. P., Meyer, B., & Barka, a. (2003). Slip partitioning in the Sea of Marmara pull-apart determined from GPS velocity vectors. *Geophysical Journal International*, *154*(1), 1–7. http://doi.org/10.1046/j.1365-246X.2003.01899.x

Foroosh, H., Zerubia, J. B., & Berthod, M. (2002). Extension of phase correlation to subpixel registration. *IEEE Transactions on Image Processing*, *11*(3), 188–199. http://doi.org/10.1109/83.988953

Goldstein, R. M., & Werner, C. L. (1998). Radar interferogram filtering for geophysical applications. *Geophysical Research Letters*, *25*(21), 4035. http://doi.org/10.1029/1998GL900033

Goudarzi, M. A., Woldai, T., & Tolpekin, V. a. (2012). Response to comments raised on "Surface deformation caused by April 6th 2009 earthquake in L'Aquila (Italy): A comparative analysis from ENVISAT ASAR, ALOS PALSAR and ASTER" by Chini Marco; Bignami Christian and Salvatore Stramondo. *International Journal of Applied Earth Observation and Geoinformation*, *18*(1), 582–583. http://doi.org/10.1016/j.jag.2012.01.007

Gürbüz, A., & Gürer, Ö. F. (2008). Tectonic Geomorphology of the North Anatolian Fault Zone in the Lake Sapanca Basin (eastern Marmara Region, Turkey). *Geosciences Journal*, *12*(3), 215–225. http://doi.org/10.1007/s12303-008-0022-9

Hamiel, Y., & Fialko, Y. (2007). Structure and mechanical properties of faults in the North Anatolian Fault system from InSAR observations of coseismic deformation due to the 1999 Izmit (Turkey) earthquake. *Journal of Geophysical Research: Solid Earth*, *112*(7), 1–12. http://doi.org/10.1029/2006JB004777

Hanssen, R. (2001). *Radar interferometry:Data Inerpretation and Error Analysis. Rev. Geophys.* Dordrecht: Kluwer Academic.ch5 http://doi.org/0-7923-6945-9

Hanssen, R. F. (2005). Satellite radar interferometry for deformation monitoring: A priori assessment of feasibility and accuracy. *International Journal of Applied Earth Observation and Geoinformation*, *6*(3-4), 253–260. http://doi.org/10.1016/j.jag.2004.10.004

Hasancebi, N., & Ulusay, R. (2006). Evaluation of site amplification and site period using different methods for an earthquake-prone settlement in Western Turkey. *Engineering Geology*, *87*(1-2), 85–104. http://doi.org/10.1016/j.enggeo.2006.05.004

Hearn, E. H. (2002). Viscoelastic deformation from North Anatolian Fault Zone earthquakes and the eastern Mediterranean GPS velocity field. *Geophysical Research Letters*, *29*(11), 19–21. http://doi.org/10.1029/2002GL014889

Hetland, E. A., Musé, P., Simons, M., Lin, Y. N., Agram, P. S., & DiCaprio, C. J. (2012). Multiscale InSAR Time Series (MInTS) analysis of surface deformation. *Journal of Geophysical Research*, *117*(B2), B02404. http://doi.org/10.1029/2011JB008731

Hitchcock, C., Altunel, E., Barka, A., Bachhuber, J., Lettis, W., Kozaci, Ö., … Lindvall, S. (2003). Timing of Late Holocene earthquakes on the Eastern Düzce Fault and implications for slip transfer between the Southern and Northern strands of the North Anatolian fault systems, Bolu, Turkey. *Turkish Journal of Earth Sciences*, *12*(1), 119–136.

Hooper, A., Bekaert, D., Spaans, K., & Arikan, M. (2012). Recent advances in SAR interferometry time series analysis for measuring crustal deformation. *Tectonophysics*, *514-517*, 1–13. http://doi.org/10.1016/j.tecto.2011.10.013

Hooper, A. J. (2008). A multi-temporal InSAR method incorporating both persistent scatterer and small baseline approaches. *Geophysical Research Letters*, *35*(16), 1–5. http://doi.org/10.1029/2008GL034654

Hooper, A., & Zebker, H. a. (2007). Phase unwrapping in three dimensions with application to InSAR time series. *Journal of the Optical Society of America. A, Optics, Image Science, and Vision*, *24*(9), 2737–2747. http://doi.org/10.1364/JOSAA.24.002737

Jolivet, R., Grandin, R., Lasserre, C., Doin, M.-P., & Peltzer, G. (2011). Systematic InSAR tropospheric phase delay corrections from global meteorological reanalysis data. *Geophysical Research Letters*, *38*(17), n/a–n/a. http://doi.org/10.1029/2011GL048757

Kiratzi, A. a. (1993). A study on the active crustal deformation of the north and east anatolian fault zones. *Tectonophysics*, *225*(3), 191–203. http://doi.org/10.1016/0040-1951(93)90279-S

Kuglin, C. D., & Hines, D. C. (1975). The phase correlation image alignment method. *IEEE International Conference on Cybernetics and Society*.

Lasserre, C., Peltzer, G., Crampé, F., Klinger, Y., Van der Woerd, J., & Tapponnier, P. (2005). Coseismic deformation of the 2001 Mw = 7.8 Kokoxili earthquake in Tibet, measured by synthetic aperture radar interferometry. *Journal of Geophysical Research: Solid Earth*, *110*(12), 1–17. http://doi.org/10.1029/2004JB003500

Leprince, S., Ayoub, F., Klinger, Y., & Avouac, J. P. (2007). Co-Registration of Optically Sensed Images and Correlation (COSI-Corr): An operational methodology for ground deformation measurements. *International Geoscience and Remote Sensing Symposium (IGARSS)*, 1943–1946. http://doi.org/10.1109/IGARSS.2007.4423207

Leprince, S., Barbot, S., Ayoub, F., & Avouac, J. P. (2007). Automatic, Precise, Ortho-rectification and Coregistration for satellite Image Correlation, Application to Ground Deformation Measurement. *IEEE J. Geosci. Rem. Sens.*, *45*(6), 1529–1558.

Leprince, S., Member, S., Musé, P., & Avouac, J. (2008). In-Flight CCD Distortion Calibration for Pushbroom Satellites Based on Subpixel Correlation, *46*(9), 2675–2683.

Leprince, S., Musé, P., & Avouac, J. P. (2008). In-flight CCD distortion calibration for pushbroom satellites based on subpixel correlation. *IEEE Transactions on Geoscience and Remote Sensing*, *46*(9), 2675–2683. http://doi.org/10.1109/TGRS.2008.918649

Lorenzo-Martín, F., Roth, F., & Wang, R. (2006). Elastic and inelastic triggering of earthquakes in the North Anatolian Fault zone. *Tectonophysics*, *424*(3-4), 271–289. http://doi.org/10.1016/j.tecto.2006.03.046

Lu, Z., Zhang, J., Zhang, Y., & Dzurisin, D. (2010). Monitoring and characterizing natural hazards with satellite InSAR imagery. *Annals of GIS*, *16*(1), 55–66. http://doi.org/10.1080/19475681003700914

Mansourpour, M., Rajabi, M. A., Filtering, S., & Filter, A. (2000). Effects and performance of speckle noise reduction filters on active radar and sar images, (JANUARY).

Masato Furuya. (2011). *Encyclopedia of Solid Earth Geophysics*. pp 1041-1048 http://doi.org/10.1007/978-90-481-8702-7

Massonnet, D., & Feigl, K. L. (1998). Radar interferometry and its application to changes in the Earth's surface. *Reviews of Geophysics*, *36*(4), 441. http://doi.org/10.1029/97RG03139

Massonnet, D., Rossi, M., Carmona, C., Adragna, F., Peltzer, G., Feigl, K., & Rabaute, T. (1993). The displacement field of the Landers earthquake mapped by radar interferometry. *Nature*, *364*(6433), 138–142. http://doi.org/10.1038/364138a0

McKenzie, D. (1972). Active Tectonics of the Mediterranean Region. *Geophysical Journal of the Royal Astronomical Society*, *30*, 109–185. http://doi.org/10.1111/j.1365-246X.1972.tb02351.x

Michel, R. (2002). Deformation due to the 17 August 1999 Izmit, Turkey, earthquake measured from SPOT images. *Journal of Geophysical Research*, *107*(B4). http://doi.org/10.1029/2000JB000102

Michel, R., & Rignot, E. (1996). Flow of Moreno Glaciar, Argentina, from repeat-pass Shuttle Imaging Radar images: Comparison of the phase correlation method with radar interferometry. *Journal of Glaciology*, *42*(141),

279–291.

Michel, R., & Taboury, J. (1999). Measuring ground displacements from SAR amplitude images: application to the Landers earthquake, *26*(7), 875–878.

Milliner, C. W. D., Dolan, J. F., Hollingsworth, J., Leprince, S., Ayoub, F., & Sammis, C. G. (2015). Quantifying near-field and off-fault deformation patterns of the 1992 M w 7.3 Landers earthquake. *Geochemistry, Geophysics, Geosystems*, *16*(5), 1577–1598. http://doi.org/10.1002/2014GC005693

Mora, O., Lanari, R., Mallorqui, J. J., Berardino, P., & Sansosti, E. (2002). A new algorithm for monitoring localized deformation phenomena based on small baseline differential SAR interferograms. *IEEE International Geoscience and Remote Sensing Symposium*, *2*(11), 2375–2383. http://doi.org/10.1109/IGARSS.2002.1025900

Necsoiu, M., Leprince, S., Hooper, D. M., Dinwiddie, C. L., McGinnis, R. N., & Walter, G. R. (2009). Monitoring migration rates of an active subarctic dune field using optical imagery. *Remote Sensing of Environment*, *113*(11), 2441–2447. http://doi.org/10.1016/j.rse.2009.07.004

Oglesby, D. D., & Mai, P. M. (2012). Fault geometry, rupture dynamics and ground motion from potential earthquakes on the North Anatolian Fault under the Sea of Marmara. *Geophysical Journal International*, *188*(3), 1071–1087. http://doi.org/10.1111/j.1365-246X.2011.05289.x

Okay, a. I., Kaşlilar-Özcan, a., Imren, C., Boztepe-Güney, a., Demirbag, E., & Kuşçu, I. (2000). Active faults and evolving strike-slip basins in the Marmara Sea, northwest Turkey: A multichannel seismic reflection study. *Tectonophysics*, *321*(2), 189–218. http://doi.org/10.1016/S0040-1951(00)00046-9

Ozgun Konca, a., Leprince, S., Avouac, J. P., & Helmberger, D. V. (2010). Rupture process of the 1999 Mw 7.1 duzce earthquake from joint analysis of SPOT, GPS, InSAR, strong-motion, and teleseismic data: A supershear rupture with variable rupture velocity. *Bulletin of the Seismological Society of America*, *100*(1), 267–288. http://doi.org/10.1785/0120090072

Pagli, C., Wang, H., Wright, T. J., Calais, E., & Lewi, E. (2014). Current plate boundary deformation of the Afar rift from a 3-D velocity field inversion of InSAR and GPS. *Journal of Geophysical Research : Solid Earth*, (August), 8562–8575. http://doi.org/10.1002/2014JB011391.Received

Pathier, E., Fielding, E. J., Wright, T. J., Walker, R., Parsons, B. E., & Hensley, S. (2006). Displacement field and slip distribution of the 2005 Kashmir earthquake from SAR imagery. *Geophysical Research Letters*, *33*(20), 1–5. http://doi.org/10.1029/2006GL027193

Peltzer, G. (1999). Evidence of Nonlinear Elasticity of the Crust from the Mw7.6 Manyi (Tibet) Earthquake. *Science*, *286*(5438), 272–276. http://doi.org/10.1126/science.286.5438.272

Peltzer, G., Crampé, F., & Rosen, P. (2001). The Mw 7.1, Hector Mine, California earthquake: surface rupture, surface displacement field, and fault slip solution from ERS SAR data. *Comptes Rendus de l'Académie Des Sciences - Series IIA - Earth and Planetary Science*, *333*(9), 545–555. http://doi.org/10.1016/S1251-8050(01)01658-5

Pondard, N., Armijo, R., King, G. C. P., Meyer, B., & Flerit, F. (2007). Fault interactions in the Sea of Marmara pull-apart (North Anatolian Fault): Earthquake clustering and propagating earthquake sequences. *Geophysical Journal International*, *171*(3), 1185–1197. http://doi.org/10.1111/j.1365-246X.2007.03580.x

Pratt, W. (1974). Correlation Techniques of Image Registration. *IEEE Transactions on Aerospace and Electronic Systems*, *AES-10*(3), 353–358. http://doi.org/10.1109/TAES.1974.307828

Pucci, S., Palyvos, N., Zabci, C., Pantosti, D., & Barchi, M. (2006). Coseismic ruptures and tectonic landforms along the D??zce segment of the North Anatolian Fault Zone (Ms 7.1, November 1999). *Journal of Geophysical Research: Solid Earth*, *111*(6), 1–16. http://doi.org/10.1029/2004JB003578

Pucci, S., Pantosti, D., Barchi, M. R., & Palyvos, N. (2007). A complex seismogenic shear zone: The D??zce segment of North Anatolian Fault (Turkey). *Earth and Planetary Science Letters*, *262*(1-2), 185–203. http://doi.org/10.1016/j.epsl.2007.07.038

Puymbroeck, V. (2008). Monitoring Earth Surface Dynamics With Optical Imagery. *Geology*, *89*(1). http://doi.org/10.1029/2001JB000951.K

Qing, X., Guowang, J., Caiying, Z., Zhengde, W., Yu, H., Peizhang, Y., … Vi, W. G. (2000). The filtering and phase unwrapping of interferogram, *1*. Retrieved from https://www.researchgate.net/profile/Guowang_Jin/publication/251802384_THE_FILTERING_AND_P

HASE_UNWRAPPING_OF_INTERFEROGRAM/links/553f72990cf23e796bfb48fd.pdf

Reilinger, R., McClusky, S., Vernant, P., Lawrence, S., Ergintav, S., Cakmak, R., … Karam, G. (2006). GPS constraints on continental deformation in the Africa-Arabia-Eurasia continental collision zone and implications for the dynamics of plate interactions. *Journal of Geophysical Research: Solid Earth*, *111*(5), 1–26. http://doi.org/10.1029/2005JB004051

Reilinger, R. E. (2000). Coseismic and Postseismic Fault Slip for the 17 August 1999, M = 7.5, Izmit, Turkey Earthquake. *Science*, *289*(5484), 1519–1524. http://doi.org/10.1126/science.289.5484.1519

Riddick, S. N., & Schmidt, D. A. (2011). Time-dependent changes in volcanic inflation rate near Three Sisters, Oregon, revealed by InSAR. *Geochemistry, Geophysics, Geosystems*, *12*(12), 1–14. http://doi.org/10.1029/2011GC003826

Rockwell, T., Barka, A., Dawson, T., Akyuz, S., & Thorup, K. (2001). Paleoseismology of the Gazikoy-Saros segment of the North Antolia fault, Northwestern Turkey: Comparison of the historical and paleoseismic records, implications of regional seismic hazard, and models of earthquake recurrence. *Journal of Seismology*, *5*(3), 433–448. http://doi.org/10.1023/A:1011435927983

Rosen, P. a., Hensley, S., Joughin, I. R., Li, F. K., Madsen, S. N., Rodriguez, E., & Goldstein, R. M. (2000). Synthetic aperture radar interferometry. *Proceedings of the IEEE*, *88*(3), 333–382. http://doi.org/10.1109/5.838084

Rosen, P. a., Hensley, S., Peltzer, G., & Simons, M. (2004). Updated repeat orbit interferometry package released. *Eos, Transactions American Geophysical Union*, *85*(5), 47. http://doi.org/10.1029/2004EO050004

Rosu, A.-M. M., Pierrot-Deseilligny, M., Delorme, A., Binet, R., & Klinger, Y. (2014). Measurement of ground displacement from optical satellite image correlation using the free open-source software MicMac. *ISPRS Journal of Photogrammetry and Remote Sensing*. http://doi.org/10.1016/j.isprsjprs.2014.03.002

Rott, H. (2009). Advances in interferometric synthetic aperture radar (InSAR) in earth system science. *Progress in Physical Geography*, *33*(6), 769–791. http://doi.org/10.1177/0309133309350263

Sahin, M., & Tari, E. (2000). The August 17 Kocaeli and the November 12 Duzce earthquakes in Turkey. *Earth Planets Space*, 753–757.

Samieie-esfahany, S., Hanssen, R. F., Thienen-visser, K. Van, Muntendam-bos, A., Samiei-Esfahany, S., Hanssen, R. F., … Muntendam-bos, A. (2010). On the effect of horizontal deformation on InSAR subsidence estimates. *Proceedings of Fringe 2009 Workshop*, *2009*(March).

Sandwell, D. T., Sichoix, L., & Smith, B. (2002). The 1999 Hector Mine earthquake, southern California: Vector near-field displacements from ERS InSAR. *Bulletin of the Seismological Society of America*, *92*(4), 1341–1354. http://doi.org/10.1785/0120000901

Similox-Tohon, D., Fernandez-alonso, M., Vanneste, K., Waelkens, M., Muchez, P., & Sintubin, M. (2008). Burdur-Isparta Region (Sw Turkey): Remote Sensing , Surface Geology and Near-Surface Geophysics. *Sagalassos VI Geo- and Bio-Archaeology at Sagalassos and in Its Territory*, 75–130.

Simons, M., & Rosen, P. a. (2007). Interferometric Synthetic Aperture Radar Geodesy. *Aperture*, *3*(Geodesy), 391–446. http://doi.org/10.1016/B978-0-12-386874-9.00010-5

Sousa, J. J., Ruiz, A. M., Hanssen, R. F., Bastos, L., Gil, A. J., Galindo-Zaldívar, J., & Sanz de Galdeano, C. (2010). PS-InSAR processing methodologies in the detection of field surface deformation—Study of the Granada basin (Central Betic Cordilleras, southern Spain). *Journal of Geodynamics*, *49*(3-4), 181–189. http://doi.org/10.1016/j.jog.2009.12.002

Squeesar, D., Ferretti, A., Fumagalli, A., Novali, F., Prati, C., Rocca, F., … Psinsar, I. (2011). A New Algorithm for Processing Interferometric Data-Stacks: SqueeSAR. *IEEE Transactions on Geoscience and Remote Sensing*, *49*(9), 3460–3470. http://doi.org/10.1109/TGRS.2011.2124465

Stein, A. F. van der M. and B. G. (Ed.). (2002). *Spatial Statistics For Remote Sensing*. New York, Boston, Dordrect, London, Moscow: Kluwer Academic.pp20-22, ISBN: 0-306-47647-9

Stein, R. S., Barka, A. a, & Dieterich, J. H. (1997). Progressive failure on the North Anatolian fault since 1939 by earthquake stress triggering. *Geophysical Journal International*, *128*, 594–604. http://doi.org/10.1111/j.1365-246X.1997.tb05321.x

Stone, H. S., Orchard, M. T., Chang, E. C., & Martucci, S. a. (2001). A fast direct Fourier-based algorithm for subpixel registration of images. *IEEE Transactions on Geoscience and Remote Sensing*, *39*(10), 2235–2243. http://doi.org/10.1109/36.957286

Tahayt, a., Feigl, K. L., Mourabit, T., Rigo, a., Reilinger, R., McClusky, S., … Ben Sari, D. (2009). The Al Hoceima (Morocco) earthquake of 24 February 2004, analysis and interpretation of data from ENVISAT ASAR and SPOT5 validated by ground-based observations. *Remote Sensing of Environment*, *113*(2), 306–316. http://doi.org/10.1016/j.rse.2008.09.015

Tibi, R., Bock, G., Xia, Y., Baumbach, M., Grosser, H., Milkereit, C., … Zschau, J. (2001). Rupture processes of the 1999 August 17 Izmit and November 12 Düzce (Turkey) earthquakes. *Geophysical Journal International*, *144*(2), F1–F7. http://doi.org/10.1046/j.1365-246x.2001.00360.x

Tobita, M., Murakami, M., Nakagawa, H., Yarai, H., Fujiwara, S., & Rosen, P. A. (2001). 3-D surface deformation of the 2000 Usu Eruption measured by matching of SAR images. *Geophysical Research Letters*, *28*(22), 4291–4294. http://doi.org/10.1029/2001GL013329

Townshend, J. R. G., Justice, C. O., Gurney, C., & McManus, J. (1992). The impact of misregistration on change detection. *IEEE Transactions on Geoscience and Remote Sensing*, *30*(5), 1054–1060. http://doi.org/10.1109/36.175340

Ürüşan, A. Y. (2014). Relations between the GNSS, InSAR, and the other techniques for prediction of earthquakes. *Arabian Journal of Geosciences*. http://doi.org/10.1007/s12517-014-1670-x

Utkucu, M., Nalbant, S. S., McCloskey, J., Steacy, S., & Alptekin, Ö. (2003). {S}lip distribution and stress changes associated with the 1999 {N}ovember 12, {D}{ü}zce ({T}urkey) earthquake ({M}w=7.1). *Geophysical Journal International*, *153*(1), 229–241. http://doi.org/10.1046/j.1365-246X.2003.01904.x

Vadon, H., & Massonnet, D. (2000). Earthquake displacement fields mapped by very precise correlation. Complementarity with radar interferometry. *Geoscience and Remote Sensing Symposium, 2000. Proceedings. IGARSS 2000. IEEE 2000 International*, *6*, 2700–2702.

van der Meer, F. D., van der Werff, H. M. a, van Ruitenbeek, F. J. a, Hecker, C. a., Bakker, W. H., Noomen, M. F., … Woldai, T. (2012). Multi- and hyperspectral geologic remote sensing: A review. *International Journal of Applied Earth Observation and Geoinformation*, *14*(1), 112–128. http://doi.org/10.1016/j.jag.2011.08.002

Van der Meer, F. D., van der Werff, H. M. A., & van Ruitenbeek, F. J. A. (2014). Potential of ESA's Sentinel-2 for geological applications. *Remote Sensing of Environment*, *148*(MAY 2014), 124–133. http://doi.org/10.1016/j.rse.2014.03.022

Van Puymbroeck, N., Michel, R., Binet, R., Avouac, J. P., & Taboury, J. (2000). Measuring earthquakes from optical satellite images. *Applied Optics*, *39*(20), 3486–94. http://doi.org/10.1364/AO.39.003486

Walter, D., Wegmüller, U., Spreckels, V., Hannemann, W., & Busch, W. (2008). Interferometric Monitoring of an Active Underground Mining Field With High-Resolution Sar Sensors. *Geotechnical Engineering*, *35*.

Wang, H., Ge, L., Xu, C., & Du, Z. (2007). 3-D coseismic displacement field of the 2005 Kashmir earthquake inferred from satellite radar imagery. *Earth, Planets and Space*, *59*(5), 343–349.

Wang, T., & Jónsson, S. (2014). Improved SAR Amplitude Image Offset Measurements for Deriving Three-Dimensional Coseismic Displacements. *IEEE Journal of Selected Topics in Applied Earth Observations and Remote Sensing*, 1–8. http://doi.org/10.1109/JSTARS.2014.2387865

Wauthier, C., Oyen, A. M., Marinkovic, P. S., Cayol, V., Fernandez, Gonzalez, J. P., … Walter, T. R. (2009). L-band and C-band insar studies of african volcanic areas. *International Geoscience and Remote Sensing Symposium (IGARSS)*, *2*(February 2016). http://doi.org/10.1109/IGARSS.2009.5418043

Wegner, J., Inglada, J., & Tison, C. (2008). Automatic Fusion of {SAR} and Optical Imagery based on Line Features. *7th European Conference on Synthetic Aperture Radar*.

Wright, T. J. (2002). Remote monitoring of the earthquake cycle using satellite radar interferometry. *Philosophical Transactions of the Royal Society A: Mathematical, Physical and Engineering Sciences*, *360*(1801), 2873–2888. http://doi.org/10.1098/rsta.2002.1094

Wright, T. J. (2004). Toward mapping surface deformation in three dimensions using InSAR. *Geophysical Research*

Letters, *31*(1), 1–5. http://doi.org/10.1029/2003GL018827

Wright, T. J., Ebinger, C., Biggs, J., Ayele, A., Yirgu, G., Keir, D., & Stork, A. (2006). Magma-maintained rift segmentation at continental rupture in the 2005 Afar dyking episode. *Nature*, *442*(7100), 291–294. http://doi.org/10.1038/nature04978

Wright, T. J., Ebinger, C., Biggs, J., Ayele, A., Yirgu, G., Keir, D., & Stork, A. (2006). Magma-maintained rift segmentation at continental rupture in the 2005 Afar dyking episode. *Nature*, *442*(7100), 291–294. http://doi.org/10.1038/nature04978

Wright, T. J., Parsons, B. E., Jackson, J. a., Haynes, M., Fielding, E. J., England, P. C., & Clarke, P. J. (1999). Source parameters of the 1 October 1995 Dinar (Turkey) earthquake from SAR interferometry and seismic bodywave modelling. *Earth and Planetary Science Letters*, *172*(1-2), 23–37. http://doi.org/10.1016/S0012-821X(99)00186-7

Yaseen, M., & Anwar, S. (2013). Sensitivity analysis of sub-pixel correlation technique for measuring coseismic displacements using a pair of ASTER images. *Journal of Asian Earth Sciences*, *62*, 349–362. http://doi.org/10.1016/j.jseaes.2012.10.015

Yaseen, M., Hamm, N. a. S., Tolpekin, V., & Stein, A. (2013). Anisotropic kriging to derive missing coseismic displacement values obtained from synthetic aperture radar images. *Journal of Applied Remote Sensing*, *7*(1), 073580. http://doi.org/10.1117/1.JRS.7.073580

Zebker, H. a., & Villasenor, J. (1992). Decorrelation in interferometric radar echoes. *IEEE Transactions on Geoscience and Remote Sensing*, *30*(5), 950–959. http://doi.org/10.1109/36.175330

Zhang, J. (2010). Multi-source remote sensing data fusion: status and trends. *International Journal of Image and Data Fusion*, *1*(1), 5–24. http://doi.org/10.1080/19479830903561035

Zhiyong, W. Z. W., Jixian, Z. J. Z., Guoman, H. G. H., & Yonghong, Z. Y. Z. (2009). Monitoring Land Subsidence in Suzhou City Using D-InSAR Technique. *2009 2nd International Congress on Image and Signal Processing*, 1–4. http://doi.org/10.1109/CISP.2009.5300898

Zone, M. R., Ergintav, S., Bu, R., Mcclusky, S., & Reilinger, R. E. (2002). Postseismic Deformation near the Izmit Earthquake. *Society*, (August 1999), 194–207.

The list of web page from which the current research has utilized information:

http://www.tectonics.caltech.edu/slip_history/spot_coseis/download_software.html

http://seismo.berkeley.edu/~burgmann/RESEARCH/TURKEY/turkey.html
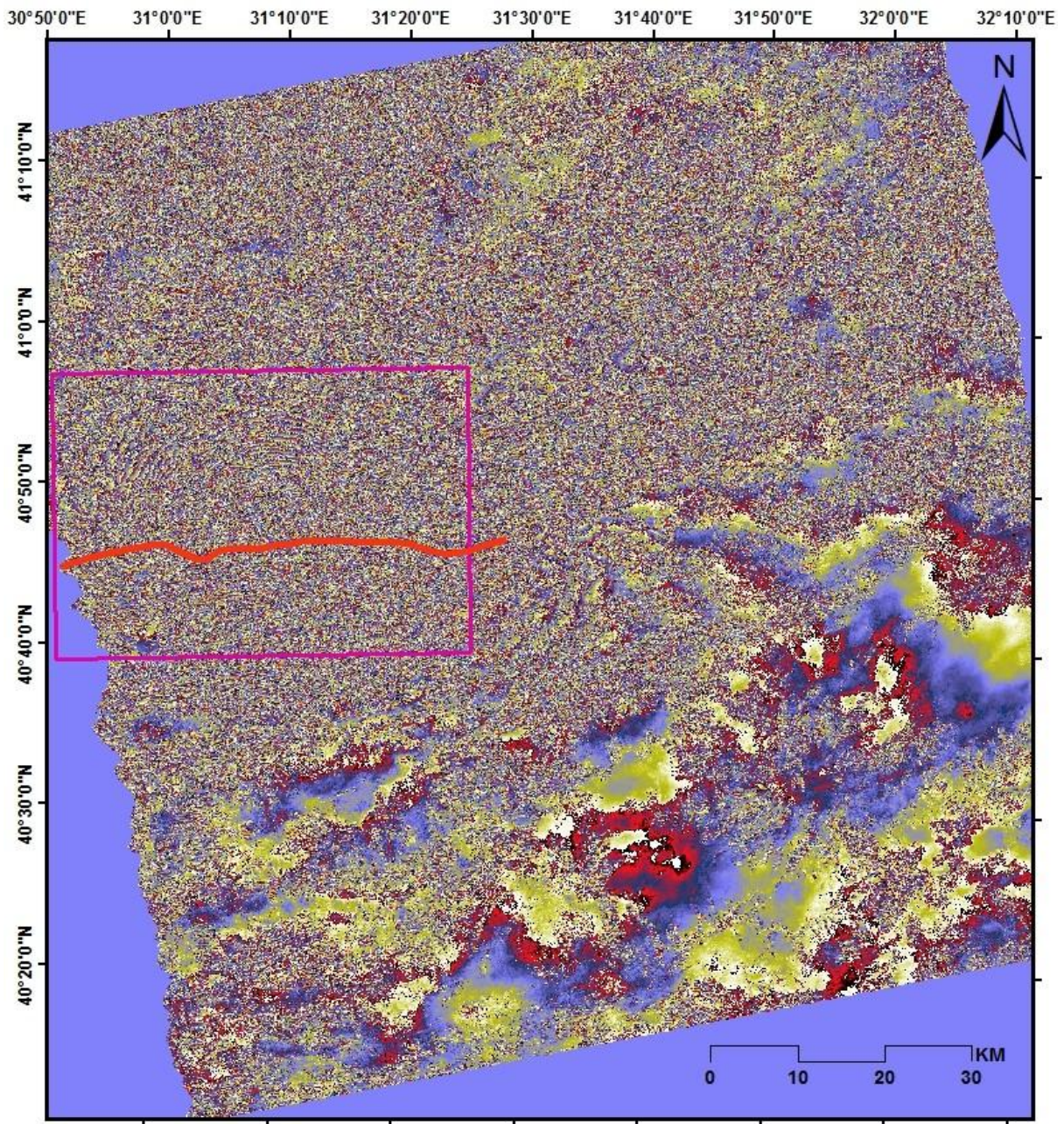
APPENDIX

Figure 6-1: Full View of SAR Interferogram Prepared from two SAR Images dated 14/09/99 and 99/11/23. This SAR image pair was acquired from Ascending East Track. The red line indicates Düzce rupture and area of interest for 3-D surface deformation model is highlighted as pink box.
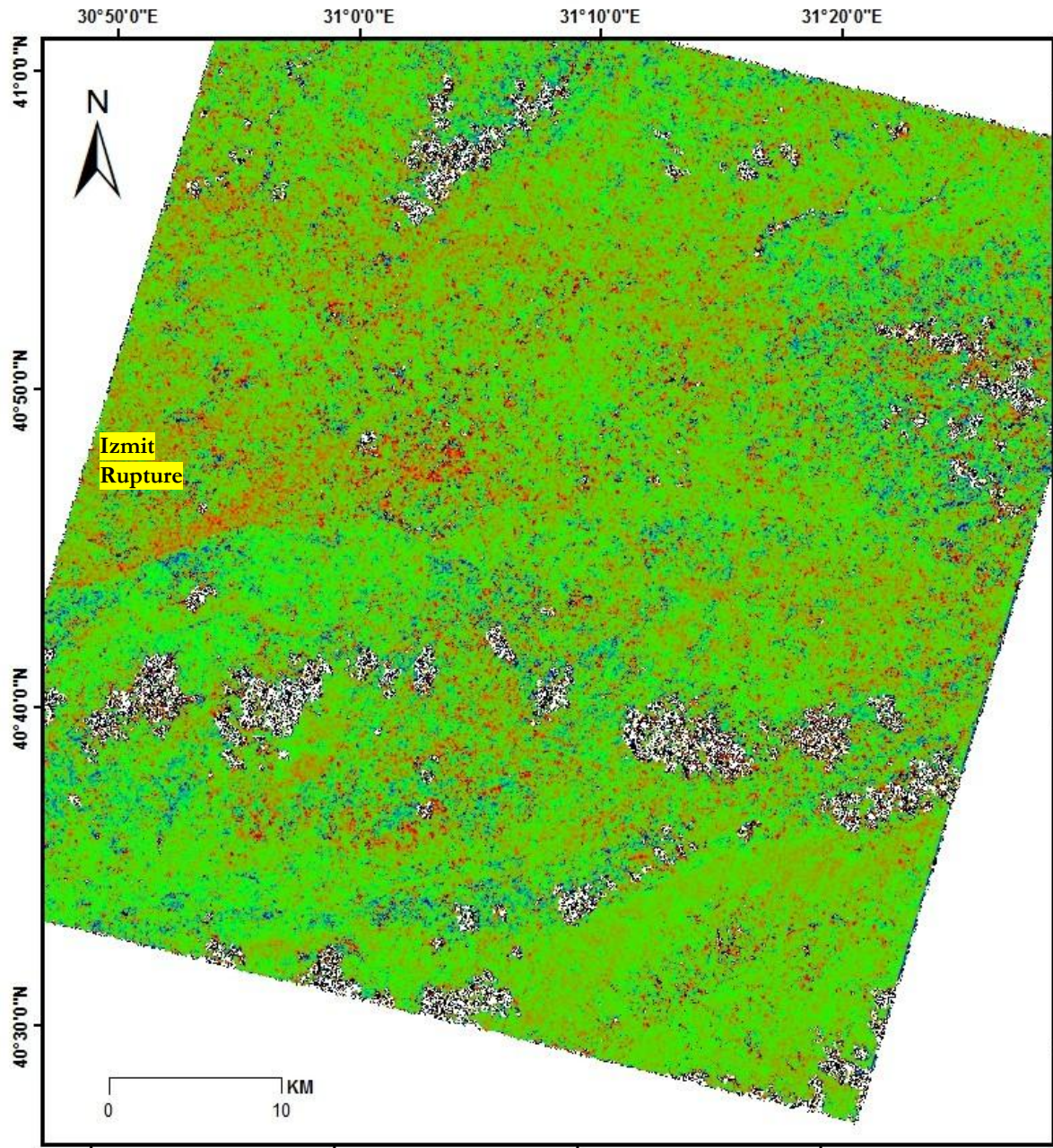
Figure 6-2: East-West Displacement map (positive towards East and Negative towards West) derived from sub-pixel correlation (window size 32×32 and step size 4) of SPOT Pan (10m) Image Pair (dated 21/06/1999 & 03/08/99 & 12/07/2000) bracketing Izmit earthquake rupture termination part
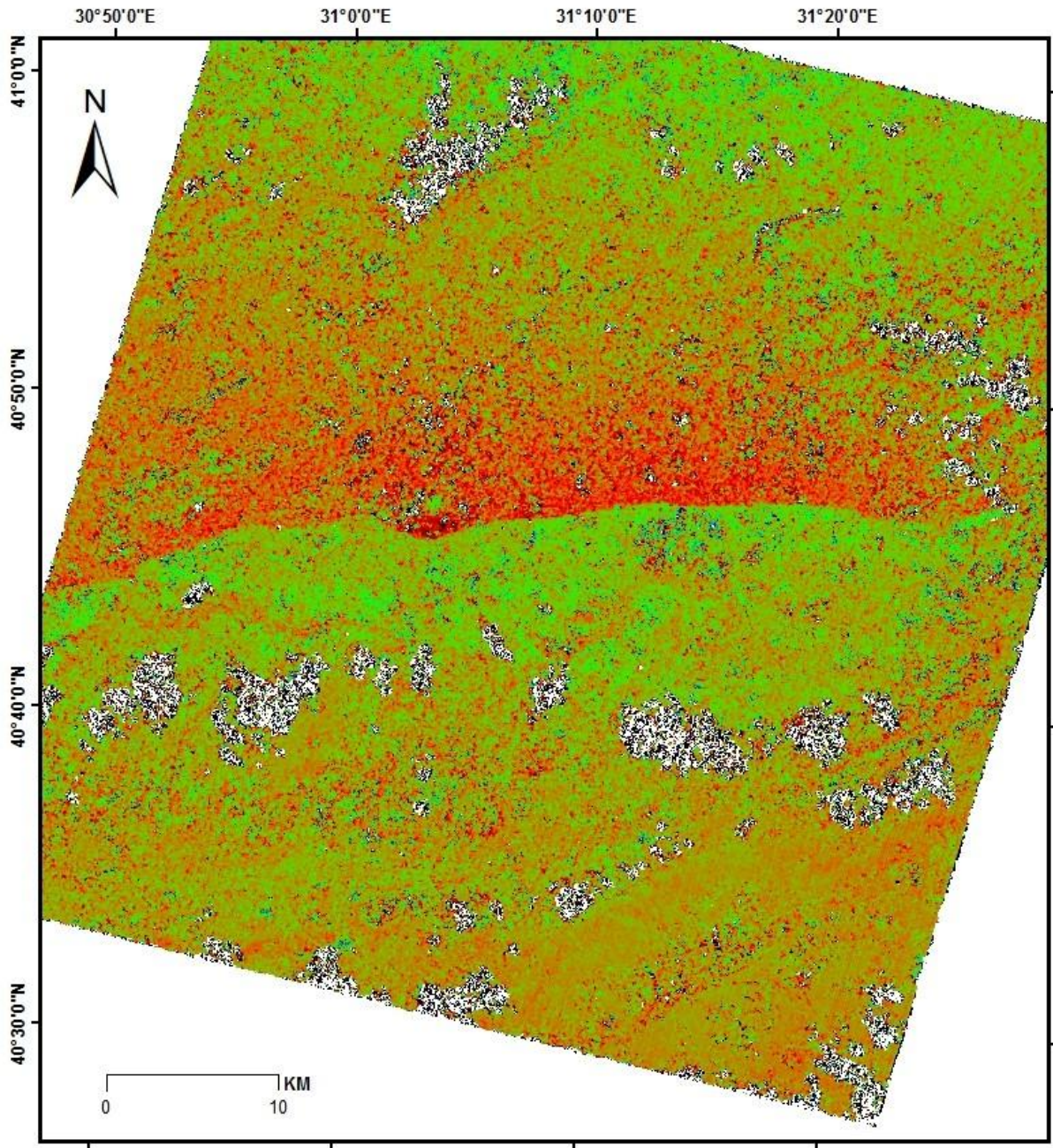
Figure 6-3 East-West Displacement map (positive towards East and Negative towards West) derived from sub-pixel correlation (window size 32×32 and step size 4) of SPOT Pan (10m) Image Pair (dated 21/06/99 & 12/07/2000) for both Izmit and Düzc earthquake combined rupture area.
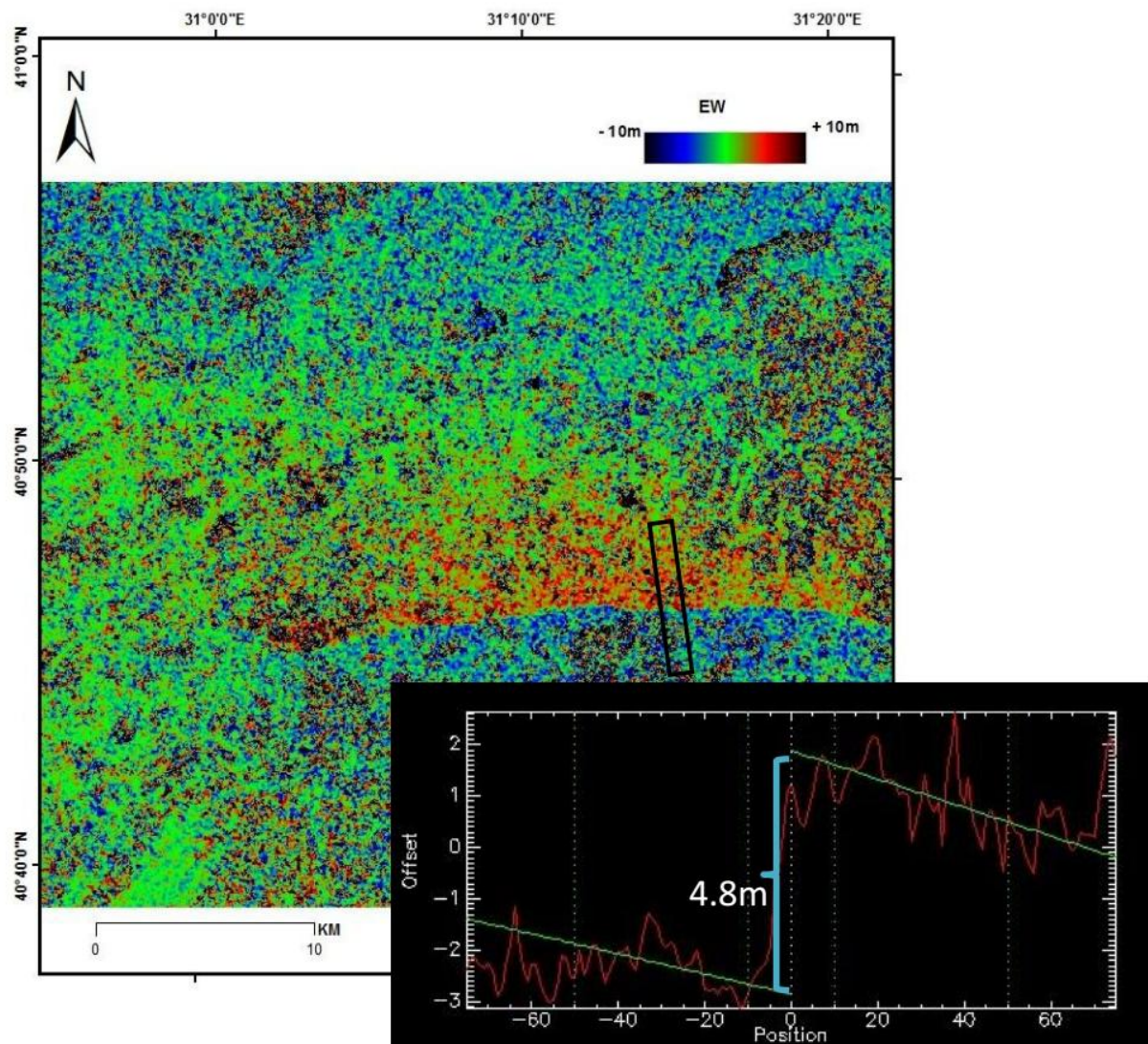
Figure 6-4 Profile is drawn across Düzce fault on EW displacement map. The profile is the two-dimensional measurement on the fault. Here offset is in meter and position across the fault is indicated by a number of pixels.
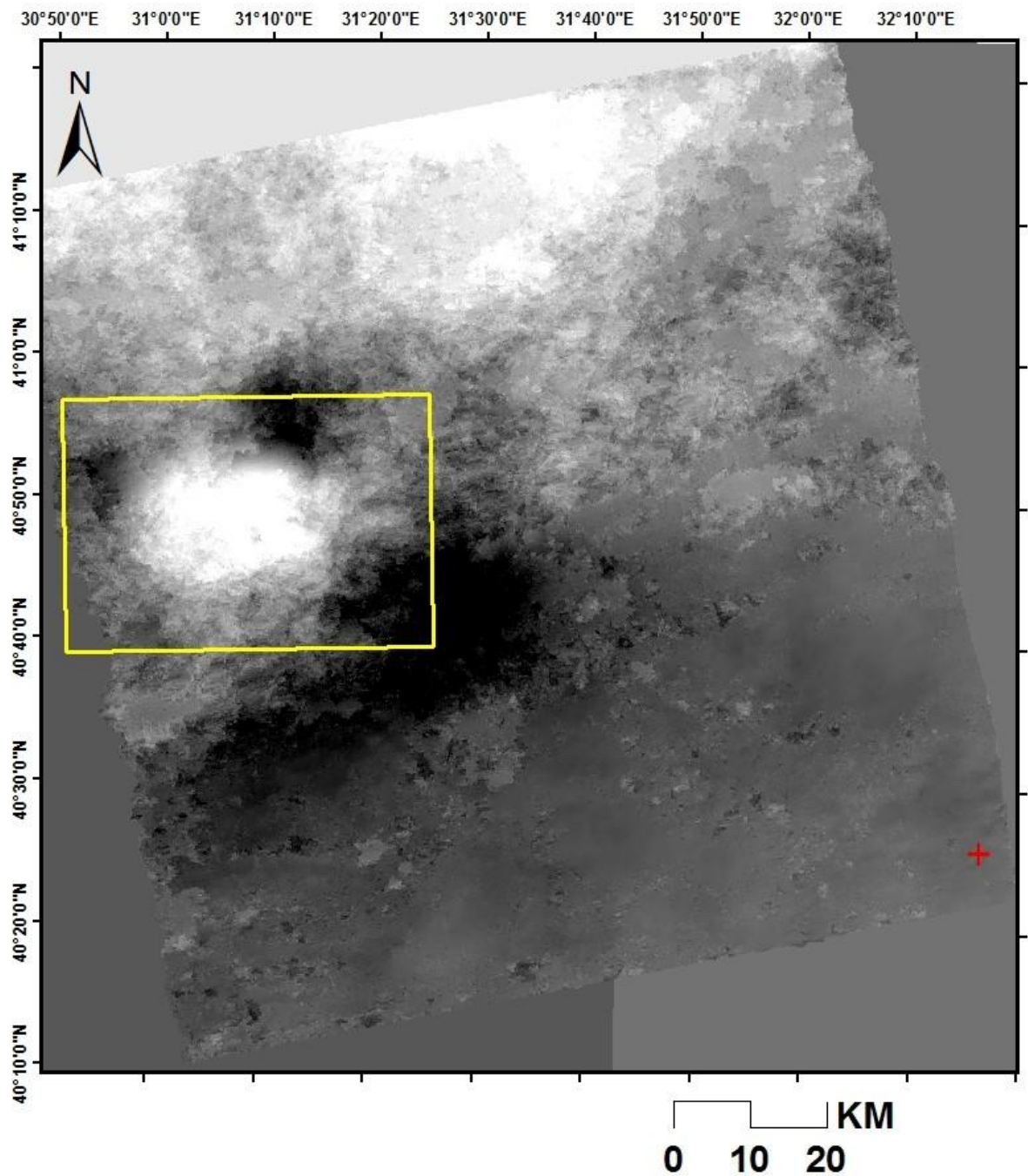
Figure 6-5 is showing the geocoded unwrapped interferogram. The yellow box is the region of interest for the 3-D model. The red plus indicates the assumed no displacement point whose radian value is considered during radian to meter conversion. The radian values for this map ranges from -97.5 to 47.5
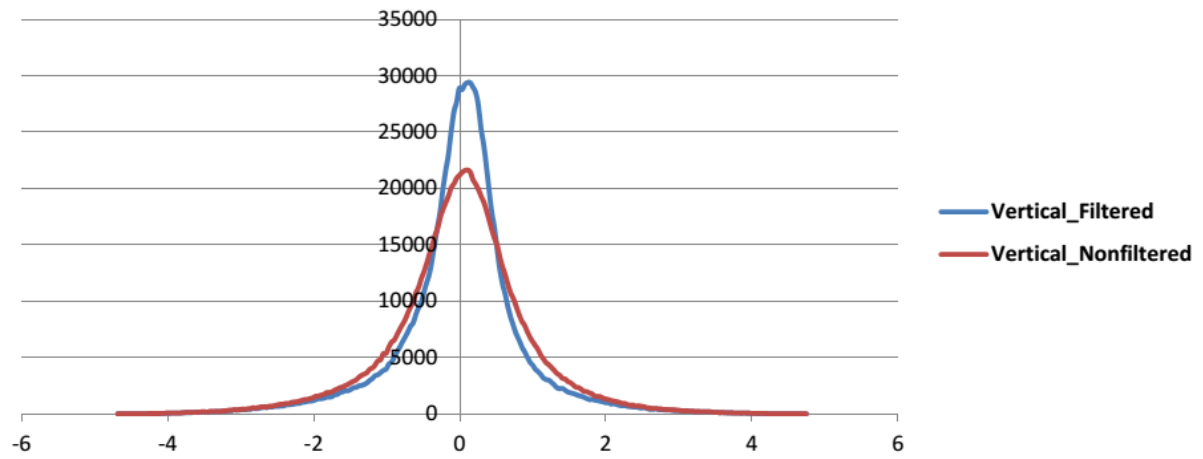
Figure 6-6 Histogram showing vertical displacement values against number of samples with and without applying non-local means filtering on COSI-Corr results